

IMPROVING SEISMIC VELOCITY MODELS WITH CONSTRAINTS FROM AUTOCORRELATION OF AMBIENT SEISMIC NOISE AND SIGNAL

Ileana M. Tibuleac, et al.

Nevada Seismological Laboratory
University of Nevada, Reno
1664 N. Virginia Street, MS 174
Reno, Nevada 89557

24 March 2016

Final Report

APPROVED FOR PUBLIC RELEASE; DISTRIBUTION IS UNLIMITED.



AIR FORCE RESEARCH LABORATORY
Space Vehicles Directorate
3550 Aberdeen Ave SE
AIR FORCE MATERIEL COMMAND
KIRTLAND AIR FORCE BASE, NM 87117-5776

DTIC COPY

NOTICE AND SIGNATURE PAGE

Using Government drawings, specifications, or other data included in this document for any purpose other than Government procurement does not in any way obligate the U.S. Government. The fact that the Government formulated or supplied the drawings, specifications, or other data does not license the holder or any other person or corporation; or convey any rights or permission to manufacture, use, or sell any patented invention that may relate to them.

This report was cleared for public release by the PRS OPSEC Office and is available to the general public, including foreign nationals. Copies may be obtained from the Defense Technical Information Center (DTIC) (<http://www.dtic.mil>).

AFRL-RV-PS-TR-2016-0098 HAS BEEN REVIEWED AND IS APPROVED FOR
PUBLICATION IN ACCORDANCE WITH ASSIGNED DISTRIBUTION STATEMENT.

//SIGNED//

Robert Raistrick
Program Manager, AFRL/RVBYE

//SIGNED//

Dr. Thomas R. Caudill, Acting Chief
AFRL Battlespace Environment Division

This report is published in the interest of scientific and technical information exchange, and its publication does not constitute the Government's approval or disapproval of its ideas or findings.

REPORT DOCUMENTATION PAGE

Form Approved
OMB No. 0704-0188

Public reporting burden for this collection of information is estimated to average 1 hour per response, including the time for reviewing instructions, searching existing data sources, gathering and maintaining the data needed, and completing and reviewing this collection of information. Send comments regarding this burden estimate or any other aspect of this collection of information, including suggestions for reducing this burden to Department of Defense, Washington Headquarters Services, Directorate for Information Operations and Reports (0704-0188), 1215 Jefferson Davis Highway, Suite 1204, Arlington, VA 22202-4302. Respondents should be aware that notwithstanding any other provision of law, no person shall be subject to any penalty for failing to comply with a collection of information if it does not display a currently valid OMB control number. PLEASE DO NOT RETURN YOUR FORM TO THE ABOVE ADDRESS.

1. REPORT DATE (DD-MM-YYYY) 24-03-2016	2. REPORT TYPE Final Report	3. DATES COVERED (From - To) 24 Apr 2014 – 24 Mar 2016		
4. TITLE AND SUBTITLE Improving Seismic Velocity Models with Constraints from Autocorrelation of Ambient Seismic Noise and Signal		5a. CONTRACT NUMBER FA9453-14-C-0214		
		5b. GRANT NUMBER		
		5c. PROGRAM ELEMENT NUMBER 62601F		
6. AUTHOR(S) Ileana M. Tibuleac, David von Seggern, Marlon Ramos, and Ryley Hill		5d. PROJECT NUMBER 1010		
		5e. TASK NUMBER PPM00016477		
		5f. WORK UNIT NUMBER EF127063		
7. PERFORMING ORGANIZATION NAME(S) AND ADDRESS(ES) Nevada Seismological Laboratory University of Nevada, Reno 1664 N. Virginia Street, MS 174 Reno, Nevada 89557		8. PERFORMING ORGANIZATION REPORT NUMBER		
9. SPONSORING / MONITORING AGENCY NAME(S) AND ADDRESS(ES) Air Force Research Laboratory Space Vehicles Directorate 3550 Aberdeen Avenue SE Kirtland AFB, NM 87117-5776		10. SPONSOR/MONITOR'S ACRONYM(S) AFRL/RVBYE		
		11. SPONSOR/MONITOR'S REPORT NUMBER(S) AFRL-RV-PS-TR-2016-0098		
12. DISTRIBUTION / AVAILABILITY STATEMENT Approved for public release; distribution is unlimited. (OPS-16-12228 dtd 18 Jul 2016)				
13. SUPPLEMENTARY NOTES				
14. ABSTRACT Accurate crustal models are an essential, first requirement for any aspect related to event characterization and yield estimation. With the goal of adding independent constraints to the crust-mantle boundary depth, we developed and tested a new application of seismic interferometry, consisting of extraction of the reflection component of Green's Functions (GFs) from ambient noise and signal autocorrelation stacks, to solve for crust and mantle reflector properties. The optimized technique is applied in three areas of the western and central USA, for a variety of crust-mantle boundary transition settings and depths. Observed waveforms are compared to synthetic estimates, using receiver function and available seismic velocity model information. We find that the method works well for crust with low anisotropy and high reflectivity; however, corrections through additional investigations are recommended in areas of dipping crust or unreflective Moho. Recommendations for improved efficiency of the method are made, including use of overlapping windows and of days with high seismic activity. Using additional geophysical information and synthetic waveforms is important for accurate phase identification, which was the main challenge in this study.				
15. SUBJECT TERMS Ambient seismic noise interferometry, crust-mantle boundary, seismic velocity models				
16. SECURITY CLASSIFICATION OF: a. REPORT Unclassified		17. LIMITATION OF ABSTRACT Unlimited	18. NUMBER OF PAGES 84	19a. NAME OF RESPONSIBLE PERSON Robert Raistrick
b. ABSTRACT Unclassified		19b. TELEPHONE NUMBER (include area code)		
c. THIS PAGE Unclassified				

This page is intentionally left blank.

Table of Contents

1. SUMMARY	1
2. INTRODUCTION	2
3. TECHNICAL APPROACH.....	3
4. RESULTS AND DISCUSSION	4
5. CONCLUSIONS.....	20
REFERENCES	58
APPENDIX.....	61
LIST OF SYMBOLS, ABBREVIATIONS, AND ACRONYMS.....	75

List of Figures

Figure 1. Upper plot: Stations used in this study (see also Appendix 1, Table A1.3) in the area TEST. The lower plots show the SIMPLE (yellow) and COMPLEX (red) study areas.	25
Figure 2. The location of the three study areas in relation to an anisotropy map estimated by Schulte-Pelkum and Mahan, 2014.	26
Figure 3. P (upper plot) and S (lower plot) velocity models available at UNR (Tibuleac et al., 2013) and the COCORP stations as red filled squares.	27
Figure 4. A. The effect of thresholding prior to GF extraction at station O11A in the TEST region.	28
Figure 5. Noise autocorrelations filtered using three different wavelets and one Fourier approach.	29
Figure 6A. Wavelets investigated in this study with CWT - gaus5 (A), morl (B), sym5 (C), db4 (D), and db5 (E)	31
Figure 6B. Biases in arrival time estimates.	32
Figure 7. The analyst-estimated two way travel times for PmP (A,B) and SmS (C,D), the COCORP TWTT from Klemperer et al., 1986 (red triangles), and the EARS TWTT estimated from EARS receiver function data (green triangles, only in plots A and B).	33
Figure 8. Ten day stacks of GFs extracted at TEST AREA, station O11A when no pre-filtering was applied at Step 1 (section 3.2.1) are shown in plots A-D. Ten day stacks after pre-filtering at Step 1 (section 4.2.1), with 0.3 – 4 Hz high-pass, Butterworth, zero phase, eight-pole filter are shown in plots E-H.	34
Figure 9. Same as in Figure 8, with a comparison of CWT filters, centered on 1.3s (plots A-E) and 2s (plots F-J) applied on the Z-component at O11A. Plot K shows the zero-phase six pole Fourier filter centered on 2s.	35
Figure 10. Ten day stacks of GFs extracted at O11A with no pre-filtering, on the E (plots A,D), N (plots B,E) and Z (plots C,F) components.	36
Figure 11. The same plots as in Figure 10 are shown at A-C and G-I. To better isolate seasonal variations at O11A the stack for the whole period, GFALL (the right red trace) was removed from each ten-day stack. The results at two CWT center frequencies are shown in plots D-F (center period 1.3s) and plots J-L (center period 2s).	37

Figure 12. Shows the effect of using one hour, 50% overlap windows to compute autocorrelation stacks.	38
Figure 13. Polarization analysis of the two-year GF's (GFALL, red) at station O11A.....	39
Figure 14. A. PmP (~9.7s) and SmS (~16s) arrivals at station O11A, at a chosen center period of 2s, are identified using CWT and an empirically chosen gaus5 wavelet. Plots B,C,D and E show the F-statistic estimated at center periods 1.3s, 1.7s 2s and 2.4s for windows (W) twice the center period of the wavelet, on normalized waveforms, with a step of one sample point (at 20 sps).....	40
Figure 15. The Z-component GF's (GFBEAM) at stations in the TEST area, using 2 years of data are shown in the black rectangle in all plots.	41
Figure 16. Same as in Figure 15, with staggered GF's, at every station.	42
Figure 17. Same as in Figure 11, at station ELK (component Z).	42
Figure 18. Shows comparison of GF2006360, GF2008052 and GF2008117 with GFALL at stations O06A (brown), O07A (green) and ELK (cyan E, blue N and magenta Z).....	43
Figure 19. Comparison of three component waveforms simulated using the model M2 in Appendix 1, Table A1.3 for point-force sources with horizontal (fx=1, fy=1, fz=0), respectively vertical (fx,y=0, fz=1) located at 85 km depth.	44
Figure 20. Comparison of three component waveforms simulated using the model M2 in Appendix 1, Table A1.2.1 for point-force sources with random start (within 1 sec), located in a circle of one meter radius beneath the center BB station at 1 m depth (plots A-C) and 85 km depth (plots D-I).	45
Figure 21. Line sources every 200 m along the x axis start at 0.36s at 1 m depth (plots A-C) and 45 km depth (plots D-F).	46
Figure 22. Observed (plots E, K and P) and synthetic waveforms at station O11A.	47
Figure 23. Panels of 20-day GFs CWT filtered (plots 1-J) and Fourier filtered (plots K-M) at station ELFS.....	48
Figure 24. Similar to Figure 23, observed and synthetic waveforms at station O05C	49
Figure 25. Similar to Figure 23, observed and synthetic waveforms at station O08A	50
Figure 26. SIMPLE AREA Three wavelet representation of the 3C GFALL (extracted from 1-3 years of data) in the SIMPLE AREA.....	51

Figure 27. Similar to Figure 23, observed and synthetic waveforms at station N27A, SIMPLE AREA.....	52
Figure 28. Similar to Figure 23, observed and synthetic waveforms at station N29A, SIMPLE AREA.	53
Figure 29. Similar to Figure 23, observed and synthetic waveforms at station W29A, SIMPLE AREA.....	54
Figure 30. Same as in Figure 26, for the COMPLEX AREA.	55
Figure 31. Similar to Figure 23, observed and synthetic waveforms at stations SPMN and L37A are shown for comparison.....	56
Figure 32. Similar to Figure 23, observed and synthetic waveforms at station P37A.....	57

1. SUMMARY

Accurate crustal models are an essential, first requirement for any aspect related to event characterization and yield estimation. Until recently, seismic velocity model building was limited to paths from seismic zones, or from test/mining sites to existing stations. Recently, seismic interferometry has added independent information to the existing velocity models, from processing of ambient-noise extracted inter-station Green's Functions. This project developed and tested a new application of seismic interferometry, to extract the reflection Green's Functions and to solve for crust and mantle reflector properties. An optimised method is described, which in contrast to receiver functions, does not depend on large recorded seismic events. Also, in contrast to reflection/refraction seismic studies, the new method is applicable locally at all available seismic sensors, providing unprecedented resolution. The body wave (P and S) reflection component of the Green's Functions (*GFs*) was extracted from previously unexploited results of ambient-noise autocorrelations. Waveform modeling was used to investigate new, independent seismic crustal model constraints for selected stations in the United States of America. The investigation includes comparison to receiver function and other seismic velocity model results. In contrast to receiver functions, the method described here does not depend on large recorded seismic events. Also, in contrast to reflection/refraction seismic studies, the new method is applicable locally at all available seismic sensors, providing unprecedented resolution.

When applied in western and central United States of America, it has been found that the method works well for crust with low anisotropy and high reflectivity, however, corrections through additional investigations are recommended in areas of dipping crust or unreflective Moho. Recommendations for improved efficiency of the method are made, including use of overlapping windows and of days with high seismic activity. The main challenge in this study was accurate phase identification and picking, and thus, it is important that additional geophysical information and synthetic waveforms are available for best interpretation.

2. INTRODUCTION

Estimation of high-resolution seismic velocity models is very important for any aspect of nuclear monitoring. Significant effort is currently devoted to seismic velocity model evaluation and validation, and to developing new, independent seismic model constraints on crust-mantle boundary depth, which have the potential to significantly reduce model uncertainty. Lack of favorable spatial distribution of source and receiver geometries, and in some regions, lack of seismicity, make the estimation of crustal reflector depth difficult. Extraction and interpretation of new crustal depth information derived from stacks of ambient seismic noise autocorrelations is important because it can lead to estimation of crustal reflector depth, independent of the presence of seismicity and of favorable spatial distribution of source and receiver geometry.

The main goals of this study are to develop a method which applies seismic interferometry (Waapenaar *et al.*, 2010) to optimally extract reflection Green's Functions (*GFs*) from stacks of ambient seismic noise autocorrelations and to assess the method performance when estimating Moho depth for multiple types and depths of crust-mantle boundary transitions.

The method developed here is based on a theoretical demonstration (Claerbout, 1968), that "one side of the autocorrelation of the seismogram due to an impulsive source at depth is the seismogram due to an impulsive source on the surface". This conjecture has theoretically been shown to apply (Sanchez-Sesma and Campillo, 2006; Wapenaar, K., 2004) to the recording of ambient noise by co-located source and receiver. Noise autocorrelations were initially used (Lobkis and Weaver, 2001; Larose *et al.*, 2005) to study ultrasonic reflections in a medium. Analysis of the temporal evolution of the autocorrelation function, interpreted as the source-receiver collocated elastic wave *GF* by Wegler and Sens-Schonfelder (2007) was used to study the relative decrease of crustal velocity coincident with the occurrence of a large earthquake in Japan. Other authors also found Moho reflections using autocorrelations of continuous waveforms (Gorbatov *et al.*, 2013). Examinations of ambient noise autocorrelations at the USArray in Nevada (Tibuleac and von Seggern, 2012) have highlighted a prominent arrival at 9-11 sec, which was interpreted as *PmP* (*P*-Moho reflection). A second prominent arrival was observed at ~15- 17 sec, and was interpreted as *SmS* (*S*-Moho reflection). These arrivals were present on all three components. One goal of this study was to develop a physical understanding for these results, by completing a systematic modeling study of the *P/S* reflection response from synthetics propagated in 3D models beneath each station and to compare our results to crustal model and receiver function predictions.

The Moho was first designated as a region of rapid change in the seismic P-velocity by Andrija Mohorovičić. Controlled source seismic data studies have found complexity of reflection characteristics in the Moho vicinity, and recommended interpretations of the transition from crust to mantle on a case-by-case basis, as no reflections are visible in some regions, in others they are single reflections, and in some reflections are complex. In regions where the crust is considerably more reflective than the mantle, the "reflection Moho", which we seek to characterize, has been defined as the deepest, high-amplitude, laterally extensive reflection or group of reflections present at travel times (depths) approximately commensurate with other estimates of crustal thickness (Klemperer *et al.*, 1986). Assuming that Moho was the same everywhere on the continents and was a transition from rocks with basaltic composition to rocks with ultramafic composition, spatially and geologically correlated with the geophysical boundary, petrologists attributed the

Moho either to changes in the bulk chemical composition or to transition in mineral phases. Modern geophysical research has estimated geometric, and thus structural and petrologic, complexities in the vicinity of the Moho. In some regions in Canada this complexity allows interpretations in which the geophysical Moho may be a response to mineralogical changes that are part of a geological continuum and overlie a deeper transition, the true crust–mantle transition, between ultramafic rocks that have different origins.

In this study we test the autocorrelation method at selected stations in regions where Moho is expected to be simple, and in regions of highly variable Moho (Figures 1 and 2).

There is enough body-wave energy in the ambient noise to illuminate crustal features. Seismic array analysis has indicated for a long time (Arrowsmith *et al.*, 2009, Koper, *et al.*, 2010 and references herein), that at shorter periods (0.25 - 2.5 s), seismic noise contains a significant amount of body-wave energy and that coherent short period noise of possible crustal or mantle origin is recorded at the array elements. Other possible causes of body-wave noise may be a range of effects including atmospheric storms (Withers *et al.*, 1996), microseisms, cultural sources (Douze and Laster, 1979), and propagation effects. Hillers and Ben Zion (2011) observed strong seasonal variations of seismic noise amplitudes at frequencies above 1 Hz in southern California. The noise was attributed to variations of temperature and wind at the surface acting directly on topographic irregularities and other surface features, which “could induce multitudinous small-scale failures in the shallow crust.” Seasonal variations of the reflection *GFs* were observed by Tibuleac and von Seggern, 2012, and are discussed in this study.

This study is designed to add independent information to other efforts aimed at building seismic velocity models using ambient noise interferometry results. Three areas (Table 1), of which one in western USA, and two in the central USA were chosen as locations to develop and test the method. Seismic velocity models were previously estimated in these areas using earthquake data, explosions, and ambient seismic noise. A list of seismic velocity models, analysis methods and references available in the study areas is shown in Table 2. These studies have provided estimates of the crustal structure, however, their authors have not focused on extracting information from autocorrelations of ambient seismic noise. The goal of our project is to use the P/S seismic velocity models proposed by these researchers in order to interpret and validate our results. We also assess whether this technique could be used to estimate crustal properties in other regions that are un-calibrated and aseismic.

3. TECHNICAL APPROACH

Algorithms to extract Green’s Functions from ambient noise crosscorrelations and autocorrelations have been developed and are used at the Nevada Seismological Laboratory (Tibuleac *et al.*, 2009; von Seggern *et al.*, 2009, Tibuleac and von Seggern, 2012). The algorithms are closely following the Bensen *et al.*, 2007 method. However, we have included modifications to estimate autocorrelations. Modifications include conversion into velocity records of the same instrument type, i.e. broadband with 0.02 Hz corner frequency and no whitening of the spectra prior to autocorrelation computations. The “sign-bit correction” is applied to all the waveforms prior to autocorrelations.

Using seismic interferometry, we first optimized a method to extract the observed reflection GF 's from continuous seismic waveform autocorrelation beams. This method has been briefly described by Tibuleac and von Seggern, 2012, and is discussed in detail here. Synthetic waveform modeling in deterministic and stochastic models is used to interpret the reflection component of the Green's Function extracted from autocorrelation stacks beneath each selected station. We aim to determine how well our Moho depth estimates correspond to the information extracted from receiver functions, and to other available seismic velocity models.

A three-task research activity has been completed, as follows.

Task 1: *Build a study area database including continuous waveforms, deterministic P/S seismic velocity models, and receiver function information at each station.*

Task 2: *Develop and test the method in a well-calibrated area. Using synthetic waveform modeling, understand the observations.*

Task 3. *Map crust-mantle boundary (Moho) discontinuities in central USA using waveform modeling. Statistically compare with previous estimates and interpret the results in terms of resolution and transportability.*

4. RESULTS AND DISCUSSION

4.1. Task 1: Build a study area database including continuous waveforms, deterministic P/S seismic velocity models, and available receiver function information at each station.

A database of continuous waveforms was built in western and central USA (Table 1). The database includes deterministic P/S seismic velocity models (Table 2) in the vicinity of each seismic station, and receiver function information, as available (Appendix1, Table A1). All stations used in this study had receiver function information, such as P -velocity (Vp), S -velocity (Vs), Vp/Vs ratios and crustal thickness extracted from earthquakes, provided by the Incorporated Research Institutions for Seismology (at <http://ds.iris.edu/ds/products/ears/>, last accessed on April 27 2016).

Three areas were chosen for this study, as shown below:

1. The TEST area (Table 1, Figure 1, plot A) includes stations along the former Consortium for Continental Reflection Profiling (*COCORP*) in northern Nevada, and the three-component (3C), broadband (BB) station *ELK*. The *COCORP* conducted multichannel seismic reflection experiments (Klemperer *et al.*, 1986) which found prominent reflectors primarily between 9 and 11 seconds two-way travel time (TWTT) along the Nevada transect along the parallel 40N. The vertical resolution of the 125sps waveforms, with frequency above 7.5 Hz, was 50-100m. “A striking aspect of the reflection data is the resolution of this group of reflections, in many places, into two distinct reflections as much as 1.2 s (~ 4 km) apart, which elsewhere merge into a single reflection.” The authors suggested that “These two reflectors might represent the top and bottom of a transition zone at the base of the crust”. The pair of Moho reflections may be explained as reflections from layers within a velocity gradient zone, with gradient varying from 0.1 km/s/km to

1 km/s/km at the refraction Moho, with a velocity gradient of 1 km/s per km depth. One question we tried to answer was whether our method can distinguish these two reflections. Klemperer *et al.* (1986) found that the reflection Moho beneath the Basin and Range generally corresponded with the refraction Moho, and that the Moho was relatively flat beneath the entire Basin and Range, and marked by distinct reflections (as opposed merely to the cessation of lower crustal reflections)

The well-characterized area of the *COCORP* experiment has been chosen to test the method because it was within ~ 50 km of line “O” of continuously recording broadband stations from the USArray EarthScope Transportable Array (TA). The “O” stations (Appendix 1, Table A1.1, Figure 1, plot A, and Figure 3) deployed from 2006 to 2008. Along this transect, according to Klemperer *et al.*, 1986, TWTT of the Moho reflections vary from 9s at 118W, to 10s at 115W, increasing to 11s at 116.5W (Figure 3, lower plot). A compilation of Nevada velocity models (Figure 3) was available at the Nevada Seismological Laboratory in the TEST study area, including *P/S* velocity models extracted from ambient seismic noise and earthquake analysis (Tibuleac *et al.*, 2013), as well as other publicly available models (Table 1).

2. An area with “simple” Moho (SIMPLE, Table 1, Figure 1, plot B). The second study area includes TA seismic stations (Appendix 1, Table A1.1b) deployed in New Mexico, Texas and Oklahoma, where Moho anisotropy models and receiver function data are available at non-tectonic, non-sedimentary locations (Shulte-Pelkum and Mahan, 2014). Shulte-Pelkum and Mahan, (2014) estimated that no significant dipping interfaces and anisotropy and no significant Moho velocity variations were observed in this area.

3. A third study area (COMPLEX, Table 1) was chosen in an accessible and well – resolved region, the Mid-Continent Rift in Central US, because of the presence of Moho complexities which usually affect the crust-mantle boundary depth measurements (Shen *et al.*, 2013). The complex structure in this region resulted in large time-averaged uncertainty in receiver functions, and one question we addressed was whether our method can resolve similar crustal variations and distinguish local Moho complexity. As estimated by Shen *et al.* (2013), this region has a thick crust (>47 km), a gradient Moho in the northern part of the rift, a sharp Moho in the south and significant anisotropy.

Due to time and scope constraints, only selected stations in the SIMPLE and COMPLEX area were analyzed in detail.

4.2 Task 2: Develop and test the autocorrelation method in the TEST area in western USA. Using synthetic waveform modeling, understand the observations.

This task was separated into two subtasks:

4.2.1 Develop optimal algorithms for GF extraction in the TEST area in western USA, at TA stations installed in the area of the COCORP profile. Apply ambient-seismic noise autocorrelations to each available sensor in this area, with the purpose to identify and extract the *P/S* reflection component of the Green's Functions (GFs); Develop a procedure for identification of reflection GF *P/S* arrivals.

A database of two years of continuous waveforms was collected in 2006-2008 at three-component broadband stations of the USAArray (Appendix 1, Table A1) in the TEST area, and at BB, 3C stations ELK and ELFS. ELFS was chosen as an additional station in the Sierra Nevada Range, such that the results could be compared to results at O05C. ELK (near TA station N11A) was chosen because of an expected “simple” crust-mantle boundary, and because it recorded all the earthquake sequences discussed at 4.2.2.6. The following is a detailed description and discussion of the *GF* extraction from stacks of autocorrelated waveforms.

4.2.1.1 Process ambient seismic noise at all available sensors and extract autocorrelation stacks

The first step consists of building a database of “sign-bit” (Bensen *et al.*, 2007) corrected day-long files for each year (named here “*gf*”). To avoid artifacts due to conversion to displacement (Anderson *et al.*, 2009), the instrument was removed and the waveforms were converted to broadband velocity, of analyst – chosen corner frequency (0.02Hz in this study). This is achieved by multiplication of the spectra with a ratio of frequency domain transfer functions. Because for the TA sensors the transfer function has two poles, of which one is in a frequency range beyond the band of interest, we only use only the pole in the frequency band of interest when the transfer function ratios are formed. An analyst-chosen window is applied in the frequency domain to assign zeros to the spectra in the vicinity of minimum and maximum frequency values. Pre-filtering is an option at this stage, and is discussed below. “Sign – bit correction” is subsequently applied to the resulting waveforms.

The *gf* database is processed at step two, when daily (or shorter length) autocorrelations are stored in a new database (named here “*gfo*”). The autocorrelations are estimated in the spectral domain by multiplying the Fourier transformed waveform with its own complex conjugate. The database *gfo* contains a window (1300s in this study) of the causal side of each *GF*. Prior to autocorrelations, the analyst has options for pre-filtering, downsampling, for choosing the time length of the continuous waveforms to be autocorrelated, for choosing the amount of window overlap and whether or not whitening is applied to the spectrum. These options are discussed below. Spectral whitening was not applied in this study.

The third step consists of stacking the waveforms in *gfo* to extract the reflection component of the *GF* at each station. A third database, named here “*gfstack*”, is created. Waveforms are stacked based on an innovative selection criteria. Assuming that the extracted reflection *GFs* should be the same every day, an option exists to compare daily waveforms in an analyst – chosen window (named here “*ACW*”) and to quantify their similarity using crosscorrelations. Note that zero – phase filtered *ACWs* of the *GFs* extracted for each interval, and not the raw waveforms are crosscorrelated at this step. An option exists to apply a threshold to the crosscorrelations maximum values such that only the *GFs* with the desired similarity in the *ACW* are stacked. This option is always used, at a threshold at least zero, to eliminate negative crosscorrelation values in the *ACW*. The results of thresholding are illustrated in Figure 4. After thresholding, it is shown that *GFs* at station O11A show higher “signal” amplitude, observed at all frequencies, however only shown in the 1-2 Hz (Figure 4, upper plot) and 0.5-1 Hz intervals (Figure 4, lower plot). This feature is useful when the signal arrival time and the frequency band are estimated correctly, however, it has the disadvantage of stacking less waveforms (only one third of the daily *GFs* met the criteria for

0.22 threshold in Figure 4B) and when the expected signal features are not known, possibly removes useful information.

Matlab[®] algorithms were created to extract and plot GF's from ten-day stacks to better identify reflection GF arrivals. These algorithms were used to investigate filtering techniques and autocorrelation beam analysis techniques with the goal to improve resolution, and to pick statistically significant arrivals.

Ideally, the *PmP* and *SmS* arrivals should be consistent in each 10-day beam at the same station. An *F*-detector (Blandford, 1974) was evaluated, to detect seismic signal in ten-day *GFs*. Blandford stated: “the essence of the *F*-detector output is the power on the beam divided by the average over all channels of the power of the difference between the beam and the individual channel seismogram”. Using these algorithms, we also investigated the best approach for *PmP* and *SmS* arrival identification once the reflection component *GF* was extracted.

The TEST area reflection GFs are shown in Figure 5 (stacking threshold 0.22), for two different Continuous Wavelet Transform (CWT) center periods (1.7 Hz and 3.4 Hz) of a *gaus5* (Figure 6) wavelet and for the case when the Fourier transform for 0.29-0.42 Hz was applied before Automatic Gain Control (AGC). Forty seconds following the autocorrelation maxima for positive lags at all the processed TA stations are shown. In 2012, Tibuleac and von Seggern, found, for most TA stations in Nevada, two clear arrivals, at ~9-10 s (named “the 10-s arrival”) and ~16 s (named “the 16-s arrival”) time lags are observed. This is consistent with reflections from a Moho discontinuity ~ 30-35 km deep. The 10s arrival is at approximately the two-way travel time of a *PmP* (Moho) reflection, and has inverse polarity when compared to the autocorrelation maxima (for the IASPEI91 velocity model with a 30-km-thick crust). The ~15-16s arrivals are consistent with two-way travel times (TWTTs) of an S-wave Moho reflection. Similar two-way travel time values (9-11 s) are estimated for the Moho reflections in this area by other authors (Klemperer *et al.*, 1986) although no later arrival is mentioned in these studies at ~ 16 s. Unlike *PmP*, which has TWTT (Two Way Travel Time) within 1s across Nevada, the *SmS* TWTT is more than 1s slower at stations in central Nevada. This is expected considering independent information of lower crustal, relatively low P and S-velocity across the TEST area (Figure 2, upper plots). Complex *GFs* were observed at stations ELFS, O05C and O13A, all in mountain ranges. The *GFs* at these stations vary significantly and differ from the rest of the line “O” when the center period is increased, and are discussed in detail at 4.2.3.1.

In Figure 5, an additional, strong arrival is present on all three components at ~ 23s (26s in the mountain areas) when waveforms are Fourier-filtered (plots G, H and I) in a lower frequency band. This arrival was also observed for CWT, *gaus5* at 5s center period. The arrival at 23s could be interpreted as a ~60 km deep discontinuity P- reflection (Priestley and Brune, 1978). These authors obtained a model of the Great Basin of Nevada and Utah from inverting the dispersion of fundamental mode Rayleigh wave (4- to 120-s period) and Love wave (4- to 40-s period) phase velocities. “This model consists of a three-layer, 35-km-thick crust and a 29-km-thick, higher-velocity ($V_s = 4.5$ km/s) cap at the top of the mantle, below which lies a broad (180-km-thick) low-velocity zone for shear waves ($V_s = 4.05$ –4.12 km/s). Intermediate-period (15- to 32-s) Rayleigh wave phase velocities measured over shorter paths indicate the existence of significant

local variations in the shallow (20- to 30-km-deep) structure which may result from varying crustal thickness or varying depths to a zone of partial melting.” Priestley and Brune interpret these areas of the Great Basin as a tensional region where deep mantle material has intruded near the surface and created a zone of partial melting.

CWT center period. In this study, wavelet filtering was preferred to Fourier filters, however, it is recommended that the results are compared, specifically when the best wavelet is chosen for the area. The CWT has the ability to filter in very narrow frequency bands, which appear to be characteristic to reflections from crustal layers. Using CWT *gaus5*, *PmP* was observed starting at center periods of 1 Hz. Wavelet analysis has disadvantages which are discussed below.

The optimal center period required for *PmP* and *SmS* identification is expected to increase with the crustal reflector depth, possibly related the low-pass filter effect of the earth on seismic waves traveling to the surface. As shown in plots G-I in Figure 5, arrivals interpreted as P-reflections from deeper layers are resolved when *GFs* are filtered at lower frequency. The center period is important, because the shorter the period, the better the resolution of the reflection picks and the shorter the wavelength of the Moho reflection. However, as shown in Figure 5 (station O08A), there is a large probability that the short periods would be contaminated with cultural noise. For a two second period the error is empirically estimated at 1 s. An error of 1s translates in ~6 km crust-mantle boundary error for a 35 km crust, when using the IASPEI91 velocity model. Other post-filters are discussed below, as it is recommended that the best filters are chosen specifically for each station and each Moho depth.

CWT using different wavelets (Figure 6A) may result in similar relative arrival times, however, it also results in systematic absolute arrival time shifts, which are larger for longer center periods (Figure 6B). Figure 6B was generated by picking the negative maximum of a synthetic delta function at a known time, embedded into a normalized random time series. The synthetic time series was then CWT-filtered with a set of wavelets at center periods from 0.5s to 5s and the largest negative peaks were picked automatically. Unlike all the wavelet filters, the zero phase, three pole Fourier filter centered on an interval of half a period around the value of each center period results in automatic picks which are closest to the “true” time lag. TWTT corrections were applied later, using the information in this figure, when picking arrivals after CWT *gaus5* filtering.

Figure 7 shows that the reflection *GFs* provide Moho reflection TWTTs comparable to active source experiment values, in the TEST area. In this figure, the UNR analyst-estimated (UNR-TWTT) two-way travel times for *PmP* (upper plot) and *SmS* (lower plot) are compared with the COCORP-TWTT interpolated from Klemperer *et al.*, 1986, and with travel times derived from EARS receiver function data (EARS_TWTT). Comparisons for CWT and Fourier filters are shown. Note relatively good correspondence of the UNR-TWTT and COCORP TWTT, while the UNR_TWTT and EARS_TWTT significantly differ in the case of S-arrivals (see also Appendix1, Table A1a) at stations in the Sierra Nevada (ELFS and O05C), at O09A, located on top of the ‘Battle Mountain Heat Flow High’ (Williams and Sass, 1997) and at O13A, also located in a mountain range. Comparisons of the Fourier and CWT (*gaus5*) at every station showed systematic CWT TWTT differences when compared to TWTT from a zero-phase Fourier transform. To obtain a Fourier P-TWTT, 1.24s (using the median value) must be added to P-TWTT from CWT with

gaus5, while Fourier S-TWTT is obtained by adding 1.8s to S-TWTT estimated after CWT gaus5 at 1.7s center frequency. Unless otherwise specified, in the discussion below corrections have not been applied to TWTT measurements.

After many of the measurements were already made, it was found that the best Fourier-CWT correspondence actually occurs in the TEST area at 1.7s for the CWT with db5 wavelet (see also Figure 6B). Because corrections were available, and because the *PmP – SmS* arrival delay was not affected by the type of wavelet, *gauss5* CWT continued to be used in most of the examples. It is however, recommended that, where possible, Fourier picks are used.

4.2.1.2 With the goal to improve resolution and optimize analysis, investigate optimal processing, filtering, arrival picking and identification, analysis time length, seasonal reflections, natural earthquake occurrence, multiple filtering techniques, and autocorrelation beam analysis techniques.

4.2.1.2.1 Pre-filters. An option is available for applying pre-filters (prior to autocorrelations) and has been used effectively for Rayleigh wave extraction. Pre-filtering has been evaluated for reflection *GF* extraction at station O11A, as shown in Figure 8. Figures 8A and 8C show the ten-day stacks of autocorrelations in the case when no pre-filter was applied at Step 1 (at 4.2.1). Note that the *PmP* and *SmS* are clearly identifiable in these plots as single arrivals, and the *F*-statistic representations in Figures 8B and 8D show detections at ~9s, respectively ~16s. Figures 8E and 8G show the same ten-day stacks, with the difference that a 0.3Hz to 4 Hz Butterworth, zero phase, eight pole pre-filter has been applied at Step 1. Note possibly split *PmP* arrivals at 9-11s and split *SmS* arrivals at 15-17s. If Klemperer *et al.*, 1986 did not observe split *PmP*, and if the results in Figures 8A and 8C were not available, it would be difficult to identify the arrivals in Figures 8E and 8G, although the *F*-statistic correctly identifies the presence of arrivals at similar times in Figures 8A and 8C. The *GF* changes during the summer, however, are easier to observe in plots E and G, and look similar to simulation of a seismic source recorded at different angles, as discussed at 4.1.1.

Figure 8 shows that pre-filtering may reveal Moho complexity, if the double arrivals are interpreted as in Klemperer *et al.*, 1986. *PmP* and *SmS* are, however, harder to identify when using the pre-filtering option. As shown below, *PmP* and *SmS* splitting is also observed when large teleseismic activity illuminates the crust.

The *F*-statistic is estimated in a window (*FW*) twice the center period, moving with a step of one sample point and the *F*-statistic value is assigned to the center of the *FW*. A filter is applied to remove the phases which are not of opposite polarity to the maximum value. The *F*-statistic can be used for arrival confirmation and picking. Also, when an arrival is present, it appears at multiple CWT scales (or center periods). This information can be used to identify coherent arrivals and could possibly be used for arrival picking, when properly calibrated.

4.2.1.2.2. “Post-filtering” (ie after autocorrelation and stacking) period, sample rate, wavelet type. It was observed that improved *GF* frequency band was obtained using waveforms at the original sample rate, versus using decimated data. Improved frequency content is desirable for increased reflection *GF* resolution. In this study of deep crustal reflections, the waveforms are

decimated to 20sp, as a tradeoff exists between larger computation time, limited memory resources and the resolution gain of a 10 Hz Nyquist frequency versus a 20 Hz Nyquist frequency.

Wavelet filtering For signals with narrow frequency band, such as the *GFs* extracted from stacks of crosscorrelations, or autocorrelations, Continuous Wavelet Transforms (CWT) show more signal features when compared to narrow band Fourier filters. The wavelets “db4”, “db5”, “sym5”, “gaus5” and “morl” (Figure 6) have been tested. For ideal filtering, the wavelet shape should be similar to the signal shape. Wavelet transform filtering identifies objectively a seismic phase localized in both time and frequency. Arrivals are identified by CWT when the signal is too narrowband, as opposed to the Fourier transform, however, CWT is not zero phase, and $\pm 1\text{-}2\text{s}$ differences have been observed in arrival picks when compared to zero-phase filters (as discussed in Figure 7 and later in chapter 4.2.1).

Figure 9 shows examples of ten-day beam analysis at station O11A when using the wavelets in Figure 6, with 1.3s and 2s center period. Analysis using a Fourier filter is also shown. The 1.3s period is the shortest period at which *PmP* arrivals are clear enough to be recognized. The wavelet “gaus5” was chosen for illustration of the method, as a wavelet closely resembling the expected signal, however, db5 would have also been a good choice. Other wavelets may be optimal in other regions. The symmetrical “morl” wavelet (Figure 9 B,G) was effective in extracting the extra energy during the summer time (approximately days 150-250). The sym5 wavelet produces similar results with the gaus5 wavelet. Comparison to Fourier filtered *GFs* (Figure 9, plot K) may help when choosing the best wavelet.

4.2.1.2.3 Seasonal reflections Significant seasonal reflections are observed at all TA stations during the summer months (days 150 to 250) as shown in Figures 8 and 9 (black rectangles). Seasonal variations are also shown in Figure 10, for a representation with ten day stacks at station O11A on all three components using the *gaus5* wavelet. The rightmost two waveforms in each plot are the *GFALL* (the stack for the whole period) and *GF2006360* which is the daily *GF* for a day with intense teleseismic activity, as discussed below. The seasonal variations are best seen on the N-component at this station. Polarization analysis shows that the seasonal variations are correlated with variations of the daily predominant P and S angle of incidence and with variations in azimuth.

The seasonal reflections are possibly the result of high frequency (around 1 sec) microseismicity “illuminating” crustal layers, as opposed to being expressions of the 5-6 sec microseism dominant period. Minimum seismic noise is observed in the winter months for frequencies around 1 Hz and maximum seismic noise is observed in the winter months for periods of ~ 6 sec (Harben and Hjortenberg, 1993). To better illustrate seasonal variations, in Figure 11 the stack for the whole period, *GFALL* (the right red trace) was removed from each ten-day stack. Figure 11, plots A-C and G-I are the same as in Figure 10. The results at two CWT center frequencies are shown in plots D-F (center period 1.3s) and plots J-L (center period 2s). Two reflections are observed during the summer months (black rectangles) at $\sim 6.5\text{s}$ and at $\sim 13\text{s}$. One interpretation is that these arrivals are multiple reflections from a mid-crustal layer. Thus, mid-crustal layers are best illuminated by the relatively higher frequency noise observed during the summer months, while deeper layers are illuminated best during the winter months, when longer period noise is dominant. Another

interpretation is that these arrivals are P and S-arrivals reflected on a mid-crustal discontinuity. Because the summer arrivals are affecting the *GFs*, further analysis is necessary to correct for, and use this information for better constraints on crustal models.

4.2.1.2.4 Processing time length, overlapping windows

It has been demonstrated (Bensen *et al.*, 2007) that the *GF* frequency content improves when analysis is performed over longer periods of time. Processing of overlapping windows has been investigated in detail by Seats *et al.*, 2012, for crosscorrelations of ambient seismic noise. These authors compared the waveform convergence of short duration stacks (e.g. 2, 5, 15 and 50 day stacks) towards the long-term (365 days) noise correlation function (NCF) stack, after applying Welch's method for non-pre-processed and running normalized time-series. "Correlating 30 to 60 minute windows of data and overlapping these windows provides a more robust quicker converging NCF than using daylong time windows or other preprocessing techniques". No similar study is available for autocorrelations.

In this study, a qualitative comparison also shows that by using one hour, 50% overlapping, windows the period of analysis could be reduced from two years to six months or less, when information is desired at frequencies less than 2 Hz, which are the frequencies at which deeper crustal layers have been observed so far. These results are shown in Figure 12 at station O05C. The lowermost waveform on the left is synthetic, for the O05CUNR model shown in Appendix1, Table A1.3. An arrival at 12s is identified as *PmP*.

Each ten-day stack (Figures 8-11), with no time window overlapping, shows results similar to the *GFALL*. In-depth analysis similar to the work of Seats *et al.* 2012, and investigation of additional pre-processing methods, such as Welch's method, would be of use for best estimates of the minimum stacking time.

GF2006360 in Figures 10 and 11, as well as additional results discussed at 4.2.2.6, suggest that the stacking period may be reduced to one day in the case of intense crustal illumination by teleseismic energy. Caution, however, and additional investigation are suggested at 4.2.2.6 when using long-term local and regional sequences, which have the potential of introducing autocorrelation periodicity not related to the reflection *GFs*.

4.2.1.2.5 Investigate the best approach for *PmP* and *SmS* arrival picking and identification once the reflection component *GF* was extracted.

Arrival identification and picking remains the most difficult issue, which needs to be addressed by using multiple sources of geophysical information in the respective region, nearby station investigations, station *GF* patterns for shorter periods of time (10 or 20 days in this study), as well as synthetic waveforms and polarization analysis. As shown in Figure 5, plots M-P, multiple types of filtering show almost similar results, and the *PmP-SmS* arrival time lags have the same difference, however, the absolute values depend on the type of *post-filter* (see also Figure 7). If the interpretation of deep Moho at the ELFS, O05C and O13A stations is correct, arrival identification is made difficult by the presence of arrivals in the vicinity of 10s and 15s, with only subtle differences from observations at the other stations in the Great Basin. For instance, the ~15s

arrivals in the black boxes should be PmP . GF inter-station differences (see red circle in plot O) are observed when using longer periods (in this case 4.5s) for post-filtering. Because of relatively high variability of the crustal structure at local distances, large aperture arrays (or lines) may be more useful for deep crust arrival identification when filtering the GF s at longer wavelengths (> 3.4 s period).

In the ideal case of flat layers beneath each station, the PmP would be present only on the vertical components. As shown in Figure 10, the horizontal components also show clear arrivals at ~ 9 - 10 s. In turn, vertical arrivals are observed at ~ 16 s, where only SmS arrivals should be present. For 30km deep crust in the Basin and Range our interpretation is that, as the 10-s arrival represents non-vertically polarized P -waves, the 16-s arrival is a manifestation of non-horizontally polarized S -waves. More intriguing, estimates of GF cross-terms (EN , EZ , NZ) at O11A were very small amplitude (1%) when compared to the E , N and Z GF ALL amplitudes. This shows that the E , N and Z GF components can be considered independent of each other. In this case, polarization reflects an average energy trend over a long period of time, and not the characteristics of a single plane wave. GF “polarization” and arrival frequency content are discussed in this paragraph.

Polarization, rectilinearity and incidence angle in 2.6s windows, with a step of one sample point, at station O11A, are shown in Figure 13 (plots B1-B4) as a function of time. The waveforms were CWT filtered, centered on 1.3s, with a *gauss5* wavelet. The “incidence angle” is $\sim 40^\circ$ - 45° in the 2.6s window starting at ~ 9.5 s. High planarity and linearity indicate a P -phase arriving at \sim zero azimuth. The relatively large PmP incidence angle measurement is in agreement with observations by Larkin et al., 1997, that in the Basin and Range province PmP is often observed only at offsets near and beyond the critical distance. This observation was explained by Larkin et al., 1997 as a manifestation of rough Moho. Increased presence of shear waves starts at ~ 14 s (center of the window, shown as a gray area), indicated by large angles of incidence ($> 70^\circ$) and $\sim 90^\circ$ azimuth.

Arrival picking In this study, an analyst has chosen the best filtering wavelet, then used the F -statistic to confirm the PmP and SmS arrivals, and picked the maximum amplitude for each arrival. Ten-day stacks are used to identify PmP and SmS for complex GF cases, and an F -statistic is estimated for each period. An “arrival” should be present at multiple periods (the periods should be in an interval within $\frac{1}{2}$ of the period length). Note that the error in arrival estimation increases with the increase of the F -statistic window, which was chosen as an interval twice the center period. Figure 14 shows this procedure at station O11A. Note that in each window only beam waveforms with inverse polarity compared to the autocorrelation maximum were considered for F -statistic calculation, all the other waveform amplitudes were replaced with zeros.

4.2.2 Natural earthquake waveform amplitudes. Due to the “sign bit” (Bensen et al., 2007) conversion, we only retain the waveform phase, and not the amplitude. Thus, the natural earthquake waveform amplitudes are not expected to significantly influence our results. Illumination of the crust with earthquake seismic energy, however, has the potential to result in improved resolution. One question answered in this sub chapter is whether analysis of two years of data could be avoided, and resolution could be improved by using just one, or a limited number of days of strong earthquake activity.

Large teleseismic sequences are the source of significant scattering in the crust, usually in the 1-3 Hz energy band. This is a band of energy significantly diminished due to summation to form stacks when extracting the *GFs* from ambient noise, resulting in lower resolution. The *GF* extracted on a day with significant teleseismic activity, processed in the same way as two years of data, was compared to the *GFALL* with encouraging results, as shown below.

On December 26, 2006 (Julian day 360) two large earthquakes of magnitudes 6.9 and 7.1 occurred in Taiwan, at 12:26:21 UTC, and at 12:34:14 UTC, at depth < 10 km, followed by a magnitude 6 earthquake in the Kuril Islands, three hours later, at 15:19:45 UTC, at a depth of 10 km. This enhanced teleseismic activity was recorded by the TEST array and processed using the same parameters as for the 2 years of data from 2006 to 2008. A daily *GF* was extracted at each TEST area station in 2006, day 360 (named *GF2006360*) and was compared with the *GFALL* in Figures 15 and 16, at two periods, 1.3s and 2s. *GF2006360* extracted at O11A was also shown for comparison to *GFALL* in Figures 8-11. The pair of *PmP* – attributed arrivals (Klemperer, *et al.*, 1986) is observed for *GF2006360*, however, is less clear for the *GFALL*, which lacks high frequencies. The *GFALL* shows the *PmP* arrival at ~9s, as observed by Klemperer *et al.*, 1986, while the ~9s and a second, larger arrival (at ~11s) is clearly seen in the *GF2006360* representation, when the crust is illuminated by seismic signals of a broader frequency band than the *GFALL* band. These observations suggest that one day of significant teleseismic activity is as valuable as two years of data, mostly in regions with complex crustal structure, however, this finding needs to be tested in more detail. In this study, a day with high teleseismic energy has been found for every station, and was compared to the *GFALL* for arrival identification purposes. For the entire TEST area *GF2006360* has been used. If other days were used, they are mentioned in every figure caption.

Large local and regional seismic sequences Could promising results for teleseismic energy mean that short periods of high local and regional seismicity could also be used to reduce the computation time? To investigate this possibility, two large earthquake sequences that occurred in the first quarter of 2008 in eastern and Western Nevada were analyzed. A 6.7 km deep magnitude M_L 6.3 earthquake occurred in Wells, NV, at 4.1 km depth, on February 21, 2008, at 41.153°N and 114.867°W. The activity continued for several months, with at least eight M_w 3.8 to 4.2 aftershocks. The *GF* for the day of the main shock of this sequence is named *GF2008052*. The main shock of the Mogul, NV sequence, of magnitude M_w 5.0, occurred on April 26 2008, at 2.8 km depth, at 06:40:10 UTC, at 39.523N, 119.939W. The *GF* extracted on the main shock day is named *GF2008117*. As the USArray was being removed from Nevada at the time of these two sequences, only few stations recorded both earthquakes, and some only recorded one sequence or the other.

ELK, a broadband station located at 55 km distance and 35 degrees back azimuth from Wells, and at more than 500 km from Mogul, recorded both sequences, thus was chosen for analysis, although it was not at the same latitude as the other stations in the TEST area. The same representation as in Figure 11 is shown in Figure 17 at station ELK, however, only for the 2s CWT center period. Unlike in Figure 11, three one day stacks are subtracted from the 10-day stacks: *GF2006360* (discussed above), *GF2008050* and *GF2008117*. The *GF2006117* looks like the ten-day stacks during the summer months. This figure shows that natural seismicity can systematically have

periodicity within 6-20s if repeatedly occurring in a local or regional range. It also shows that a very shallow crustal sequence such as the Mogul, NV earthquakes, would provide information on what we interpret as shallow crustal reflections, otherwise visible only during the summer.

Figure 18 compares, for each selected station, the *GFALL* with *GF2006360*, *GF2008052* (the day of the Wells main shock) and *GF2008117* (the day of the Mogul earthquake). The *GFALLs* at stations O06A (brown), O07A (green) and ELK (cyan E, blue N and magenta Z) were filtered using CWT, gaus5, centered on 1.3s (plot A) and 2 s (plot B). The Wells earthquake was recorded at all three stations, however, the Mogul earthquake was only recorded at ELK. The Z-component *GF* is shown at O06A and O07A, and the E, N, Z components are shown at ELK. Good correspondence of the *GF2008052* and the *GFALLs* at O06A and O07A is observed, possibly due to larger epicentral distance (> 500 km). Also note good correspondence of all three daily *GFs* and the *GFALL* on the Z-component at ELK, and on the N-component (except for *GF2006360*, contaminated probably by cultural noise). Worst correspondence of the *GF2008052* and *GF2008117* and the *GFALL* is observed on the E component. The shear wave energy from both earthquake sequences in 2008, which was the dominant energy, was oriented roughly along the ELK N-component.

These observations suggest caution when using local and regional sequences, however promising results and a direction for further investigations.

4.2.3. Interpret the results in terms of crustal properties, crustal reflectors and crust-mantle boundary depth using synthetic GF reflection components propagated in composite 3D models (deterministic and stochastic).

An interpretation puzzle in the TEST area is the fact that *PmP* and *SmS* are present on the vertical, as well as on the horizontal components. Ideally, for zero-offset only the phases with vertical propagation should be present in *PmP* and *SmS* should be horizontally - polarized. Tibuleac and von Seggern (2012) proposed as possible explanation the contribution to these arrivals of ambient noise from a spatial "cone" beneath the stations or the ambient - noise scattering in the layers immediately beneath the station. Another issue is the recognition and picking of *P* and *S*-arrivals, which, as shown below, is relatively difficult, especially in regions with thicker crust. We use waveform modeling to address these questions, however, a more detailed investigation, not allowed by the scope and time of this study, is necessary.

The finite-difference code named *sw4* (Petersson and Sjogreen, 2014), is used to propagate synthetics in composite 3D models (deterministic and stochastic). The results are interpreted in terms of reflection *GF* phase composition, crustal structure, crust-mantle boundary depth, and crustal reflector properties.

Simulations have been performed in two stages.

In the first stage, point sources, linear, and randomly distributed sources were placed at 0.001km, at 35 km (to simulate scattering from Moho), 45 km and 80 km (to simulate teleseismic arrivals) in deterministic and random models, as discussed below. The synthetic waveforms generated for sources at 1 m depth were considered an acceptable approximation of the Green's Function at each

station. All the cases with sources at other depths than 1 m were processed as described at 3.2.1.1. For deterministic, and deterministic with random variations superposed models, generation of PmP and SmS on the three components has been investigated. Emplacement of sources at several depths within the crust, and in multiple configurations have also been investigated, as well as the effect of non-zero angles of incidence.

The second stage was a first – order Moho depth estimation using forward modeling for the TEST (and later for selected SIMPLE and COMPLEX) area stations. The receiver function models in Appendix 1, Table A1.3 (named starting with “RF”) were used together with UNR-derived models (named starting with “UNR”). In-house models were available from previous Nevada studies at the TEST stations.

These simulations represent only a first-order evaluation. A systematic, larger scale investigation using stochastic models is recommended to best understand the influence of heterogeneity on 3C arrivals.

4.2.3.1. Investigate 3C GF generation using deterministic, and deterministic with random variations superposed models, and sources with various configurations and depths

Models Thirty second records (for the TEST area) or fifty second records (for the SIMPLE and COMPLEX areas) were simulated in a 3D model with a grid cell size 200 m. Each model is a cube with a side length of 100 km, and has a super-grid damping layer of 30 grid points. Models used for the deterministic analysis are shown in Appendix 1, Table A1.2.1 The type of source was “C6SmoothBump”. The *freq* parameter, ie the frequency content in the time function, was set to 1, thus the highest significant frequency was 3 Hz.

Table A1.4 shows the location of the 3C virtual stations, within 100 km, with inter-station distance of 15 km. Two groups of six virtual stations were located on lines perpendicular to each other, and one virtual station (BB) was located in the middle. The possibility for simulations of sources located at different angles from the vertical from a station were the reason an array, as opposed to one station was chosen. A 2D array is most useful when studying directionality effects in random fields.

To test the effect of random velocity models added to the deterministic models, the *sw4* “randomize” command was used to make random perturbation of the material velocities, Vp and Vs , according to $Vp = (1 + A(z)T)Vp$ and $Vs = (1 + A(z)T)Vs$ where T is a random field with $-1 < T < 1$. The perturbation amplitude was constant, with $A(z)$ from 0.1 to 0.3. The aspect ratio of 2:1 was used for correlation length on the horizontal (0.8km or four grid intervals) when compared to the correlation length on the vertical. This approach was a convenient first-order investigation, as it was a built-in feature of the *sw4* codes, however, a systematic investigation using stochastic models is recommended. Larkin *et al.*, 1997 used an aspect ratio of 4:1 in the mid-crust to Moho depth range and a correlation length of 240m to model a stochastic crust in the Basin and Range. These authors also suggested “high impedances and/or horizontally oriented seismic fabrics” as a possible cause of high-amplitude reflectivity observed at middle-crustal (12–20 km) levels in the Basin and Range.

GF data was modeled by positioning the source close to the surface (at 1 m depth). Wide-angle refraction data were simulated by placing the source into the lower crust or at Moho level. “Teleseismic” data were generated by having a line or point source beneath the target zone, at 45km or 85km depth.

Searching for an optimal source type to model the observed GFs point source, line source and circular sources were investigated. The sources were unit forces with components on the X , Y , Z axes (f_x , f_y and f_z).

When the source was 1m deep, below the BB central virtual station, difficulties were encountered in extracting the synthetic GFs at any other stations than the BB center station, in deterministic models. In addition, Rayleigh waves contaminated the signal in the first ~10s for virtual stations away from the BB center station, independent of the type of source.

The autocorrelation of the transmission response should be the reflection response (Claerbout, 1968), thus, an 85km deep **point force source** should be effective for GF extraction. As shown in Figure 19, is possible to extract mid-crustal (25km deep) vertical reflections at station BB for a unit point force source at 85 km depth, however, the arrivals have low amplitude. Simulations with only horizontal, or only vertical unit forces were useful to identify 25km P and S reflections, however, PmP was not retrieved. As predicted by model $M2$, the 25km P reflection TWTT should be 8.7s, PmP is expected at 11.36s, the S-reflection from the 25km deep crustal layer is expected at 14.8s and SmS is expected at 20s.

The results when using the model $M2$ and **randomly triggered unit point-force sources located on a circle with radius 1m**, with the center on the vertical to station BB, at 1m and 85 km depth, are shown in Figure 20. The sources are either horizontal (plots A-F) or vertical (plots G-I). When these sources were at 1 m depth, no distinguishable GFs were extracted (plots A-C) except at the BB station. Sources at 85 km depth, however, produce SmS at some stations away from station BB even when they are all vertical. Double arrivals are observed on the vertical components when the model is deterministic (plots G-I), however, double arrivals and the reflections from 25 km are not visible in plots D-F when a random model is added to the deterministic model. Note that the random model was generally faster than the deterministic model, resulting in slightly earlier reflections.

When **200 m apart sources start in the same time in a line** along the X -axis, at 0.001 km and 45 km deep, in a deterministic model, reflections are retrieved on the Z component even if sources are only horizontal, as shown in Figure 21, A-C. Note that the largest arrivals within the first 10s on line 2 (plot B) are identified as Rayleigh waves. The rightmost waveform is the “BB” station, which is located in the center of the array. The model $M2$ used in Figures 19-21 produces a significant reflection at 25 km depth (Figure 21, A-C and D), which may explain the “double arrivals” observed by Klemperer *et al.* (1986) and observed at some of the TEST stations. The S-reflection from the 25 km deep layer is less clear in all plots except for F and the SmS is best seen in plot E, black rectangle at ~ 20s.

Based on the synthetic waveform investigations described above, “double arrivals” observed by Klemperer *et al.*, 1986 in the TEST area could possibly be explained by reflections from a strong

reflector at ~ 25 km in the crust, or by topography of crustal layers, which could have effects similar to localized, randomly triggered circular sources. When random models are added to the deterministic models, the energy is redistributed from the vertical reflection GF to the horizontal components. These are only first-order investigations, and an in-depth analysis is recommended, using stochastic models with better control on crustal heterogeneities. Effects of scattering near the surface and of topography should also be evaluated, as well as effects of converted phases.

4.2.3.2 Comparison of observations with synthetic waveforms in the TEST area.

O11A. Moho depth is estimated at 33 ± 0.4 km (Appendix 1, Table A1.1a) in the Sierra Nevada beneath station O11A, with Vp/Vs of 1.76. Figure 22 shows observed and synthetic results at O11A for 1m and 45 km unit force, point sources and for a line source along the X axis. The modeled PmP (10s, 40° incidence angle in Figure 13) and SmS (17.5s, $\sim 90^\circ$ incidence angle in Figure 13) qualitatively correspond to the observed arrivals, when filtered with CWT gaus5 at 1.7s. Random perturbations were added to the deterministic model M2 Appendix1, Table A1.2 as shown in the figure. Note that the modeled SmS is faster (within 1s) than the observed SmS when using a random model.

Station ELFS Moho thickness is estimated at 50 ± 1.2 km (Appendix 1, Table A1.1) in the Sierra Nevada beneath station ELFS, with Vp/Vs 1.67. The results shown in Figure 23A show that observations and synthetic waveforms confirm the receiver function results, however, GF s from a thicker crust are more complex and detailed analysis is necessary, as multiple interpretations are possible.

A UNRELFS model (Table A1.3) with random velocity variations predicts arrivals at ~ 5.6 s and 9.3s from a 18km deep discontinuity, and the observed data confirm the polarization as P and S (Figure 23, plots F and G). The existence of a Moho discontinuity at ~ 20 km depth was suggested by Frassetto *et al.*, 2011 several km south of ELFS, with an estimated a Vp/Vs ratio of ~ 1.6 . A P-phase reflected on a 50km discontinuity in the RFELFS (Appendix1, Table A1.3) models best the observations when all the waveforms are filtered with CWT gaus5, center period 1.7s and 3.4s, however, the 15s (70° incidence angle in plot G) arrival is not well distinguished on the Fourier filtered waveforms, possibly because of the filter (from 0.2-0.4Hz). The ~ 27 s arrival in plots A-C is explained by RFELFS as S-reflection from a 50 km discontinuity, and has a incidence angle 50° . Another interpretation, which with the current method could not be ruled out, is that the arrivals at ~ 10 s are a mix of P(30km)P and S(18km)S, while a weak arrival at 18s (not marked on the figure, occurring mostly on the horizontal components in plots I-J) is S(30km)S.

As measurements of crustal thickness in the Sierra Nevada rarely agree, additional investigations involving 20-day GF polarization, observations at nearby stations and modeling of all the arrivals would be necessary to make a definitive interpretation of the observed reflections.

Station O05C is a station located in the Sierra Nevada, approximately 160 km northwest of Lake Tahoe, in an area with a high density of faults. Moho thickness is estimated at 41 ± 3.7 km (Appendix 1, Table A1.1) in the Sierra Nevada beneath station O05C by EARS, with Vp/Vs 1.79. Frassetto *et al.*, 2011 estimated a crust ~ 35 km deep beneath this station and a Vp/Vs exceeding 1.8. When using gaus5, the shortest period where the any arrival is visible in the summer months is 2s. The shortest CWT center period where all arrivals are visible on all 20s GF s is 3s (Figure 24A).

This could be explained by heterogeneity beneath the station, with dimensions similar to wavelengths of 6-10 km. Figure 24 shows 20 day GFs at O05C, compared to synthetic waveforms for a source at 1 m depth. Note similarity of the plots D, E and F to plots G, H and I in Figure 23B. Two reflections are proposed to explain the GF arrivals: one at 41 km (V_p/V_s 1.77) and one at 50 km (V_p/V_s 1.78).

Station O08A is located above a 30 km deep low S-velocity anomaly (Figure 2) in a region known as the “heat flow high” of the Basin and Range. The EARS estimated crustal thickness beneath O08A as 32 ± 0.3 km. Klemperer *et al.*, 1986 estimated a P TWTT of ~9.5s in the vicinity of the station. The synthetic waveforms modeled with the RFO08A model (Appendix A1, Table A1.3) correspond best to GF2006360 opposed to GFALL (Figure 25). High levels of cultural noise are contaminating several of the summer GFs. The noise is best removed with wavelet filtering. The arrival identified as PmP at 9s (corrected at 1.7s, see Figure 6) has strong horizontal components (incidence angle ~70 °, Figure 25B) and SmS is identified at 15s (corrected at 1.7s). V_p/V_s is 1.66, similar to the EARS 1.65 value.

4.3. Task 3. Apply the method developed at Task 2 to stations in the SIMPLE and COMPLEX regions in central USA. Interpret the autocorrelation stacks in terms of reflection GF phase composition, crustal structure, crust-mantle boundary depth, and crustal reflector properties. Compare the results to other seismic velocity models at selected stations and to receiver function estimates beneath each station. Interpret the results in terms of resolution and transportability.

4.3.1 Process ambient seismic noise at selected sensors in the SIMPLE area and extract autocorrelation stacks.

Using the method described at 3.2.1, autocorrelation stacks were extracted at stations in the SIMPLE area and are shown in Figure 26. Schulte-Pelkum and Mahan, 2014, found no significant dipping interfaces and anisotropy, and no significant Moho velocity in the SIMPLE area.

GFs extracted at stations in the SIMPLE area are shown in Figure 26 for CWT db4, db5, gaus5 and Fourier filters and compared to the EARS-estimated Moho depth. Note that the center period is 3.4s, which was empirically found suitable for deeper crust. As seen in all plots, the stations to the south of this area are located in a region with relatively uniform Moho. Stations to the north and northeast located at the transition to the thick crust of the Colorado Plateau show clear variations of the GFs and a clear difference between the “simple” crust and the increasing thickness crust (black rectangles). Unlike the Z and E-components, the N component appears to show continuous variation as the depth increases from 44 to 55km. There is a visible difference between the “simple” crust and the increasing thickness crust. A slight P-TWTT reduction is observed as the crust thins to 40km (visible on panels filtered with CWT, using db4 and db5).

Station N27A The Moho depth beneath N27A is 51 ± 6.3 km, with V_p/V_s 1.76 ± 0.13 , according to EARS receiver function results. Only a receiver function-derived model (RFN27A in Table A1.3) was used to generate synthetic waveforms. The observed PmP and SmS are identified as reflections from a 50 km discontinuity, which is similar however, not exactly as predicted by the model RFN27A (Appendix 1, Table A1.3). In Figure 27 PmP arrives at 18.2s (corrected time, see Figure 6) and SmS is identified at 30.75s (corrected time) with V_p/V_s 1.69. Another possible P-arrival is

identified at 13.2s on the vertical component (plot C), with a corresponding S-reflection at 22.75 (Vp/Vs 1.72). PmP and SmS are vertically polarized in this case (plots D-G).

Station N29A The Moho depth beneath N29A is 34 ± 7.5 km, with Vp/Vs 1.7 ± 0.14 , according to EARS receiver function results. Only a receiver function-derived model (RFN29A) was used to generate synthetic waveforms (Figure 28). The PmP (green line, at 12.5s) arrival is less clear in plot C than in plot J, and has a significant horizontal component (incidence angle $\sim60^\circ$). SmS (magenta line, at 22s, incidence angle 80°) is observed here, and Vp/Vs is 1.76. The model RFN29A shows too slow of P and S velocities. Like at other stations in the SIMPLE area, here we observe slightly better directional separation of the PmP (mostly on the vertical component) and SmS (mostly on the horizontal component).

Station W29A The Moho depth beneath W29A is 40 ± 6 km, with Vp/Vs 1.95 ± 0.11 , according to EARS receiver function results.. In Figure 29 it is found that the EARS Moho depth was correct and that PmP and SmS separate on the expected components at longer periods (longer than 2.5s).

4.3.2 Process ambient seismic noise at selected sensors in the COMPLEX area and extract autocorrelation stacks.

GFs extracted at stations in the COMPLEX area are shown in Figure 30. Note that the TWTTs were not picked because the arrivals must be first identified at each station. Differences are observed for the increasing thickness crust (>40 km). Unlike the case of the SIMPLE area, deeper crustal reflectors are not easily distinguishable. One explanation could be that the EARS depth estimations are less precise in this region, thus, each station should be analyzed separately. Shear velocity Vsv models were published by Shen et al., 2013 for six stations in the COMPLEX area. Three stations with well-resolved models (Appendix 1, Figure A1.1) were chosen for discussion here.

According to Shen et al. 2013, **station SPMN and station L37A** are located over Moho at a depth of 50km, however, Moho does not have a large velocity contrast at 50km below SPMN. As estimated by Shen et al. in Appendix 1, Figure A1.1 SPMN has constant gradient velocity up to 50km (Moho) with a change at 35km. L37A has constant Vsv gradient up to ~25 km and Moho at 50km. The Moho depth beneath L37A is 46 ± 3.7 km, with Vp/Vs 1.75 ± 0.07 , according to EARS receiver function results. Appendix 1, Table A1.3 and Figure A1.1 shows the model used at to create synthetic waveforms at L37A (UNRL27A). The Moho depth beneath SPMN is 55 ± 0.3 km, with Vp/Vs 1.67 ± 0.01 , according to EARS receiver function results. Figure 31 shows 20-day GFs at these two stations and a filter comparison. At SPMN an arrival at ~16.75 s (corrected) is interpreted as PmP, however, it has a significant shear component (90° incidence angle), and arrivals at ~27.75 s ($\sim45^\circ$ incidence angle) are interpreted as SmS (Vp/Vs is 1.66). Also, an arrival is observed at ~10.75 s, which is possibly a P-reflection from a compositional discontinuity at ~35 km, with a corresponding SmS at 21.75s and Vp/Vs of 1.66. At L37A (plots H-N) and plots R-T weak PmP reflections, with 15° incidence angle, are identified at 17.2s (corrected), with corresponding SmS (incidence angle 45°) at 28s (corrected), and Vp/Vs 1.6. The Fourier filtered panels show arrivals which are less clear than CWT filtered data at both stations. The RFSPMN

model predicts the observed arrivals, however, the Vs of the RFL37A model is slower than observed.

Station P37A is another example of a station with a deep Moho. The Moho depth beneath P37A is 43 ± 0.2 km, with $Vp/Vs = 1.75 \pm 0.02$, according to EARS receiver function results. Appendix 1, Table A1.3 and Figure A1.1 shows the model at P37A (UNRP37A), extracted by Shen et al., 2013. The Shen et al. 2013 model for this station has an upper crust with velocity increasing uniformly and a ~ 44 km Moho depth, which corresponds to the observed arrivals for this station. Figure 32 shows qualitative correspondence of observed and synthetic waveforms estimated using the Shen et al. model and a Vp/Vs of 1.64.

5. CONCLUSIONS

A new application of seismic interferometry was developed and tested, consisting of extraction of the reflection component of Green's Functions (*GFs*) from ambient noise and signal autocorrelation stacks, to solve for crust and mantle reflector properties. Technique optimization (filtering, arrival identification, polarization) was discussed. The method was applied in three areas of western USA, for a variety of crust-mantle boundary depths and types of transition. The investigation includes comparison of observed and synthetic waveforms, estimated using receiver function and available seismic velocity models.

Method application recommendations

The effect of seismic noise seasonal changes significantly affects the *GFs*. Changes in noise direction, and frequency content are observed as regular patterns in 10 or 20 day *GF* representations and may significantly affect the *GF* stacks. Additional investigations, using synthetic waveforms and polarization analysis are recommended to estimate the best period for *GF* estimation.

The use of polarization analysis as an arrival identification tool needs to be further assessed, applied to 10 and 20 day stacks, and also using *GF* cross-terms at each station. Wavelet filtering was preferred to Fourier filters, however, it is recommended that the results are always compared, and calibrated, as wavelet filters introduce arrival delays when compared to Fourier filters. In regions with highly variable Moho depth, it is recommended that multiple frequency bands are used to identify deeper Moho locations. Pre-filtering may reveal Moho complexity, however, *PmP* and *SmS* are harder to identify when using the pre-filtering option.

Improved frequency content is desirable for increased reflection *GF* resolution. In this study of deep crustal reflections, the waveforms are decimated to 20sps, as a tradeoff exists between larger computation time, limited memory resources and the resolution gain of a 10 Hz Nyquist frequency versus a 20 Hz Nyquist frequency.

Additional investigations are suggested, to assess findings that one day of significant teleseismic activity, with high levels of scattered energy in the crust, is as valuable as two years of data. This

finding may be useful specifically in regions with complex crustal structure, where PmP and SmS are weak. Investigations of the usefulness of local and regional earthquake sequences is also suggested.

Waveforms over time periods as short as 6 months converge to two- year reflection GF when overlapping windows are used.

Arrival identification, specifically in complex crustal environment was a challenge in this study, addressed with:

- a) Multiple station regional analysis, using the representation of GFs from a larger aperture array;
- b) Single station analysis, using 1) 10-day or 20-day GF sections; 2) Polarity of the 10-day or 20-day GF sections; F-statistic indicators estimated for all available intervals.
- c) Polarity analysis of GFs extracted from one-two years of autocorrelation beams;
- d) Comparison to theoretically predicted PmP and SmS travel times, using independent observations of the velocity model beneath each station, extracted from tomographic and receiver function studies;
- e) Comparison to synthetic waveforms estimated using publicly available models in the area.

Synthetic waveform analysis Based on the synthetic waveform investigations, “double arrivals” observed by Klemperer *et al.*, 1986 in the TEST area could possibly be explained by reflections from a strong reflector at ~ 25 km in the crust, or, less probably, by topography of crustal layers, which could have effects similar to localized, randomly triggered circular sources. When random models are added to the deterministic models, the energy is redistributed from the vertical reflection GF to the horizontal components, however, the amplitude of the horizontal reflections is lower. P to S or S to P scattering at the surface may explain observation of PmP and SmS on all components. Waveforms estimated using ambient noise arriving vertically, from sources deeper than the crust, were similar to observations. Because all the investigations in this study were qualitative, additional, in depth synthetic waveform analysis is recommended, using stochastic models with better control on crustal heterogeneities.

Method transportability Post-filtering modifications (change in wavelet and center period, for instance) may be considered when the method is applied in other complex regions. Longer periods were found useful for deeper PmP and SmS identification. In the ideal case of the USArray, changes in GF pattern are observed when the Moho depth (estimated by EARS) varies from 25 to 50 km. A slightly better separation of P and S reflections on the vertical and horizontal components is observed at stations south of the SIMPLE area, which is characterized by low anisotropy. Mid-crustal reflections appear better resolved in regions with deeper crust, if the interpretations in this study are correct.

Error discussion Arrival identification and picking remains the most difficult issue, which needs to be addressed by using multiple sources of geophysical information in the respective region, nearby station investigations, as well as synthetic waveforms and polarization analysis. Further

research for improved methods of arrival identification is recommended. If the arrivals were identified correctly, it is estimated that the error of the method is $\frac{1}{2}$ of the wavelet center period, or the center period of the Fourier transform interval. This error includes time lag pick variations due to different types of filters. For arrival identification, using any other seismic information than active source reflections at the respective station is also subject of large errors. This observation applies specifically to receiver functions in regions of large crustal variability, of scale comparable to the distance between the P and S-conversion points.

Although this method can be used (at higher sample rate) for very shallow (tens to hundreds of meters) analysis, the structure immediately beneath each station was not resolved here, because the wavelengths of interest are much larger than 1km. In some cases, however, such as basin environment, or layers with significant seismic velocity anomalies, static corrections may be necessary.

The method works well for crust with low anisotropy and high reflectivity, however, corrections through additional investigations are recommended in areas with dipping crustal layers or unreflective Moho.

Table 1. Study areas also shown in Figure 1.

Name	Latitude (deg)	Longitude (deg)	Comment
SIMPLE	31.97 to 40.82	-104.82 to -100.63	Moho depth from 31 to 50 km
TEST	39 to 40	-120 to -114	Moho depth from 25-35 km
COMPLEX	37.57 to 48.94	-100 to -90	Moho depth from 25km – 50 km

Table 2. Seismic velocity models publicly available in the study areas, resolution, analysis methods and references.

Study area	Location	Vp	Vs	Resolution	Authors	Method	Comment
TEST	USA 112W to 120W, 40 N	Y	N	50- 100m vertic al	Klemperer <i>et al.</i> , 1986	TWTT data was used to identify the location of the Moho.	Moho reflections beneath COCORP Nevada lines.
TEST	US west of 100°W longitude	N	Y	0.25° x 0.25°	Shen <i>et al.</i> , 2013	A nonlinear Bayesian Monte Carlo method is used to estimate a distribution of shear wave speed (Vs) models beneath each station by jointly interpreting surface wave dispersion and receiver functions and their uncertainties.	3-D model of shear wave speeds beneath the central and Western US to a depth of 150 km
TEST	US west of 110° longitude	N	Y	0.5° x 0.5°	Moschetti <i>et al.</i> , 2010	Surface wave tomography was used with the inversion of the surface wave dispersion maps for a 3-D Vs model. A Monte Carlo method was used to infer a radially anisotropic Vs model of the crust and uppermost mantle beneath the western United States. The isotropic component of this model was calculated by Voigt averaging, and a comparison was done with the direct inversion for an isotropic model	3-D model of shear wave speeds beneath the Western US to a depth of 250 km.
TEST	US west of 114°W longitude	N	Y	0.5°x 0.5°	Yang <i>et al.</i> , 2008	The set of Rayleigh wave phase speed maps was inverted for a 3-D isotropic shear velocity (Vs) model on a $0.5^\circ \times 0.5^\circ$ geographic grid.	3-D model of shear wave speeds beneath the

Table 2. Seismic velocity models publicly available in the study areas, resolution, analysis methods and references (continued).

						The linearized inversion of the Rayleigh wave phase speed curve for the best fitting V_s model below each grid point was used with a Markov Chain Monte Carlo inversion.	Western US to a depth of 150 km.
All	Lat: 10°-70N° Long: -160.0° – 40.0W°	Y	N	200 km-400 km Gaussian Density Functions	Sigloch <i>et al.</i> , 2008	Cross correlation of all usable broadband waveforms measured in North America, in total 59,800 source-receiver paths generated by 635 earthquakes and recorded at 1118 stations. This was used to form a tomographic model of all of North America.	General tomographic model of North America
TEST	Lat: 41°-42N° Long: -120° – 118W°	Y	Y		Gashawb eza <i>et al.</i> , 2008	Nature of the crust beneath northwest Basin and Range province from teleseismic receiver function data	V_p/V_s ratio to determine Moho depth.
TEST	Lat: 39.6°-40.7N° Long: -119.7° – 116.5W°	Y	N		Catchinn gs <i>et al.</i> , 1992		A relation among geology, tectonics, and velocity structure, western to central Nevada Basin and Range
TEST	Lat: 39°-41N° Long: -121.5° - 116W°	Y	N		Louie <i>et al.</i> , 2004	Pn first arrivals were used to measure the depth of the crustal root of the Sierra Nevada range.	

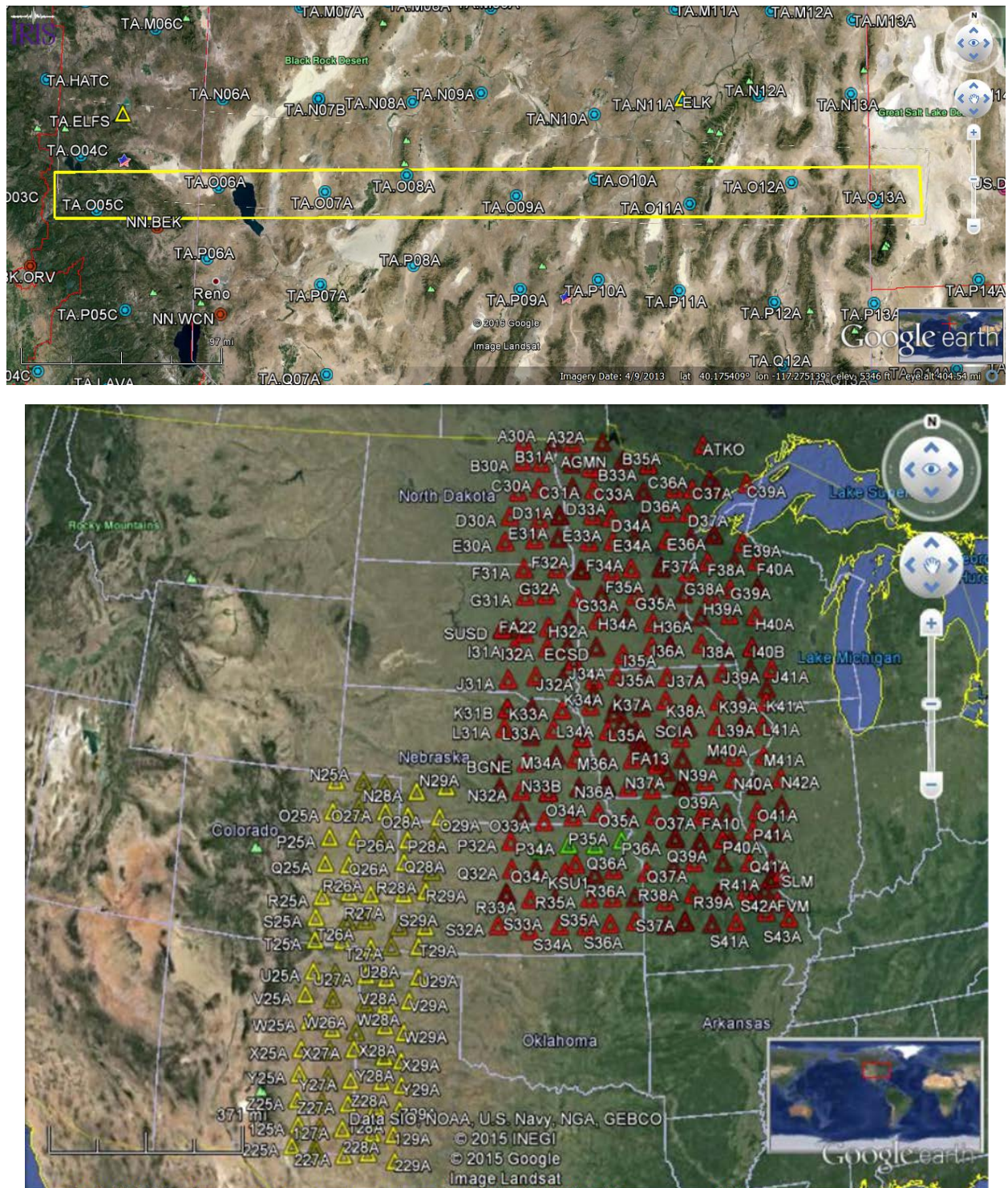


Figure 1. Upper plot: Stations used in this study (see also Appendix 1, Table A1.3) in the area TEST. The lower plots show the SIMPLE (yellow) and COMPLEX (red) study areas. Stations O05C and O[6-13]A are shown as circles in the red rectangle and are located in the vicinity of 40N. Two more stations, shown as yellow triangles, were also used, ELFS and ELK. The location of the stations is within ~50 km the locations of the COCORP experiment (Klemperer et al, 1987).

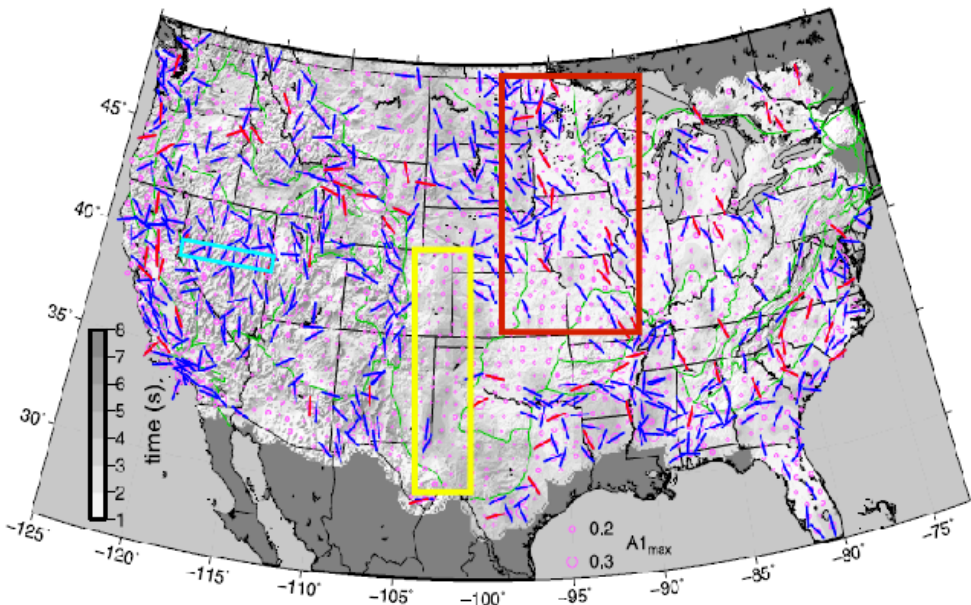


Fig. 9. Map of delay time of largest degree-1 arrival occurring between 1-8 s in greyshade (light – shallower, dark – deep, 1 s corresponding to \sim 8-9 km depth depending on P and S velocity above the converter), overlaid with topographic shading. Pink circles scale with amplitude of the arrival. Red bars are strikes for arrivals exceeding 0.15 I/I_Z ratio that show an opposite phase direct P arrival, indicating an isotropic dipping interface. Blue bars show the same but without a matching direct P arrival, indicating plunging axis anisotropy.

Figure 2. The location of the three study areas in relation to an anisotropy map estimated by Schulte-Pelkum and Mahan, 2014. The yellow rectangle is the SIMPLE study region, the red rectangle is the COMPLEX study region, and the cyan rectangle is the TEST region. The blue lines indicate “plunging axis anisotropy” and the red lines indicate “an anisotropic dipping interface.”

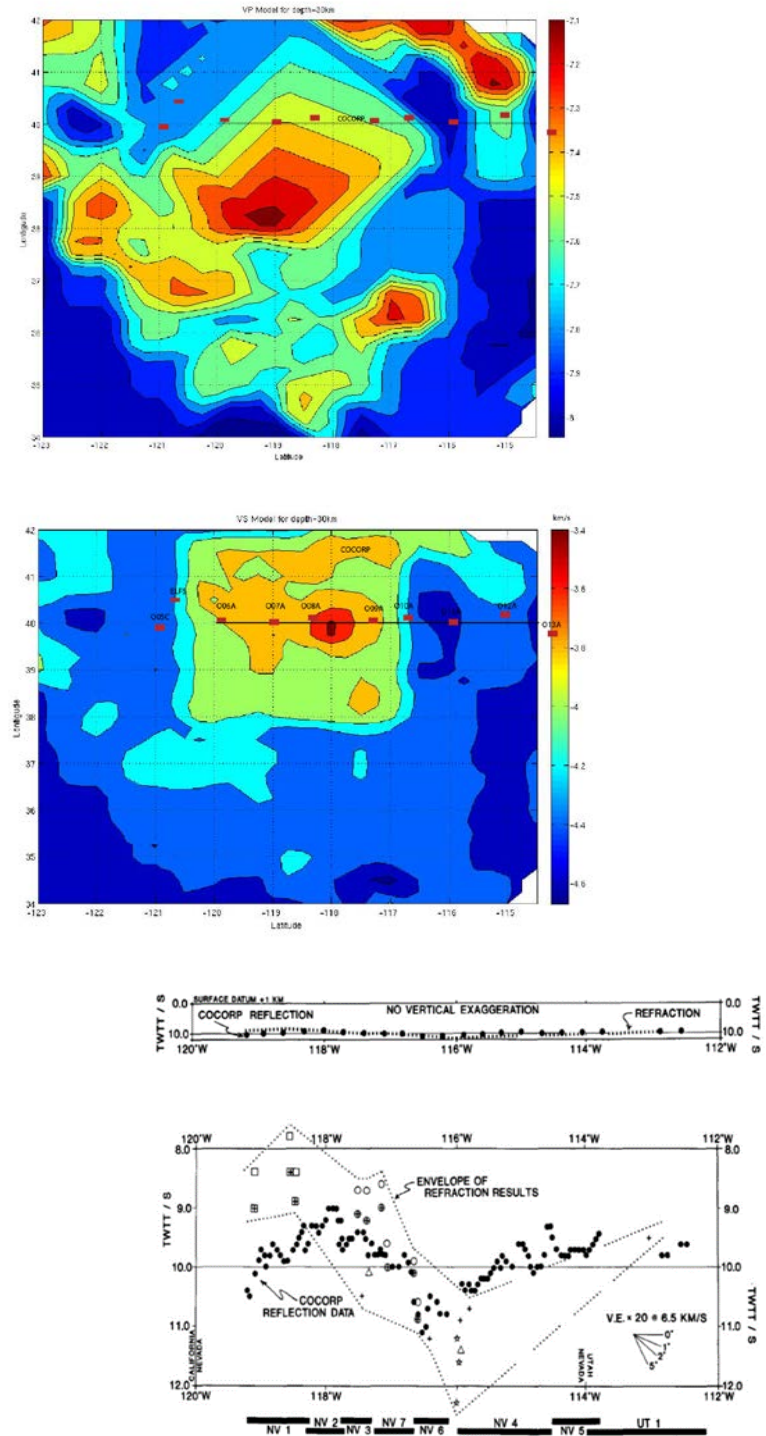


Figure 3. P (upper plot) and S (lower plot) velocity models available at UNR (Tibuleac et al., 2013, in Altarock final report) and the COCORP stations as red filled squares. The COCORP two-way travel time (TWTT) measurements are shown as black dots in the lower plot (Figure 10B from Klempner et al., 1986). Note the correspondence of low S velocity along parallel 40N, interpreted as thin crust, with lowest values of the TWTT-P in Figure 1 (upper plot).

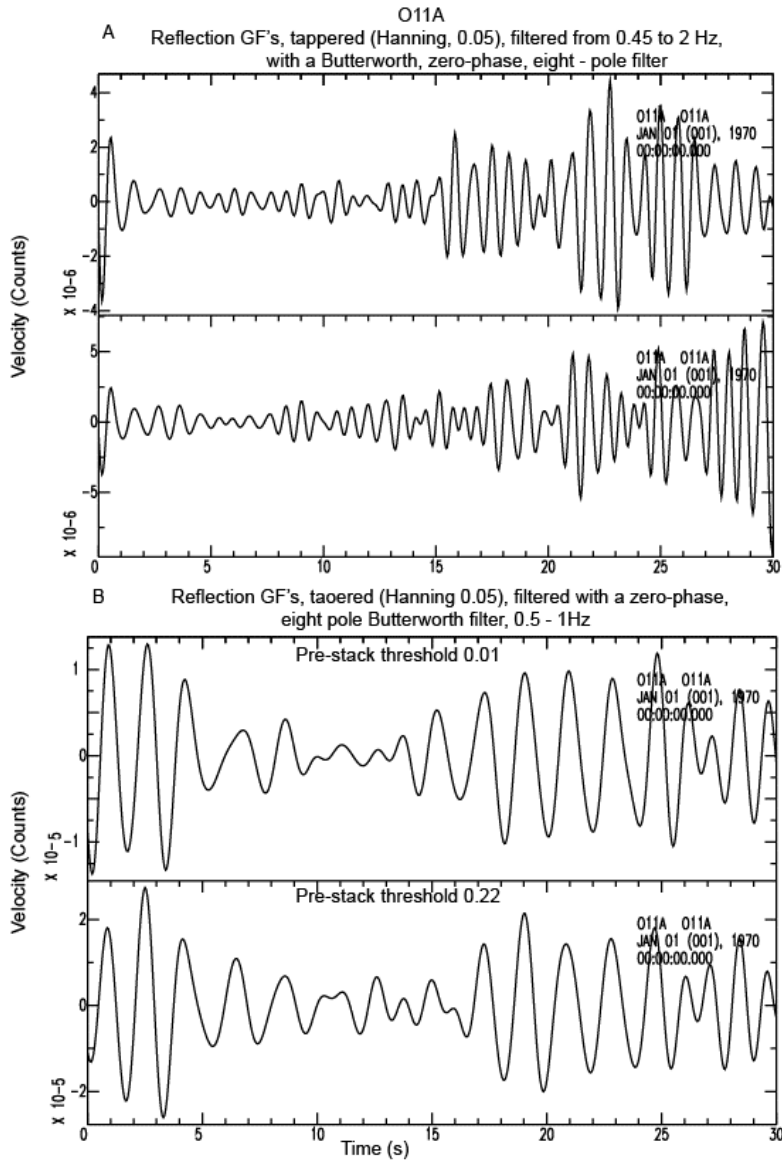
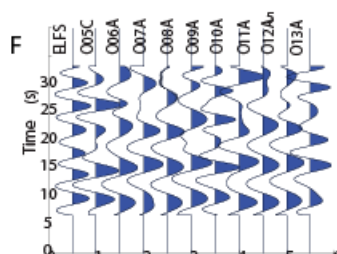
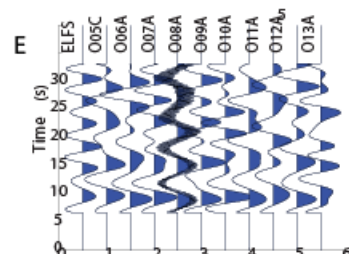
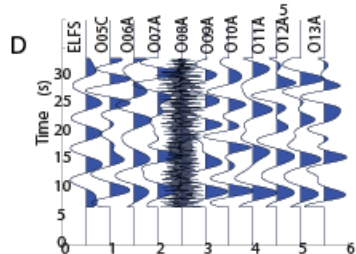
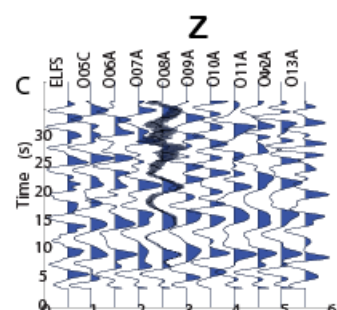
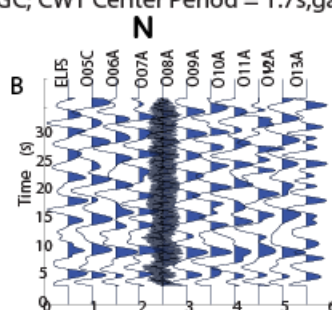
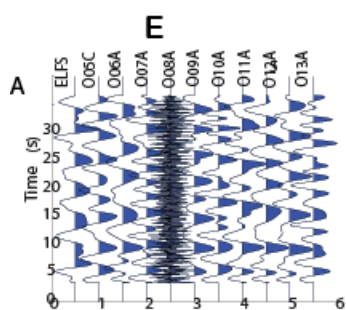


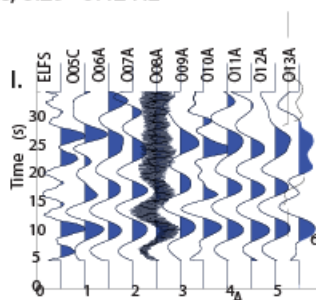
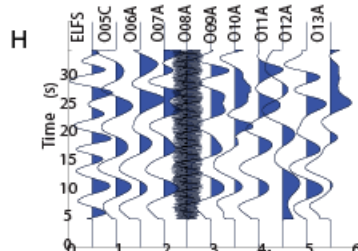
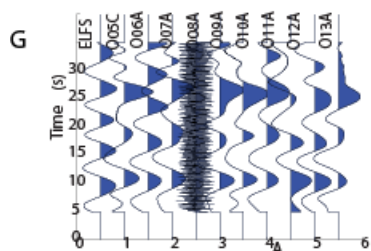
Figure 4. The effect of thresholding prior to GF extraction at station O11A in the TEST region. Prior to stacking, windows from 5s to 19s from the start of daily GFs were filtered (from 0.45 to 2 Hz, zero phase, eight poles) and crosscorrelated. Crosscorrelation maxima are proportional to similarity in the chosen windows. Daily GFs with crosscorrelation maxima greater than 0.01 (upper plot) or 0.22 (lower plot) were subsequently stacked without any filtering. In the lower plot, the only GFs stacked (approximately one third of the waveforms) were those for which all the normalized maximum crosscorrelations values exceeded 0.22 in a window between 5 and 19 seconds. The resulting GF's were filtered as shown in the figure. Note higher amplitude of the signal interpreted as PmP (at nine second time lag) when a higher threshold is applied. B. Higher GF amplitude is also evident at longer periods (0.5 – 1 Hz). Tapers, however, no Automatic Gain Control (AGC) is applied in this figure.

TEST STUDY AREA

8.5s AGC; CWT Center Period = 1.7s,gaus5



10 s AGC; Butterworth Filter, zero-phase-6 poles, 0.29–0.42 Hz



GFs2006 316 2007 359

TEST, Z, 22.5s AGC, CWT period 4.5s

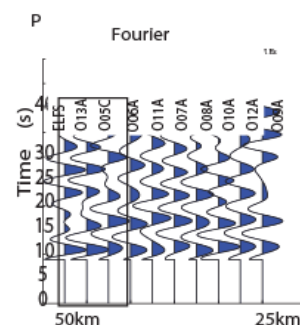
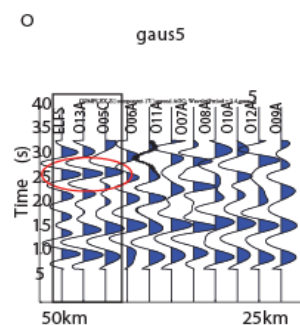
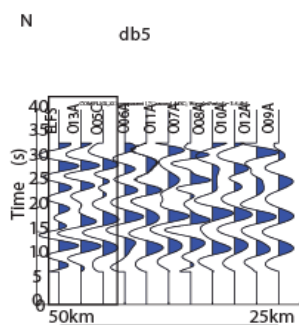
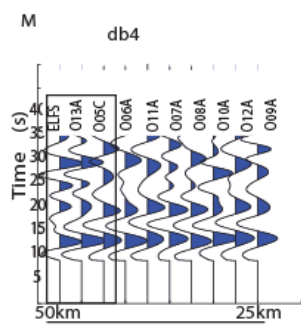


Figure 5. Noise autocorrelations filtered using three different wavelets and one Fourier approach.
Approved for public release; distribution is unlimited.

Plots A-L. Each vertical trace shows the average, from 2006 to 2008, of one-day intervals autocorrelations at a station on the TA line O, and at ELFS, in the vicinity of O05A (Appendix 1, Table A1). Two year autocorrelation stacks in the TEST area are interpreted as the reflection component Green's Functions (GFs). Plots A, D and G are the E-components, plots B, E and H are the N-components and plots C, F and I are the Z-components. The waveforms were converted to records from a broadband sensor with 0.02 Hz corner frequency before autocorrelations, no pre-filter was applied at Step 1 (3.2.1). The GFs are post-filtered using CWT with a “gaus5” wavelet (shown in Figure 6) centered on 1.7s (plots A,B,C), on 3.4s (plots D,E and F) and filtered with a Butterworth, 6 pole, zero phase filter between 0.29 and 0.42 Hz (plots G, H and I). The first large reflection, which we interpret as a Moho reflection at all stations except for ELFS, O05C and O13A, is observed at each station, at ~10 s time lag. The arrival at ~15-16 s is interpreted as the SmS reflection. In this case, the PmP and SmS arrival identification is facilitated by the existence of an array. Automatic gain control (AGC) was applied in a window five times the gaus5 center period on each trace, except for the Fourier filtered traces, for which a window of 10s was used. Note that an additional, strong arrival is present on all three components at ~ 26s when waveforms are Fourier-filtered in a lower frequency band (also observed for CWT, gaus5 at 5s periods). Waveform polarity in this figure is only slightly affected by the AGC application. A possible explanation for the arrival at 26s, if it is interpreted as a two-way travel time from a ~60 km deep discontinuity is the Priestley and Brune (1978) Great Basin of Nevada and western Utah model: “This model consists of a three-layer, 35-km-thick crust and a 29-km-thick, higher-velocity ($V_s = 4.5$ km/s) cap at the top of the mantle, below which lies a broad (180-km-thick) low-velocity zone for shear waves ($V_s = 4.05\text{--}4.12$ km/s). Intermediate-period (15- to 32-s) Rayleigh wave phase velocities measured over shorter paths indicate the existence of significant local variations in the shallow (20- to 30-km-deep) structure which may result from varying crustal thickness or varying depths to a zone of partial melting.” This model was obtained from inverting the dispersion of fundamental mode Rayleigh wave (4- to 120-s period) and Love wave (4- to 40-s period) phase velocities. Priestley and Brune interpret these areas of the Great Basin as a tensional region where deep mantle material has intruded near the surface and created a zone of partial melting. Note GF complexities at ELFS, O05C and O13A. All these stations are located in the vicinity of, or in mountain ranges and are discussed in detail at 4.2.3.1. Cultural noise contaminates the GF at higher frequencies (>0.3 Hz).

Plots M-P show the Z-component at all stations at 4.5Hz CWT center frequency. The stations in each black box have EARS Moho depth of 50km (ELFS), 35km (O05C) and 44km (O13A). All these stations are in mountain range areas surrounding the Basin and Range. All the other stations except for O09A have Moho depth of 30-33km. Note that when filtering with db4 and db5 all the arrivals are delayed. Based on GF similarity, it is estimated that the structure beneath ELFS and O05C is similar at longer wavelengths. All the stations with deep Moho (depth > 45km) have an extra arrival (red circle) in figure O, however they also have arrivals in the vicinity of 10s and 15s (see section 4.2.3.1 for arrival identification). This figure shows why, in order to identify stations above Moho deeper than 35km, is important to analyze a longer time window and to use various filtering wavelengths.

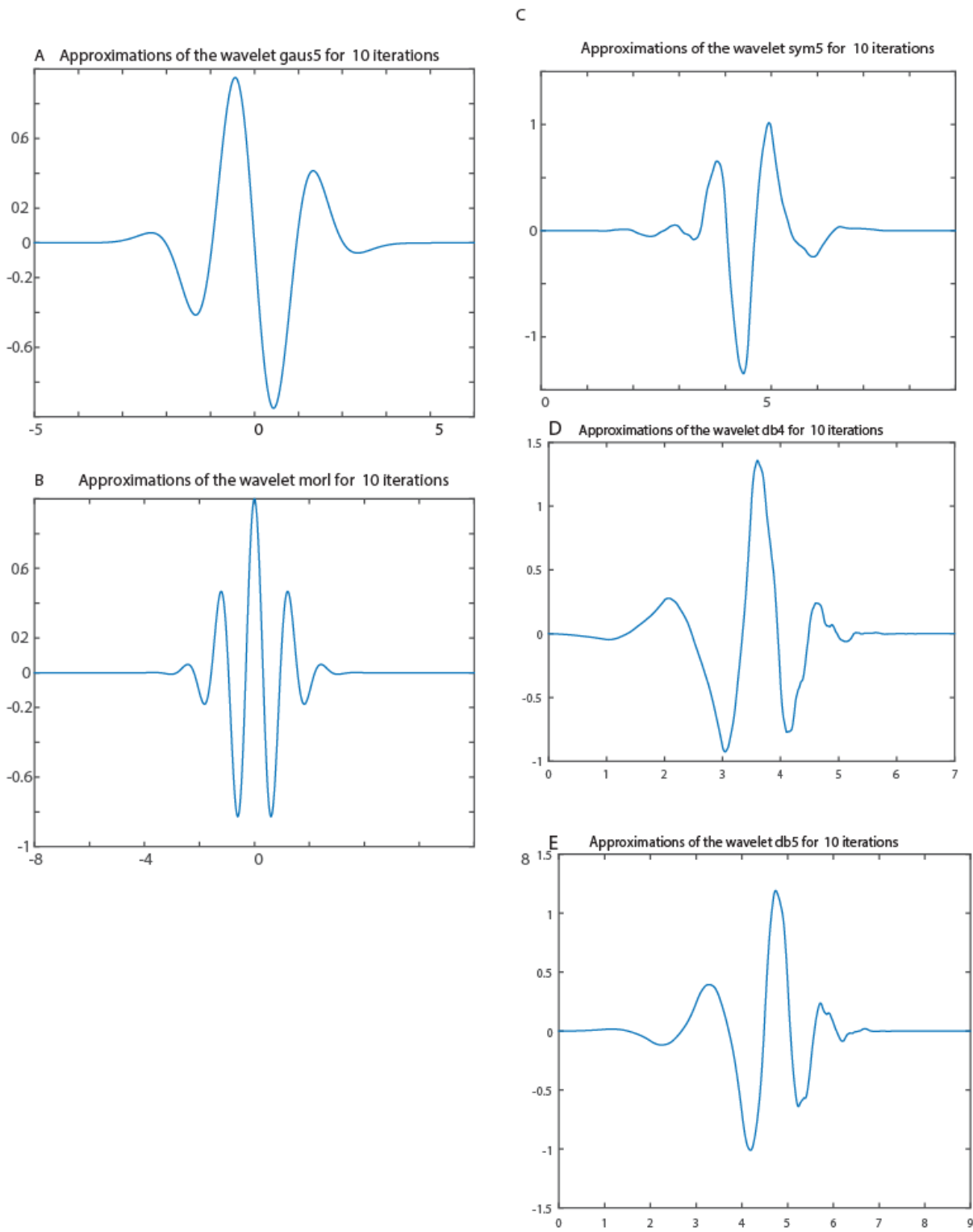


Figure 6A. Wavelets investigated in this study with CWT - gaus5 (A), morl (B), sym5 (C), db4 (D), and db5 (E)

FIGURE 6B

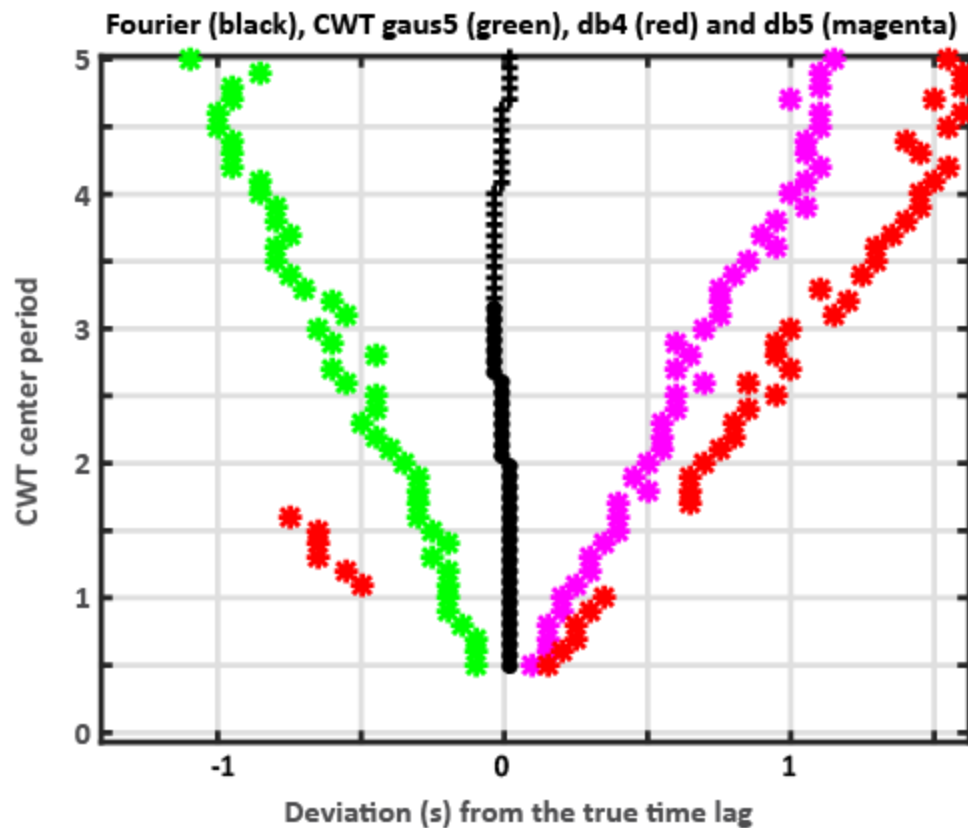


Figure 6B. Biases in arrival time estimates. The best decomposition using CWT occurs when the wavelet shape matches the shape of the signal within the same length of time. B. When a delta function is embedded into a random signal, and filtered with CWT and Fourier filters, the negative maximum peak time lag deviates from the real arrival time differently for each wavelet used. The deviation is larger for longer periods. In contrast, Fourier zero-phase filtered peaks only minimally deviate from the true arrival time for all periods.

FIGURE 7A

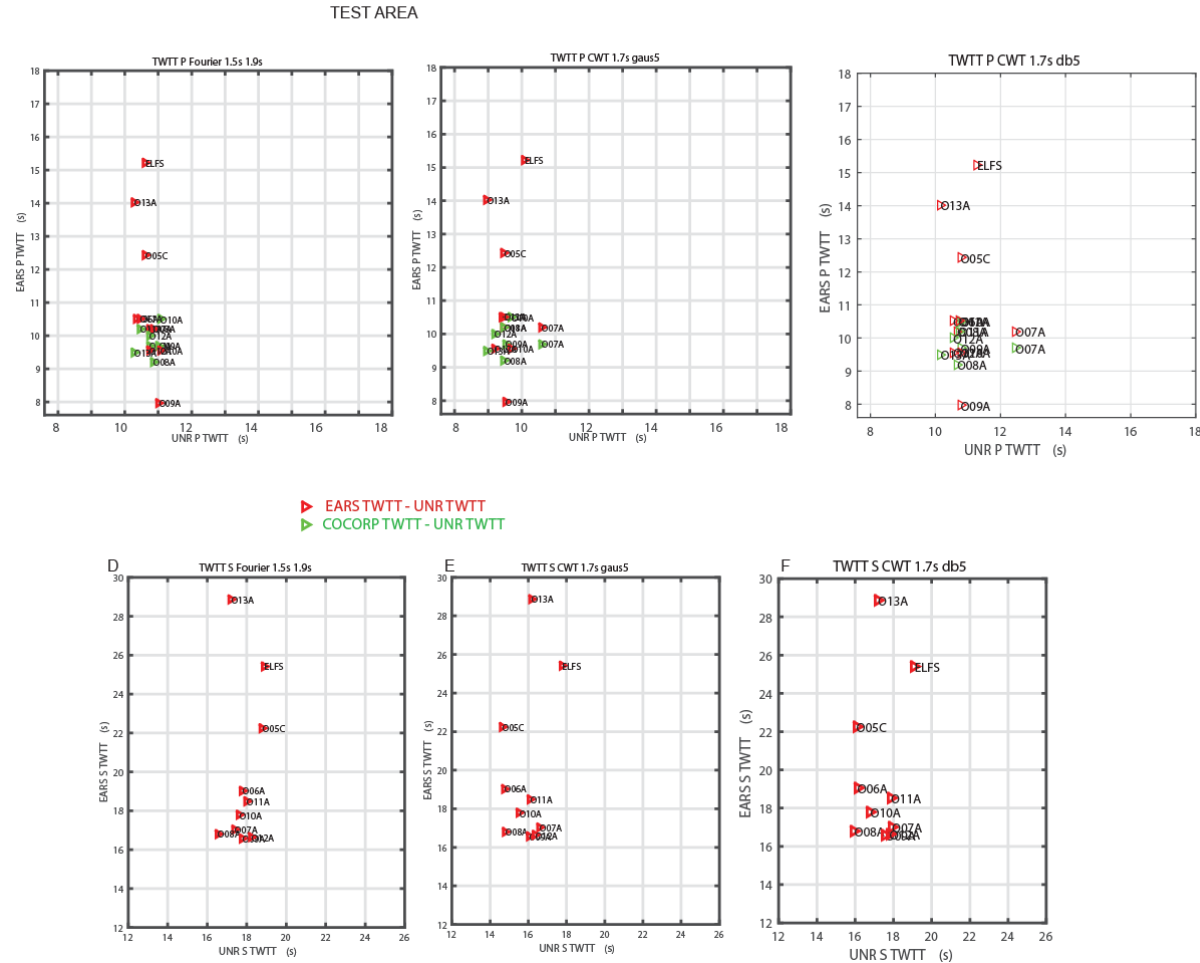


Figure 7. The analyst-estimated two way travel times for PmP (A,B) and SmS (C,D), the COCORP TWTT from Klemperer et al., 1986 (red triangles), and the EARS TWTT estimated from EARS receiver function data (green triangles, only in plots A and B). Note good correlation of COCORP and UNR TWTT. EARS P TWTT correlate slightly better with the UNR TWTT estimated from CWT as opposed to Fourier analysis, and S-TWTT correlates best with the EARS TWTT for Fourier analysis. At stations located in the Sierra Nevada stations ELFS and O05C, at the 'Battle Mountain Heat Flow High' (O09A, plots A and B), and in the eastern Nevada mountain range (O13A), interpretation of the GFs is not trivial, as shown in chapter 4.2.3.1. The TWTT were picked on the Z component.

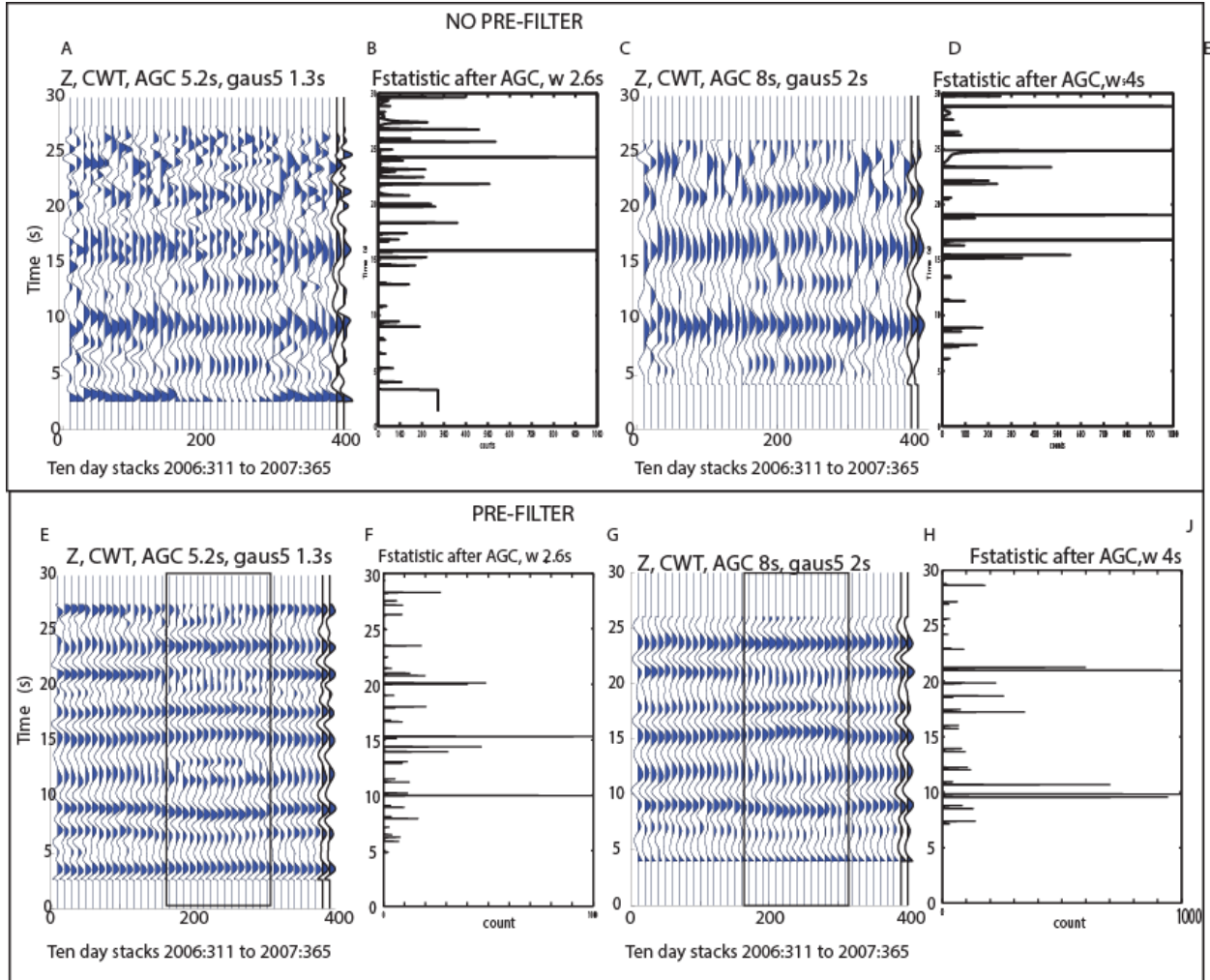


Figure 8. Ten day stacks of GFs extracted at TEST AREA, station O11A when no pre-filtering was applied at Step 1 (section 3.2.1) are shown in plots A-D. Ten day stacks after pre-filtering at Step 1 (section 4.2.1), with 0.3 – 4 Hz high-pass, Butterworth, zero phase, eight-pole filter are shown in plots E-H. The waveforms were post-filtered using CWT, with wavelet gaus5 centered on 1.3s (plots A and E) and 2s (plots C and G). The right two traces in plots A, C, E and G are respectively the GF stack for the whole period (left, named GFALL) and the daily GF for 2006:360 (right, GF2006360). Black rectangles show the summer days, when significant energy is observed in the 0.5-2 Hz range at all stations. Plots B, D, F and H show the F-statistic estimates as a function of time. The window used to estimate the F-statistic was twice the center period, was moved with a step of one sample point, and the value of the F-statistic was assigned to the center of the window. As shown in the synthetic modeling section, the non-linear variations in plots E and G at ~10s time lag, during the summer, are possibly explained by changes in ambient noise direction.

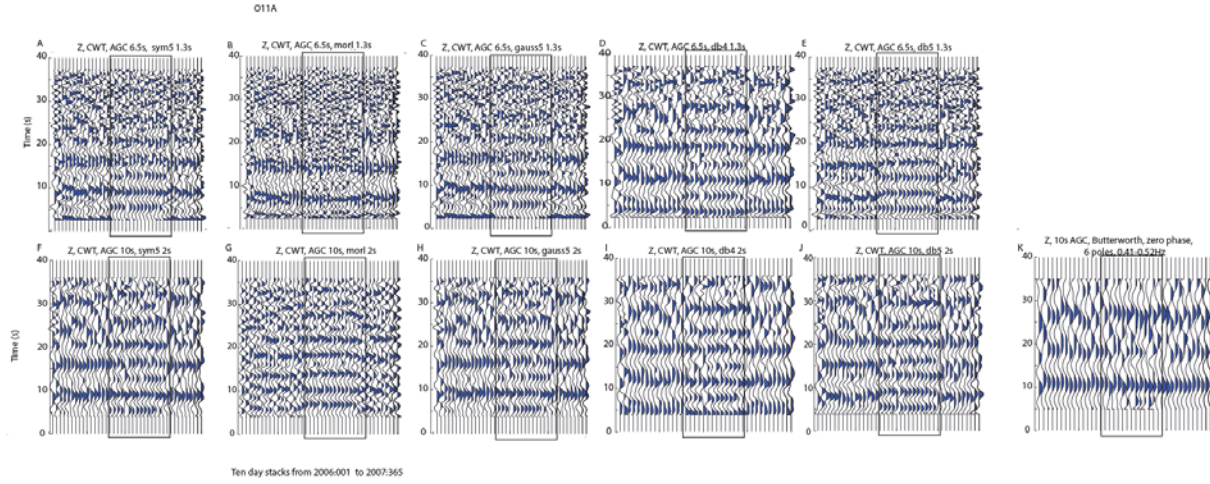


Figure 9. Same as in Figure 8, with a comparison of CWT filters, centered on 1.3s (plots A-E) and 2s (plots F-J) applied on the Z-component at O11A. Plot K shows the zero-phase six pole Fourier filter centered on 2s. Enhanced amplitude is observed when the wavelet shape is similar to the shape of the signal. CWT with sym5 and gaus5 produce similar results after AGC and the morl wavelet picks up more noise, especially in the summer months (black rectangles). CWT with db4 and db5 result in arrivals of opposite sign, and gaus5 and db5 arrivals are most similar to the Fourier filtered waveforms.

O11A

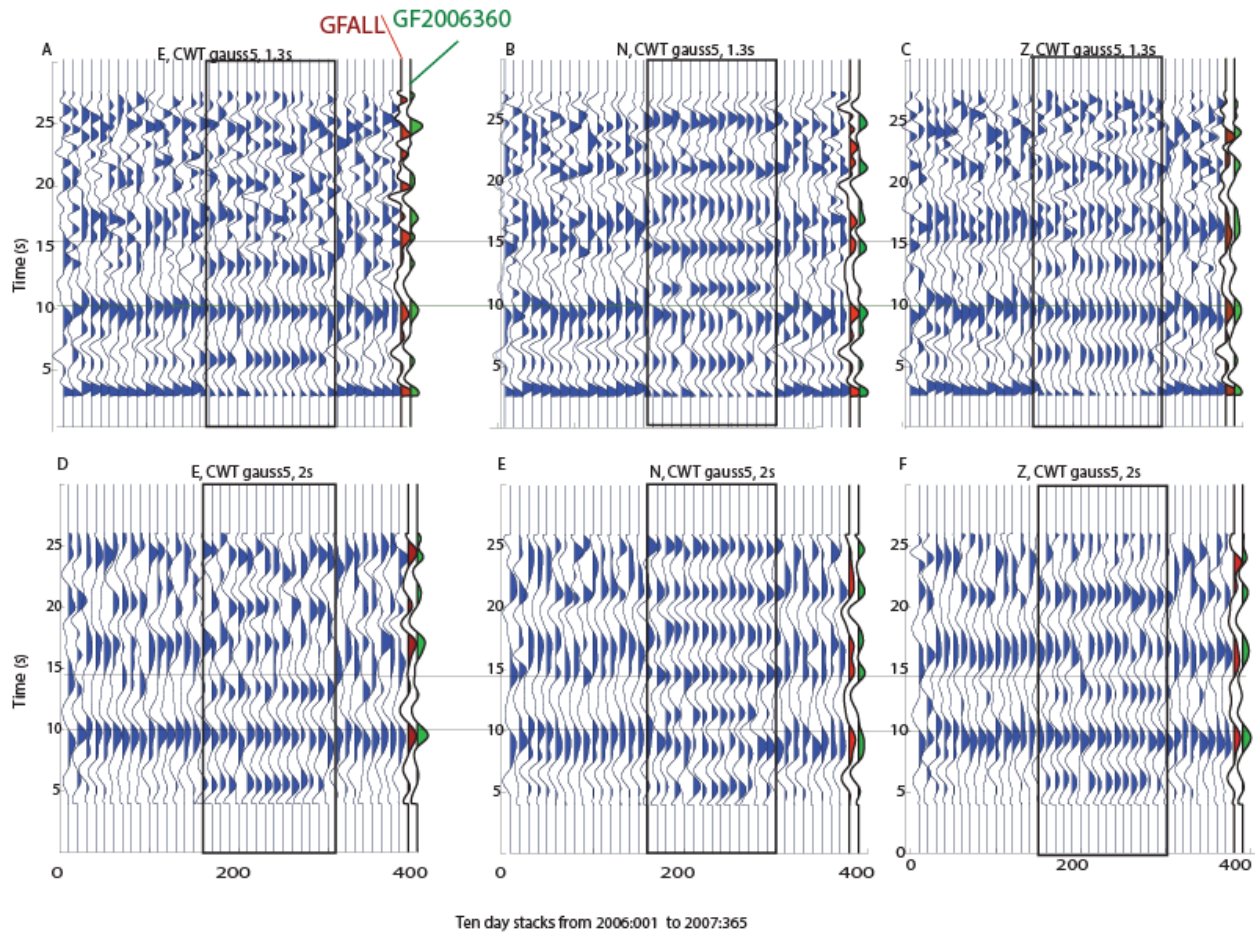


Figure 10. Ten day stacks of GFs extracted at O11A with no pre-filtering, on the E (plots A,D), N (plots B,E) and Z (plots C,F) components. The waveforms were post-filtered using CWT, with wavelet gaus5 centered on 1.3s (plots A-C) and 2 s (plots D-E). AGC with a window four times the center period was applied. The right two traces in all plots are respectively the GF stack for the whole period (red, GFALL) and the daily GF for 2006:360 (green, GF2006360). Black rectangles show the summer days (Julian days 150-250), when significant seismic energy is observed in the 0.5-2 Hz range at all stations. Note different arrival times, when compared to the Z and E components, for the reflections on the N-component. Some of the summer arrivals arriving after 11s on the N component appear to have opposite direction with the Z and E components, thus, the noise may possibly arrive from the northwest-southwest direction in the summer, which is the direction perpendicular to the mountain ranges in Nevada. PmP is strong on all three components, while SmS appears better defined on the Z-component for this station.

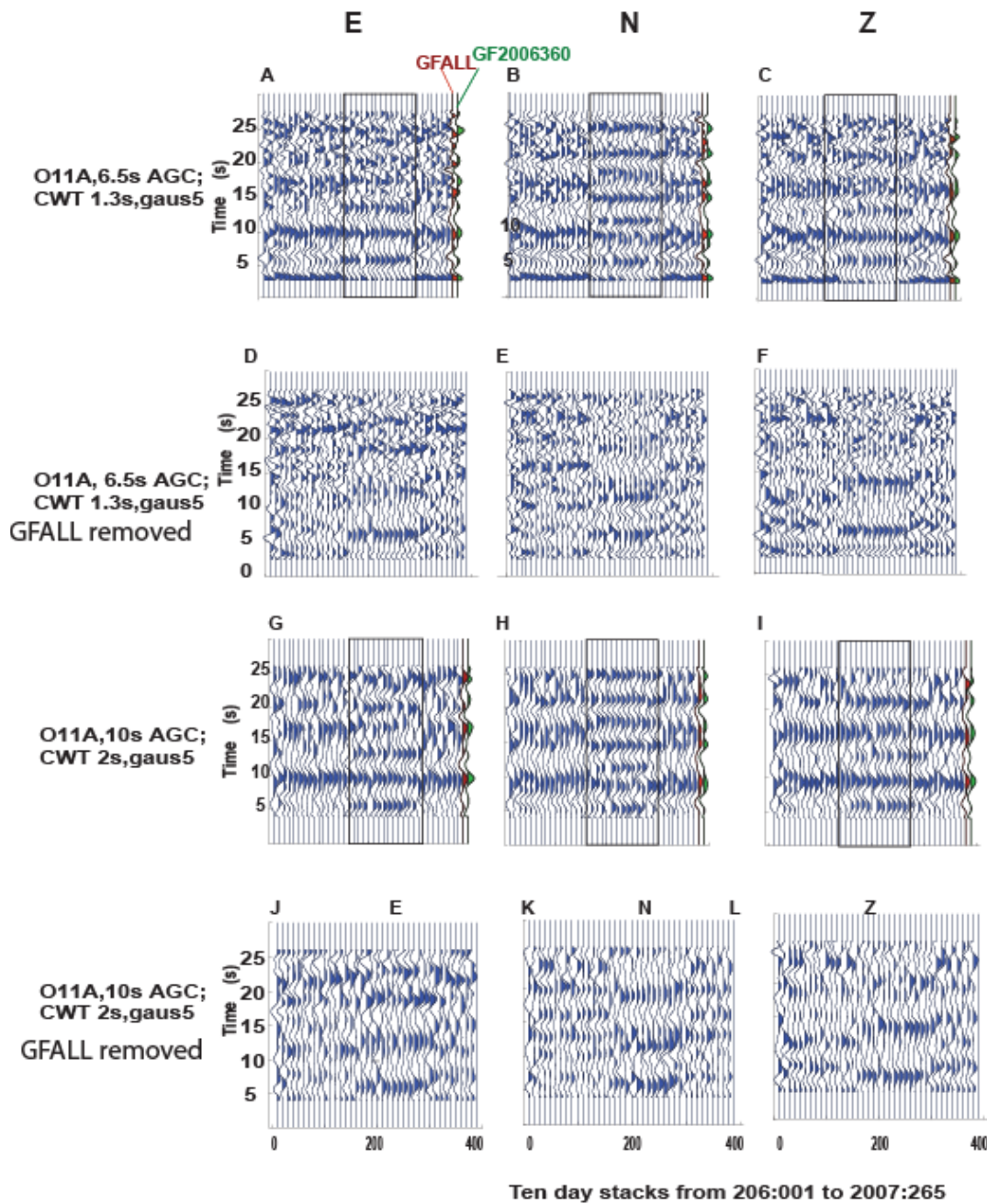


Figure 11. The same plots as in Figure 10 are shown at A-C and G-I. To better isolate seasonal variations at O11A the stack for the whole period, GFALL (the right red trace) was removed from each ten-day stack. The results at two CWT center frequencies are shown in plots D-F (center period 1.3s) and plots J-L (center period 2s). Two reflections are observed during the summer months (black rectangles) at ~ 6.5 s and at ~ 13 s, which could be interpreted as multiple reflections from a mid-crustal layer. In this interpretation is correct, mid-crustal layers are best illuminated by the relatively higher frequency noise observed during the summer months, while deeper layers are illuminated best during the winter months, when longer period noise is dominant.

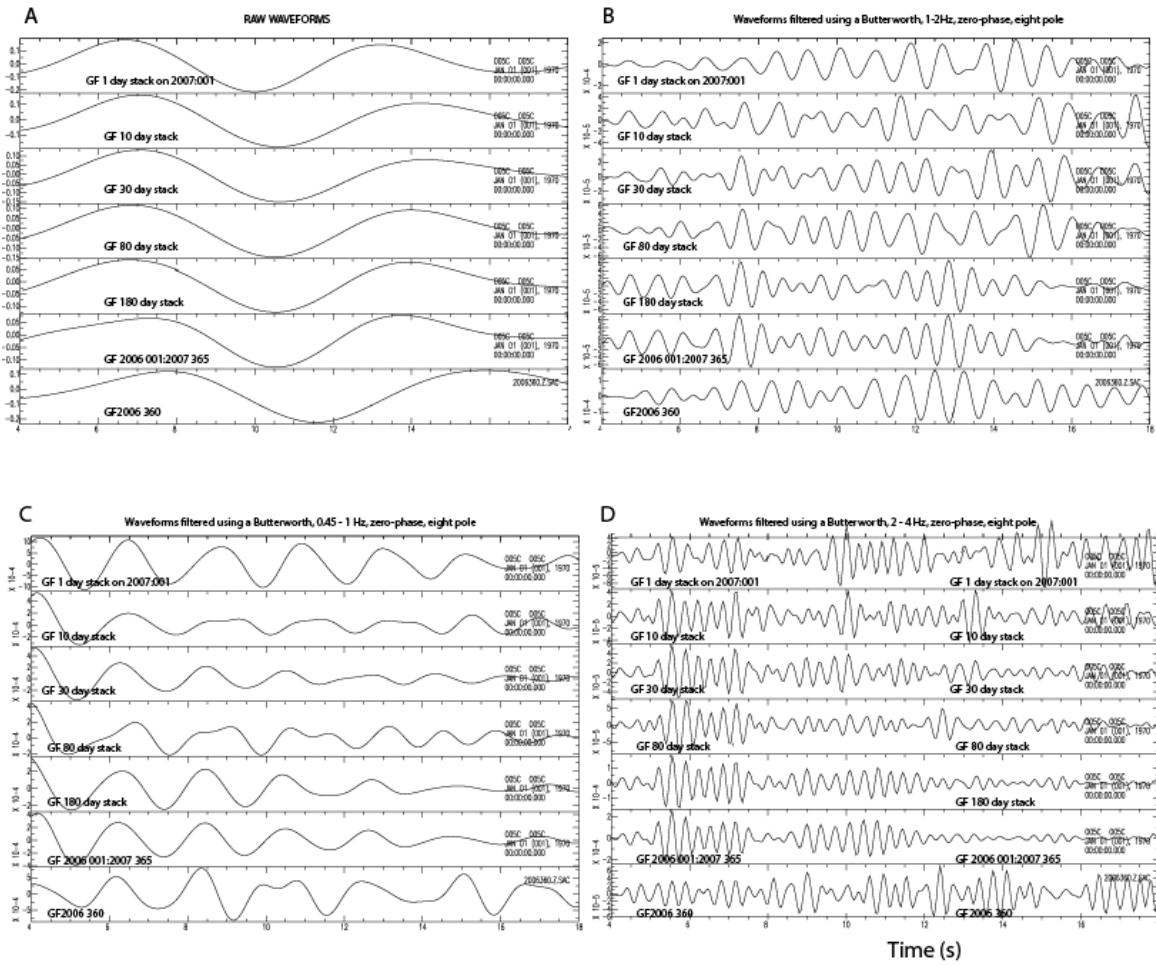


Figure 12. Shows the effect of using one hour, 50% overlap windows to compute autocorrelation stacks. For analysis periods from 1 day (first from the top in all plots), 10 days (second from the top in all plots), 30 days (third from the top in all plots), 80 days (fourth from the top in all plots), and 180 days (fifth from the top in all plots), compared to the 2 year autocorrelation stack at O05A (named GFALL, or GF 2006:001 – 2007:365). GFALL is obtained from stacks of one – day autocorrelations with no overlap and is shown in every sixth subplot from the top in plots A-D. The upper five stacks in each plot start at 2007:001. The upper waveform in each plot is the stack on 2007:001 and the lowermost (seventh) waveform in each plot is the stack of one hour windows in 2006, Julian day 360 (GF2006360). The difference between these two one day stacks is the high teleseismic activity on day 360 of year 2006. In plots A, B and C, the 180 day stack best matches GFALL. Note that the first 5s “arrival” (interpreted as a shallower layer reflection) matches the GFALL after 30 days of stacking. Note best correspondence of the one-day stack in the seventh plot and the GFALL at frequencies lower than 2Hz (plots A,B,C). In plot D, at frequencies greater than 2 Hz, the first “arrivals” (~2.5s) correspond well to the 2 year stack (in the sixth panel) starting with 1 day analysis time. Note that all the comparisons are qualitative. Quantitative analysis is needed to best assess the GF convergence to the GFALL.

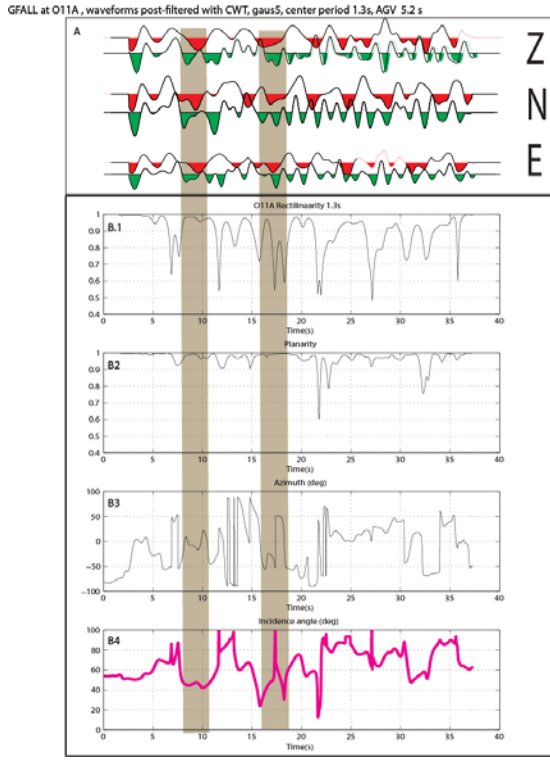


Figure 13. Polarization analysis of the two-year GF's (GFALL, red) at station O11A. GF2006360 (green) is added for comparison in plot A. P-polarization, rectilinearity and P incidence angle in 2.6s windows (2 times the center period, gray areas) are shown plots B1-B4 as a function of time. The parameter values have been attributed to the start of the window, which is moved along the waveform with a step of 1 sample point (waveforms are sampled at 20 sps). The azimuth is measured from the east direction and the incidence angle is measured from the vertical axis which points up, for a wave traveling in the direction of the axis. Incidence angles of 90° are estimated when the particle movement is in a horizontal plane (S-phases). High rectilinearity and planarity are indicators of the arrival of a seismic phase. In this case PmP has an “incidence” angle of ~ 40°. The arrivals at 17.5s have S-polarity (incidence angles ~90°), and 90° shift in backazimuth. One later arrival in a 2.6 s window starting at ~22s has an incidence angle of ~ 15°.

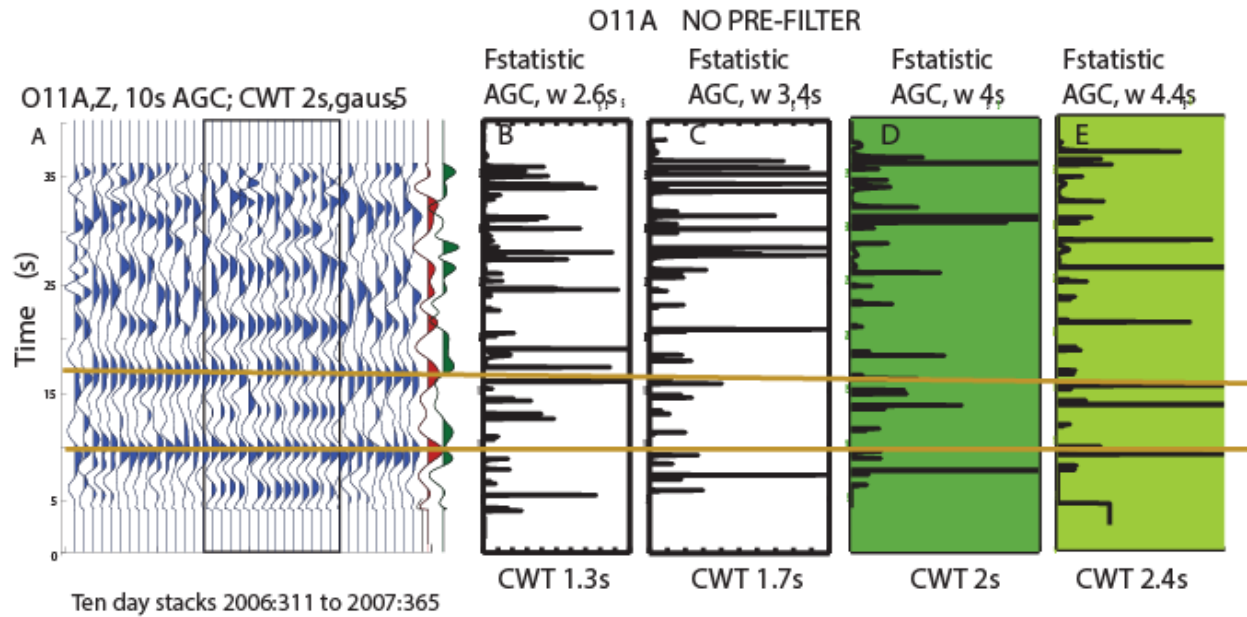


Figure 14. A. PmP (~ 9.7 s) and SmS (~ 16 s) arrivals at station O11A, at a chosen center period of 2s, are identified using CWT and an empirically chosen gaus5 wavelet. Plots B,C,D and E show the F-statistic estimated at center periods 1.3s, 1.7s 2s and 2.4s for windows (W) twice the center period of the wavelet, on normalized waveforms, with a step of one sample point (at 20 sps). Note that the PmP and SmS arrivals correspond to windows with local F-statistic maxima, similarly located in plots D-E, however different from plots B and C, where CWT picks earlier arrivals. The F-statistic value is assigned to the center of the window and is zero if the beam has the same polarity with the autocorrelation maximum.

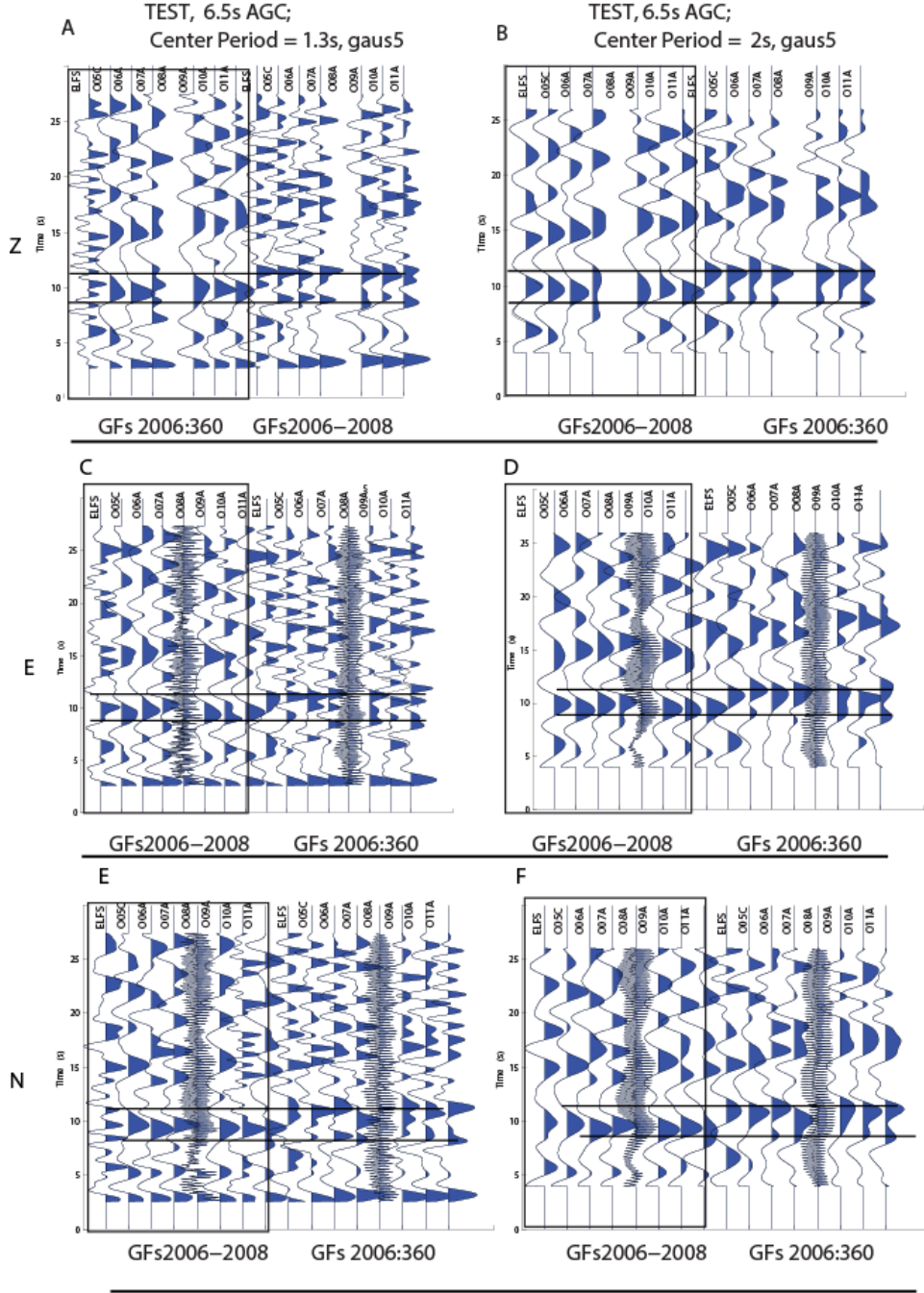


Figure 15. The Z-component GF's (GFBEAM) at stations in the TEST area, using 2 years of data are shown in the black rectangle in all plots. The daily GF's using only one day of high teleseismic energy release at each station (GF2006360), on December 26, 2006 are shown on the right in each plot, for each component: Z (plots A and B), E (plots C and D) and N (plots E and F). The CWT gaus5 center frequency is 1.3s in plots A, C and E and 2 s in plots B, D and F. Note split PmP arrivals and SmS arrivals on the GF2006360s and a significant delay, especially for SmS. A possible explanation of the delay suggested by synthetic waveform modeling is directionality of the seismic energy from a non-vertical angle of incidence.

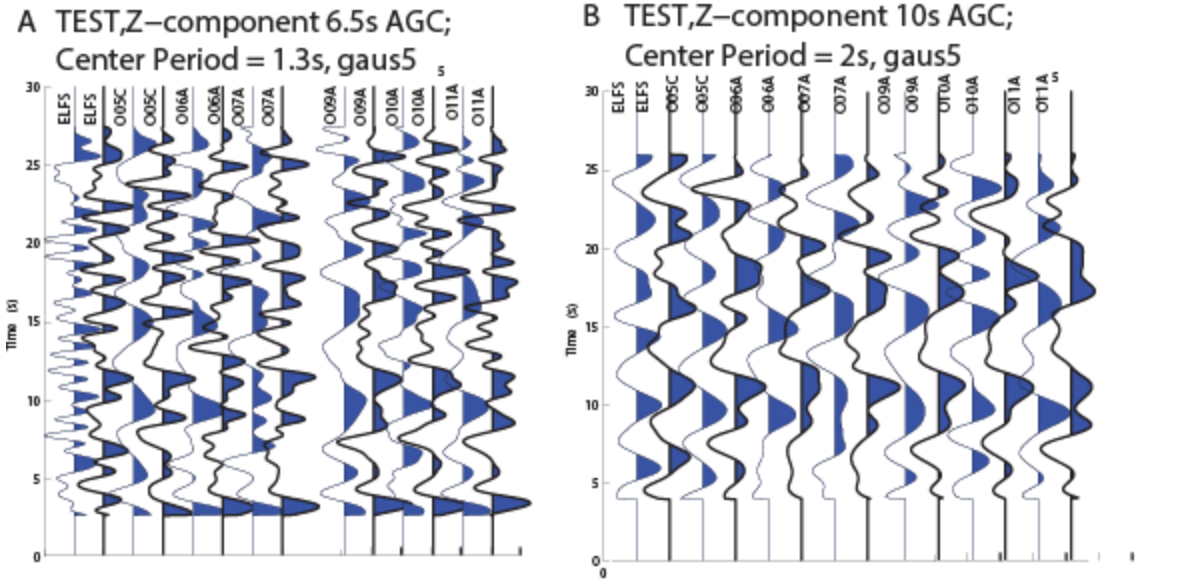


Figure 16. Same as in Figure 15, with staggered GF's, at every station. For each station, the left waveform is the 2-year beam (GFALL), the right (black outline) waveform is the GF2006360 in Figure 15, extracted on Julian day 2006:360 at the same station. Only the Z-component is shown here.

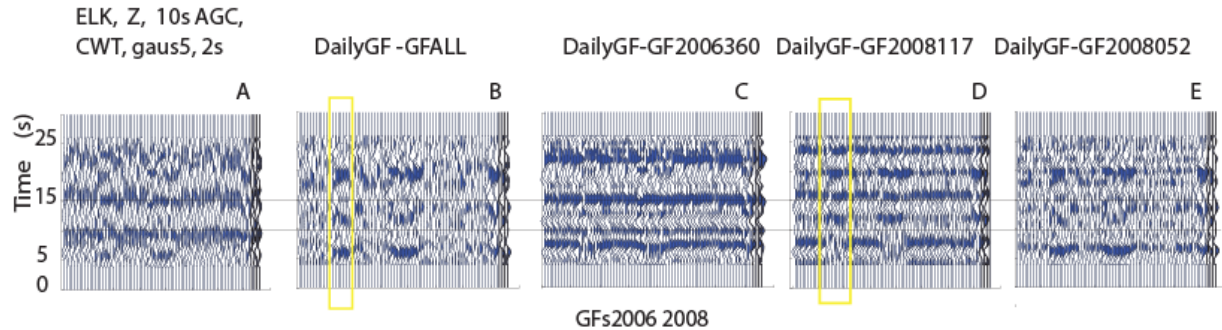


Figure 17. Same as in Figure 11, at station ELK (component Z). However, in this figure, not only the GFALL (plot B) and the GF2006360 (plots C) are removed from each ten-day GF in plot A, also the Mogul (GF2008117, plot D, from more than 500 km epicentral distance) and Wells (GF2008052, plot E, from 55 km epicentral distance) are removed. By removing the GFALL from the 10-day stacks in plot A, daily/seasonal variations are easier to observe (plot B). The yellow rectangles show a summer period at ELK with an upper crustal reflection at ~7s (plot B) which is removed when the GF2008117 is subtracted from the ten-day plots (plot D). As opposed to the teleseismic events and the Wells sequence, the very shallow Mogul sequence appears to contain shallow, high frequency crustal periodicity information. This discussion is valid for all components. Note that removing GFALL and GF2008052 results in similar plots (B and E). As shown in plot C, the GF2006360 has higher frequency content in all the reflections. The Mogul sequence (GF2008117) introduces extra periodicity on Z, and on all components, observed as additional “arrivals” in the difference plots.

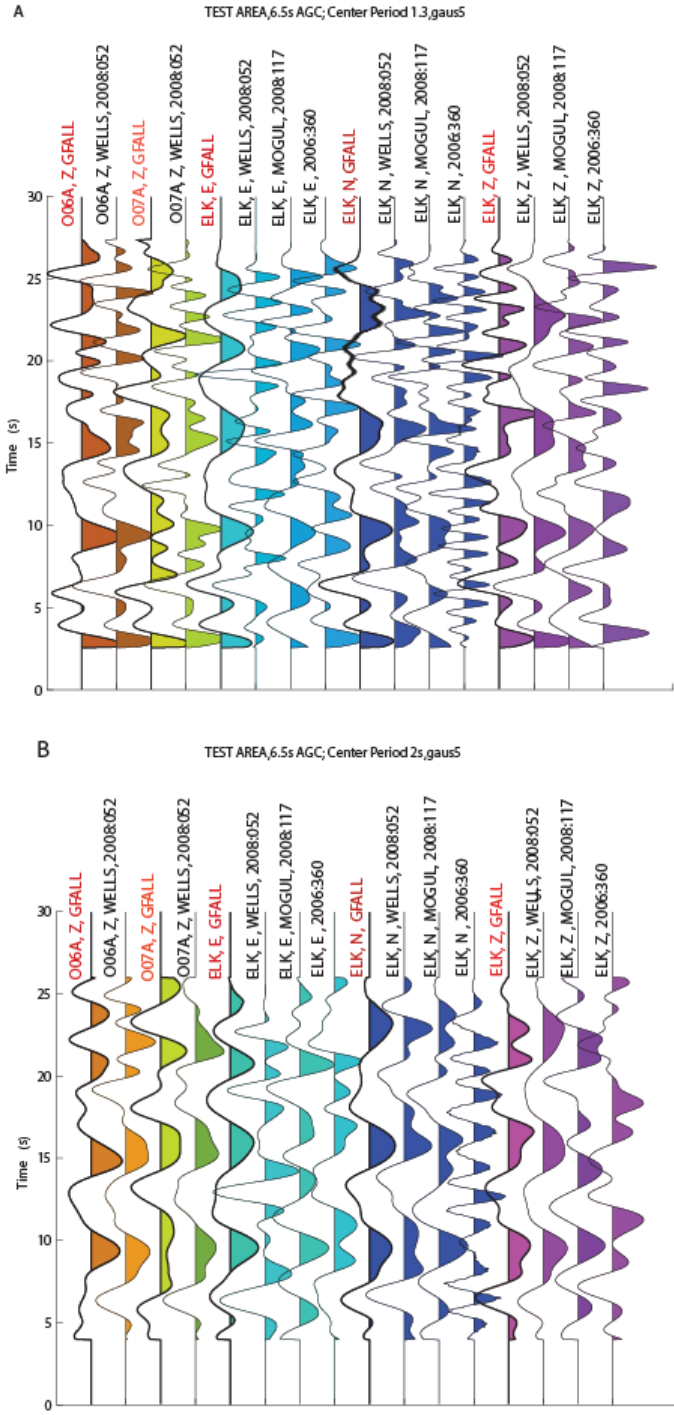


Figure 18. Shows comparison of GF2006360, GF2008052 and GF2008117 with GFALL at stations O06A (brown), O07A (green) and ELK (cyan E, blue N and magenta Z). Waveforms were filtered using CWT, gaus5, centered on 1.3s (plot A) and 2 s (plot B). The Wells earthquake was recorded at all three stations, however, the Mogul earthquake was only recorded at ELK. The Z-component GF is shown at O06A and O07A, and the E,N,Z components are shown at ELK. Note good correspondence of the 2008:052 daily GF's and the GFALLs at O06A and O07A,

possibly due to larger epicentral distance (> 500 km) of the 2008:052 Wells sequence. Also note good correspondence of all daily GFs and the GFALL on the Z-component at ELK, and on the N-component (except for the 2006:360 daily GF, contaminated probably by cultural noise) and worst correspondence of the daily GFs on 2008:052 and 2008:117 on the E component. The shear wave energy from both earthquake sequences in 2008, which was the dominant energy, was oriented roughly along the ELK N-component.

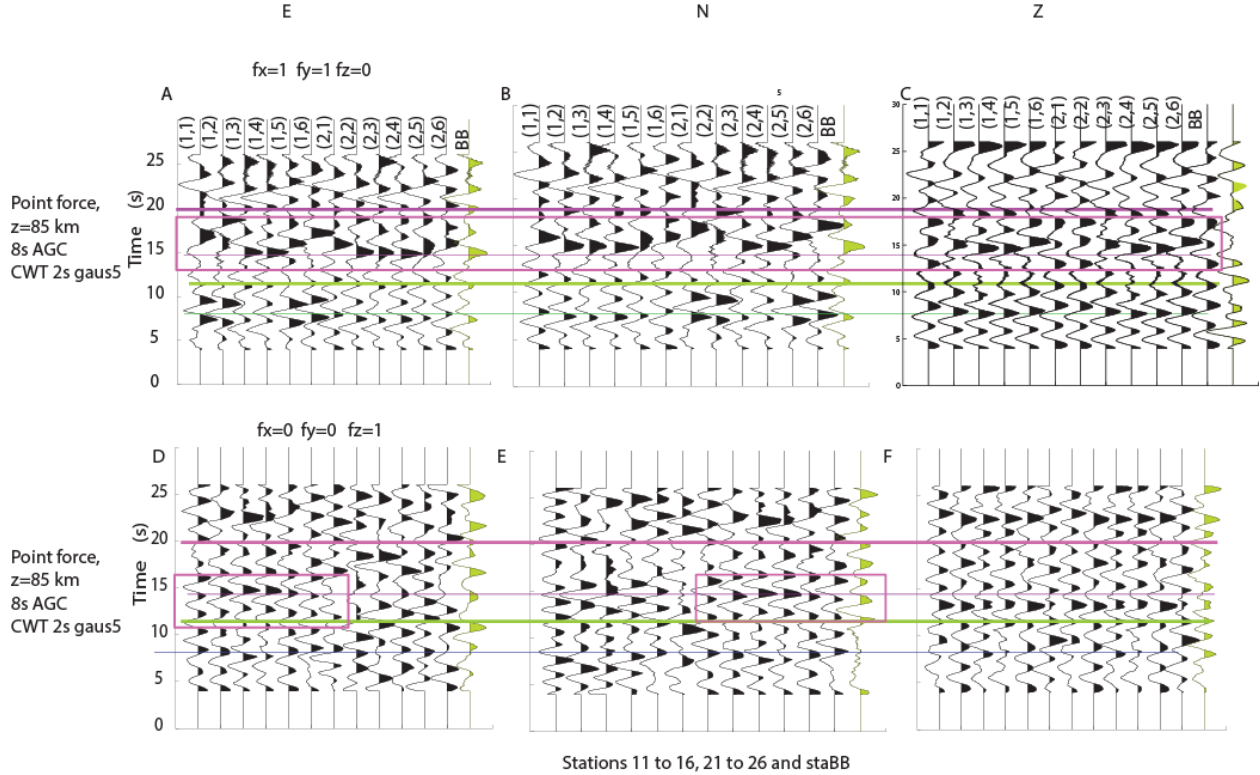


Figure 19. Comparison of three component waveforms simulated using the model M2 in Appendix 1, Table A1.3 for point-force sources with horizontal ($fx=1, fy=1, fz=0$), respectively vertical ($fx,y=0, fz=1$) located at 85 km depth. The synthetic waveforms underwent the same type of processing (sign bit corrections, autocorrelations and AGC) as the observed GFs. The magenta rectangles show S-reflections from a 25 km deep reflector in plots D and E. Thin blue line is the TWTT of the P-reflection from the 25 km discontinuity, the thick green line is the TWTT for the PmP, the thin magenta line is the TWTT for the 25 km discontinuity and the thick magenta line is the SmS TWTT. Note that PmP, and the P-reflection from the 25 km layer are retrieved in plot C, although the source has only horizontal components. In plots A and B, the S-waves reflected on the 25 km discontinuity are retrieved, and show variations as a function of the source-station angle which resemble the seasonal noise patterns observed at some of the stations discussed in this study. When a vertical only source is used, visible arrivals are the P-reflection from the 25 km layer (plot F) and S-reflections from the 25 km layer (plots D and E), however, PmP is not visible.

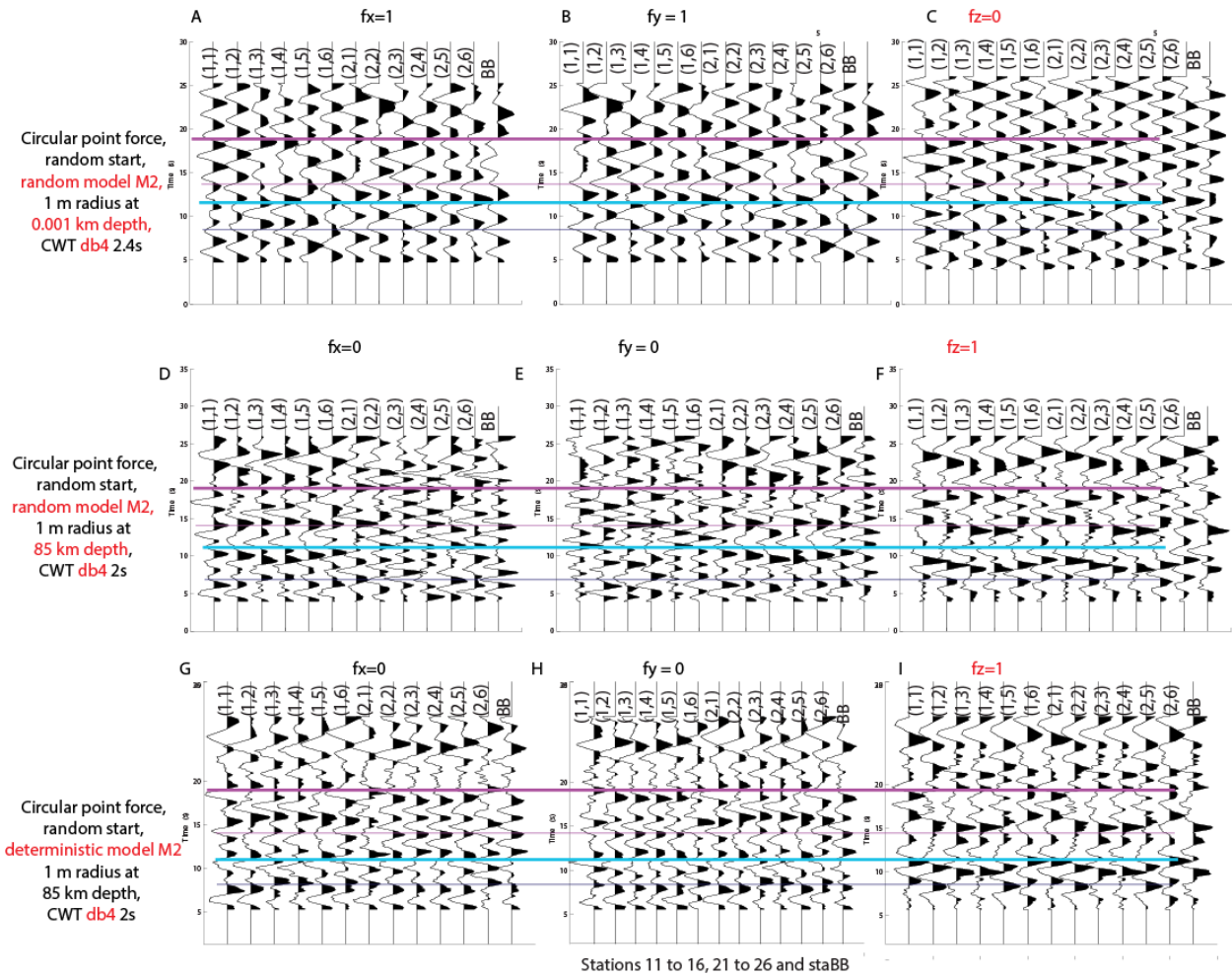


Figure 20. Comparison of three component waveforms simulated using the model M2 in Appendix 1, Table A1.2.1 for point-force sources with random start (within 1 sec), located in a circle of one meter radius beneath the center BB station at 1 m depth (plots A-C) and 85 km depth (plots D-I). Theoretical time lags for P(25km)P (thin blue line), S(25km)S (thin magenta line), PmP (cyan line) and SmS (magenta thick line) are marked with horizontal lines. The synthetic waveforms underwent the same type of processing (sign bit corrections, autocorrelations and AGC) as the observed GFs, if the sources were deeper than 1m. Only CWT filtering and AGC was applied when the source depth was 1m. No clear arrivals are visible in plots A-C. Plots D,E G and H show PmP only on the horizontal, even if the source is vertical. P and S reflected from the 25km discontinuity are identified at times varying with the source-station vertical angle. According to Figure 6B, db4 picks arrivals about 0.6s later at 2s center period. PmP is observed on the horizontal components even if the sources are all vertical (plots D, E, G and H). SmS is observed on the horizontal component in plots D, E, G and H even if the source is only vertical. This effect is less visible in plots D and E, when the medium is random (correlation length 800m, aspect ratio 2:1, amplitude variation $A(z)=0.1$), and invisible when the sources are at the surface (plots A and B). When the sources are at the surface, only the GF recorded by the BB station shows PmP and SmS arrivals.

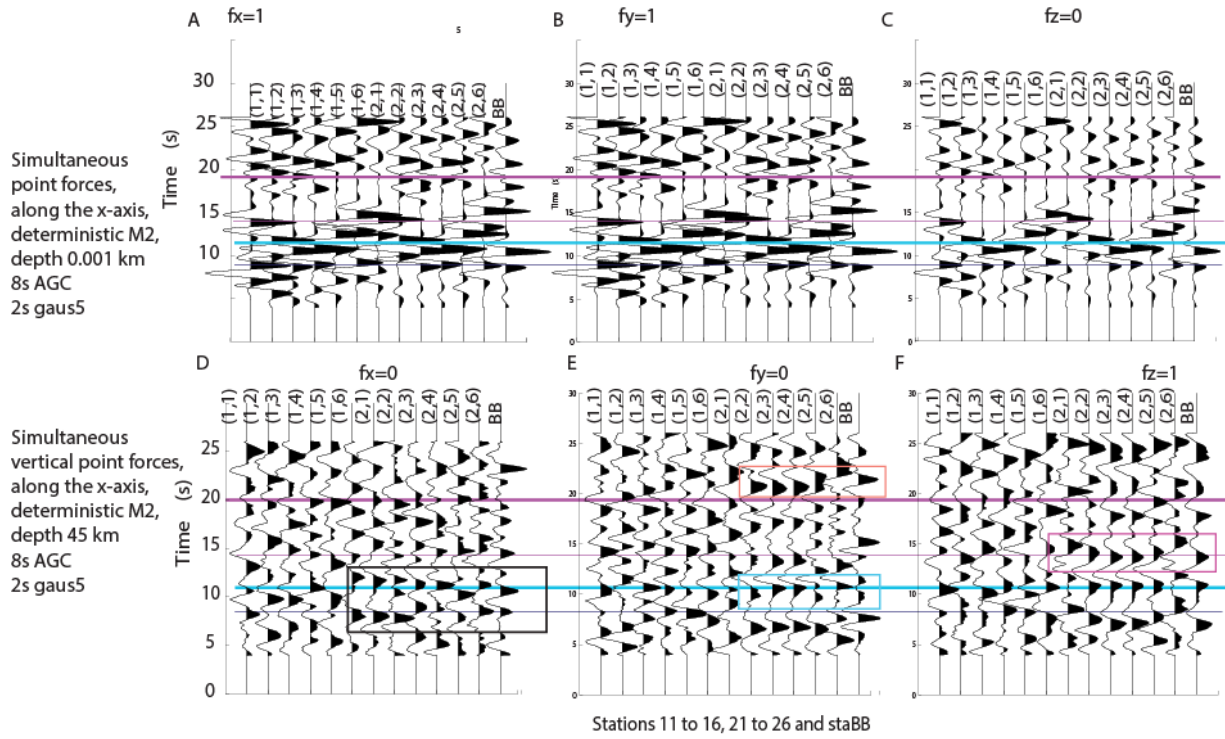


Figure 21. Line sources every 200 m along the x axis start at 0.36s at 1 m depth (plots A-C) and 45 km depth (plots D-F). In plots A-C Rayleigh waves propagate along the horizontal axes and are the largest arrivals at all stations (except for station BB) thus, only station BB was used to identify the arrivals (the last waveform to the right of each plot). Only SmS is visible in plots A-C. Waveforms are processed in the same way as for Figures 19 and 20. When the sources are at 45 km depth, the 25km P (thin blue line) and S (magenta rectangle) reflections, and Moho P and S-reflections are observed, on the vertical components, as well as on the horizontal components. Arrivals are observed on all the components when the source is only vertical, or only horizontal.

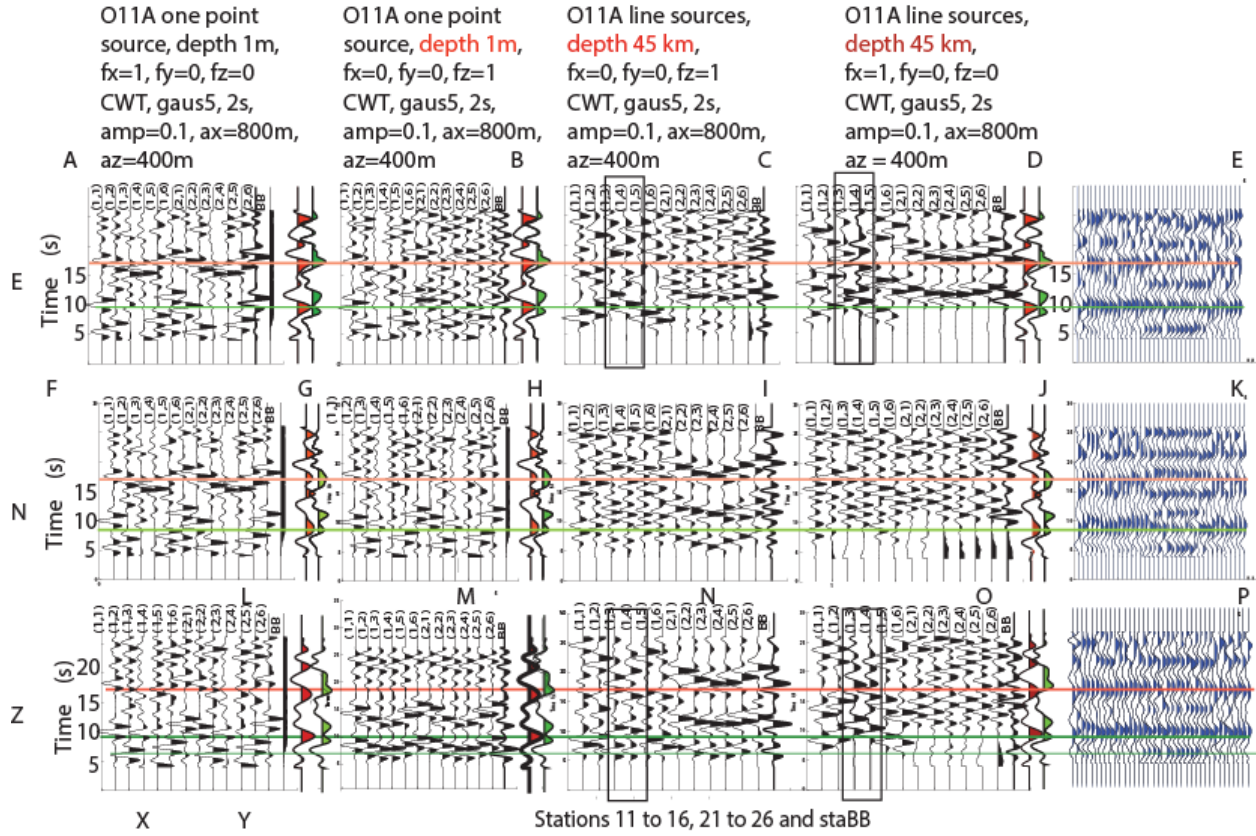


Figure 22. Observed (plots E, K and P) and synthetic waveforms at station O11A. GFALL (red) and GF2006360 (green) are represented, for each component, to the right of the synthetic waveforms in all plots except for E, K and P. Point sources and line sources are used with random models. Details of the random models used for synthetic waveform generation are above each set of plots for components E (plots on the upper row), N (plots on the middle row) and Z (plots on the lower row). The deterministic model to which random velocity was added is M2 in Appendix 1, Table A1.3. For source depth 1 m only SmS could be identified at stations other than BB (in good correspondence with the synthetic waveforms), as the first 10s are contaminated by Rayleigh waves. When PmP could not be identified at station BB (plot O), the two nearby stations in the black boxes, at 5km and 10 km distance (in black rectangles), show PmP arrivals. The thin blue line shows P(25km)P (best in plots I and N) and corresponds to extra arrivals observed (plots K and P) during the summer months.

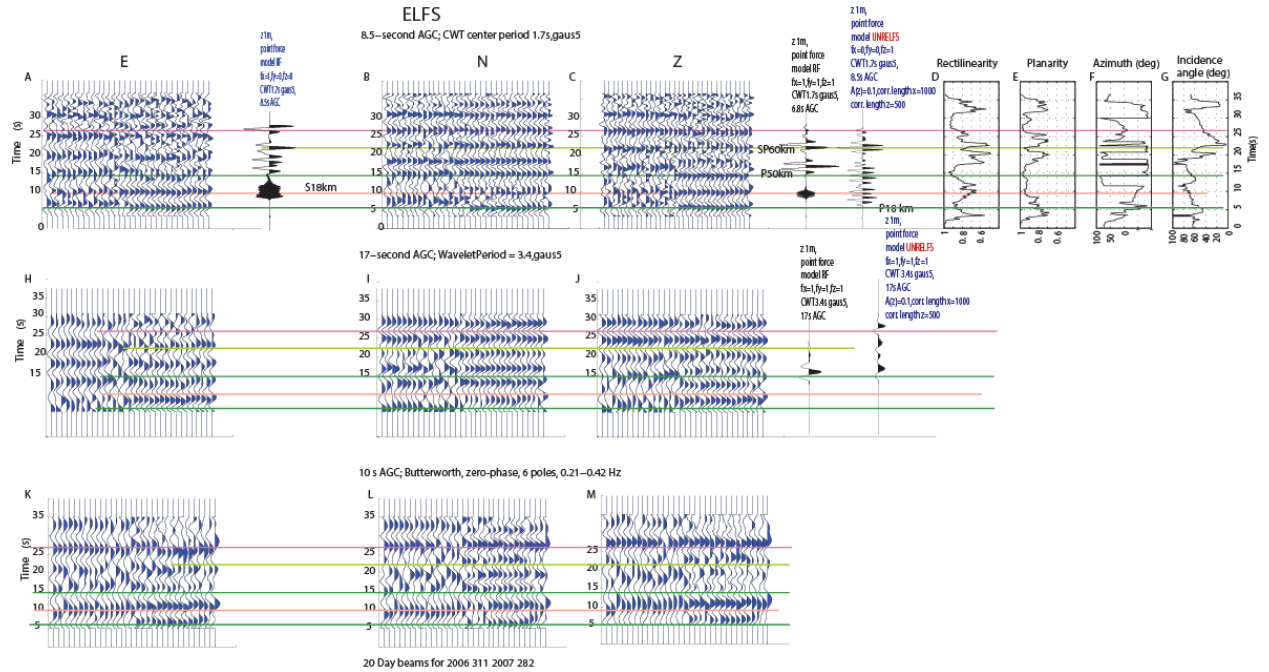


Figure 23. Panels of 20-day GFs CWT filtered (plots 1-J) and Fourier filtered (plots K-M) at station ELFS. In each plot, note GF pattern changes in the winter to the left and in the summer to the right. The summer months have more high frequency ambient noise which results in systematic arrival time variations, which could possibly be due to predominant ambient noise back azimuth changes (this hypothesis is suggested by the synthetic waveforms, however not investigated in detail in this study). The arrivals identified as P reflections are marked by green lines and the arrivals identified as S reflections are marked by magenta lines. Note the lack of arrivals at 15s time lag during the summer on the vertical component (plot M) at periods from 2.5 to 5s. The UNRELFS model (Appendix 1, Table A1.3), has inter-layer velocity variations smaller than 0.4km/s (Vp) and 0.3km/s (Vs) except at 18 km, thus there are no clear P-reflections from each of these layers. In plots A-C arrivals from an 18 km discontinuity with a velocity jump of 0.3 km/s in the model UNRELFS would be found at time lags 5.2s (P18km, green) and 9.3s (S18km, magenta). A P-phase reflected on a 50km discontinuity in the RFELFS (Appendix1, Table A1.3) models best the observations when all the waveforms are filtered with CWT gaus5, center period 1.7s and 3.4s, however, the ~15s arrival is not well distinguished on the Fourier filtered waveforms, possibly because of the filter (from 0.2-0.4Hz). The UNRELFS model predicts the SmS from 60 km at 28s time lag, however a P-reflection from a layer at 100 km depth (TWTT 26s) could also explain this arrival. This shows the importance of corroborative information for correct interpretation at each station. Plots D, E, F and G show polarization analysis and interpretation of P reflections (green) and S reflections (magenta). Another interpretation, which with the current method could not be ruled out, is that the arrivals at ~ 10s are a mix of P(30km)P and S(18km)S, while a weak arrival at 18s (not marked on the figure, occurring mostly on the horizontal components in plots I-J) is S(30km)S. The arrival at 22s could be interpreted as S(60km)P with the RFO05C model, or as P(60km)P with the UNR_O05C model in Appendix1, Table A1.3.

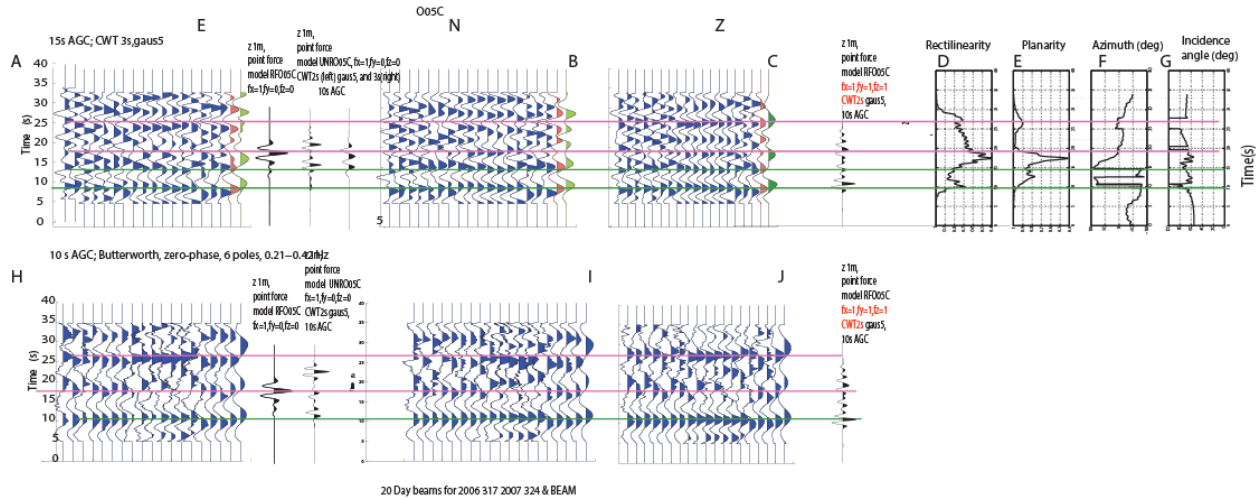


Figure 24. Similar to Figure 23, observed and synthetic waveforms at station O05C. Note similarity of the plots H-J to plots K-M in Figure 23, which is interpreted as similar deep reflector structure at the two stations. Plots D-G show polarization analysis and an interpretation of P reflections (green) and S reflections (magenta). In this case, the arrival at ~11s (corrected for 3s center period, see Figure 6) is interpreted as a P-reflection at 41km with a large (70°) incidence angle. An arrival at 14.6 (15.1s corrected time incidence angle 70°) is interpreted as P reflected from an ~ 50 km deep reflector. An arrival at ~ 19 s is interpreted as S(41km)S (corresponding to RFUNR modeled seismograms, incidence angle 65°), and one arrival at ~ 27 s (corrected time lag, incidence angle 80°) is interpreted as S(50km)S. Note that this interpretation corresponds to the receiver function model RFO05C.

Figure 25A

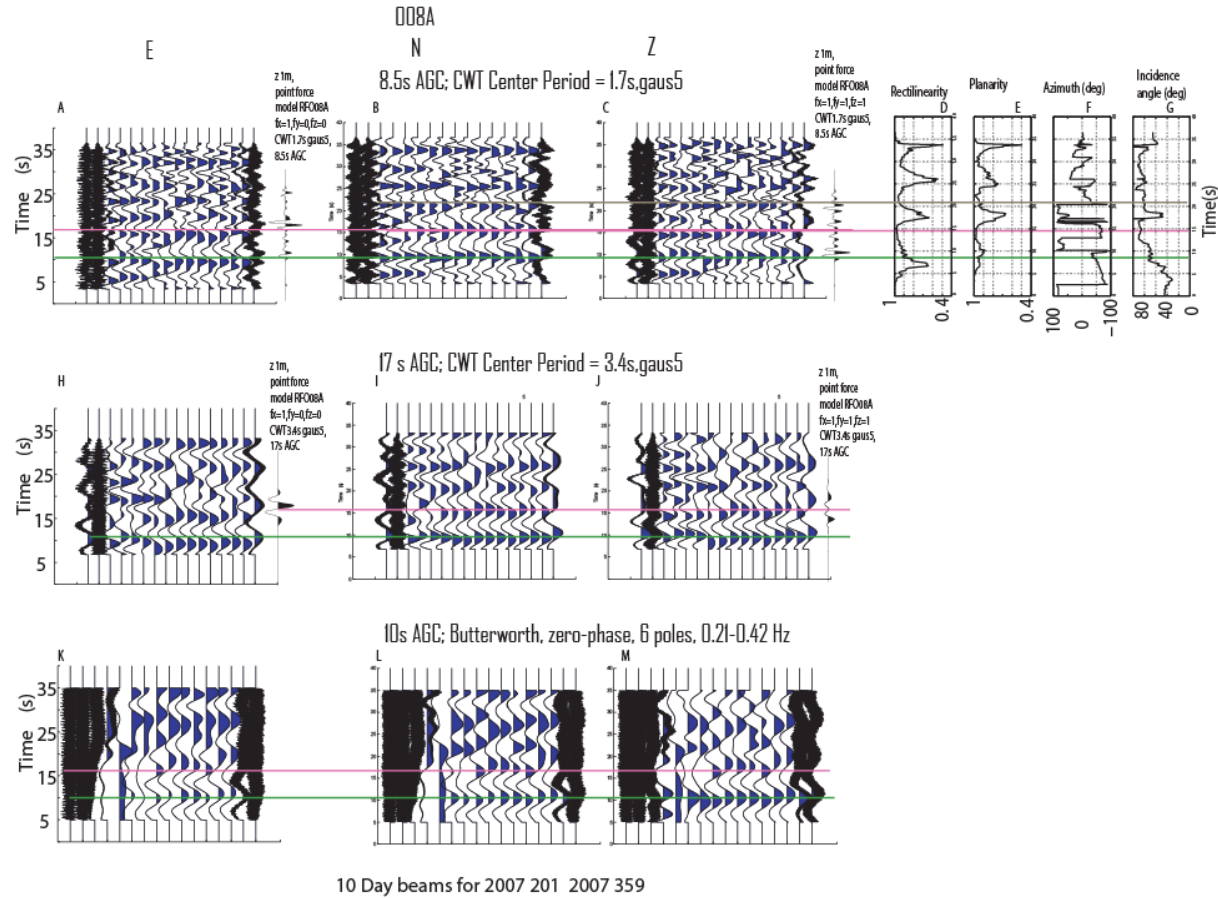


Figure 25. Similar to Figure 23, observed and synthetic waveforms at station 008A. Note best correspondence of the synthetic waveforms (model RFO08A) to GF2006360 (where visible) as opposed to GFALL. The cultural noise at O08A is affecting the 20-day GFs during the summer. Plot B (second column, top row) shows $\sim 70^\circ$ incidence angle for PmP and $\sim 90^\circ$ incidence angle for SmS. Another possible S-arrival is at ~ 22 s and is unidentified.

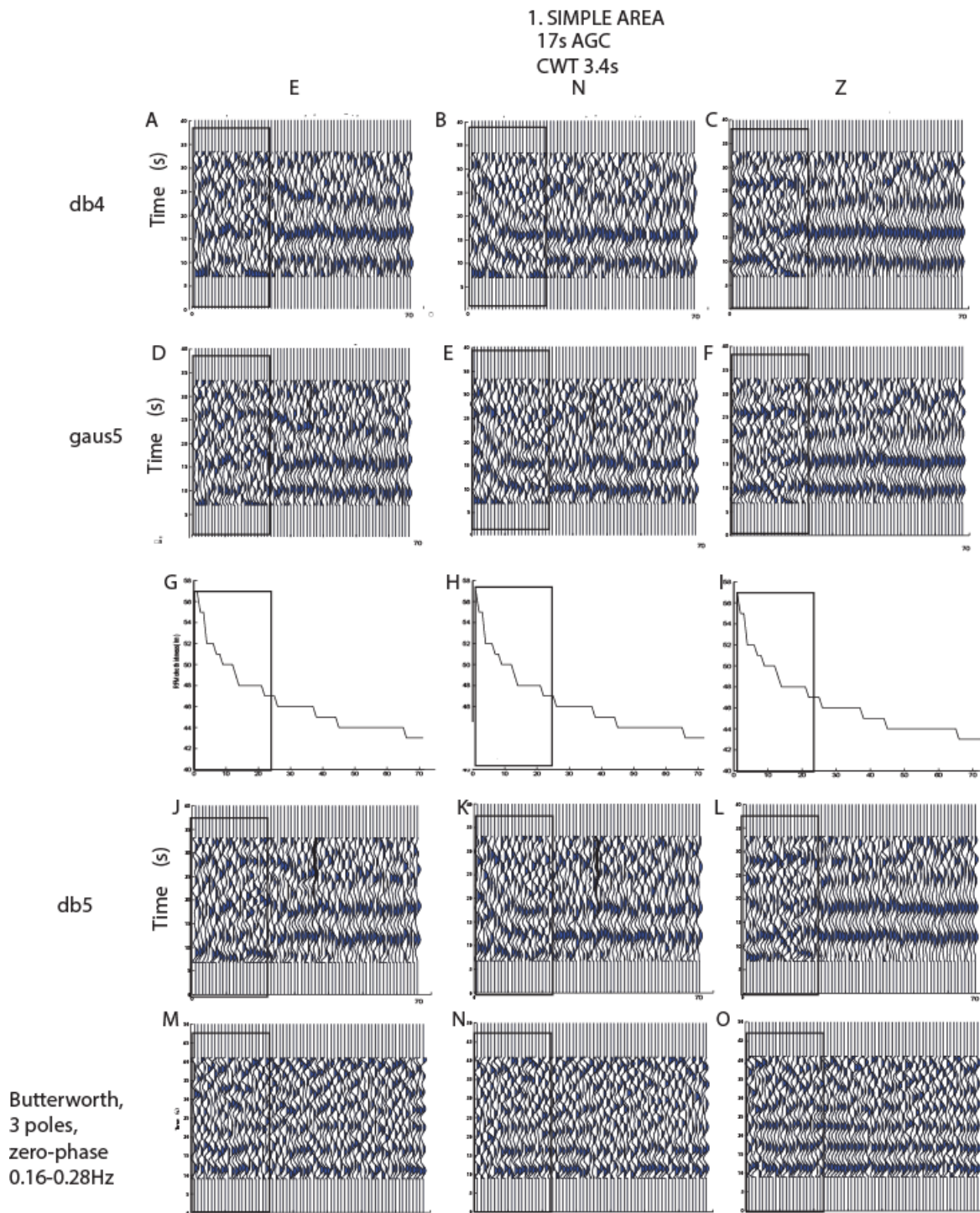


Figure 26. SIMPLE AREA Three wavelet representation of the 3C GFALL (extracted from 1-3 years of data) in the SIMPLE AREA. Plots G-I are the same plot, added for comparison on each column, and represent the EARS-estimated depth, using receiver function analysis. In all the other plots the stations are ordered according to EARS – estimated Moho depth. The stations to the south of the SIMPLE area are located in a region with relatively uniform Moho and are outside the box in every plot. When compared to stations in the TEST area, PmP arrives 1-2.5s later, independent

of the filtering method, after the corrections from Figure 6 have been applied. Note good similarity of db5 and Fourier-filtered waveforms, however, better resolution of wavelet- filtered waveforms for SmS from deepest crust. The SIMPLE group include stations to the north and northeast located at the transition to the thick crust of the Colorado Plateau (inside the black rectangles in each plot). Unlike the Z and E-components, the N component appears to show continuous variation as the depth increases from 44 to 55km. There is a clear difference between the “simple” crust and the increasing thickness crust. A slight P-TWTT reduction is observed as the crust thins to 40km (best for CWT using db4 and db5).

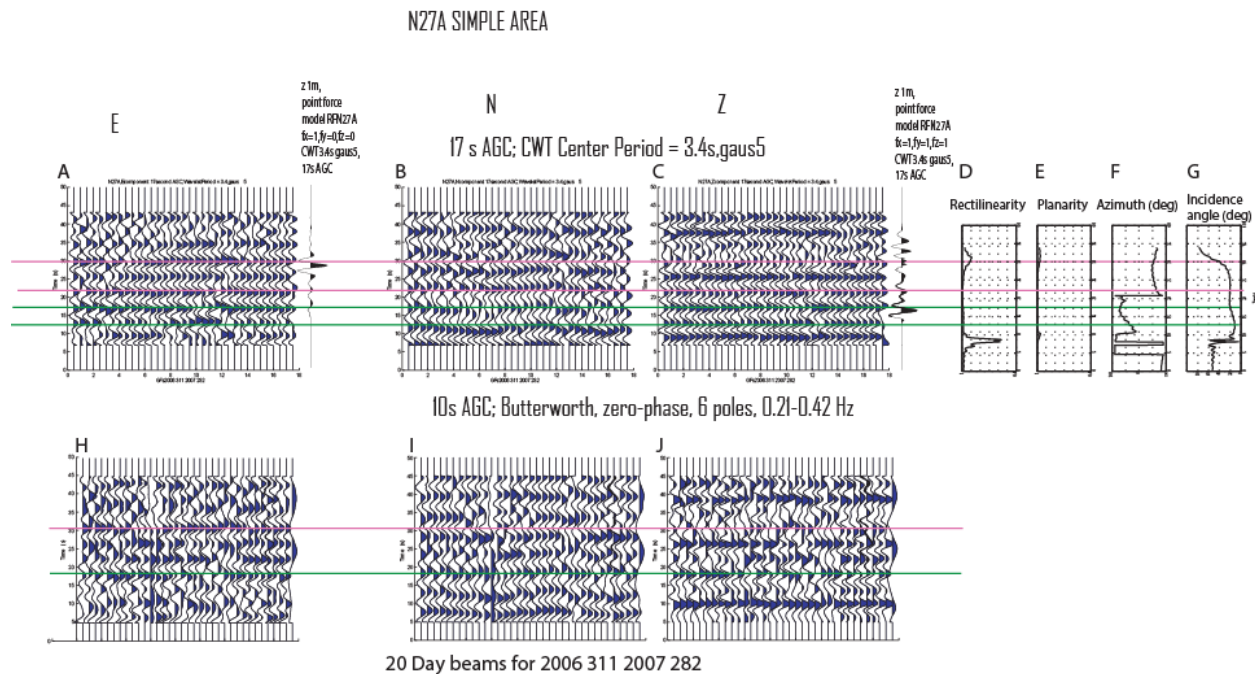


Figure 27. Similar to Figure 23, observed and synthetic waveforms at station N27A, SIMPLE AREA. The observed PmP and SmS are identified as reflections from a 50 km discontinuity, which is similar however, not exactly as predicted by the model RFN27A (Appendix 1, Table A1.3). PmP arrives at 18.2s (corrected time, see Figure 6) and SmS is identified at 30.75s (corrected time) with V_p/V_s 1.69. Another P-arrival is identified at 13.2s on the vertical component (plot C), with a corresponding S-reflection at 22.75 (V_p/V_s 1.72). Also note that PmP and SmS are vertically polarized in this case (plots D-G).

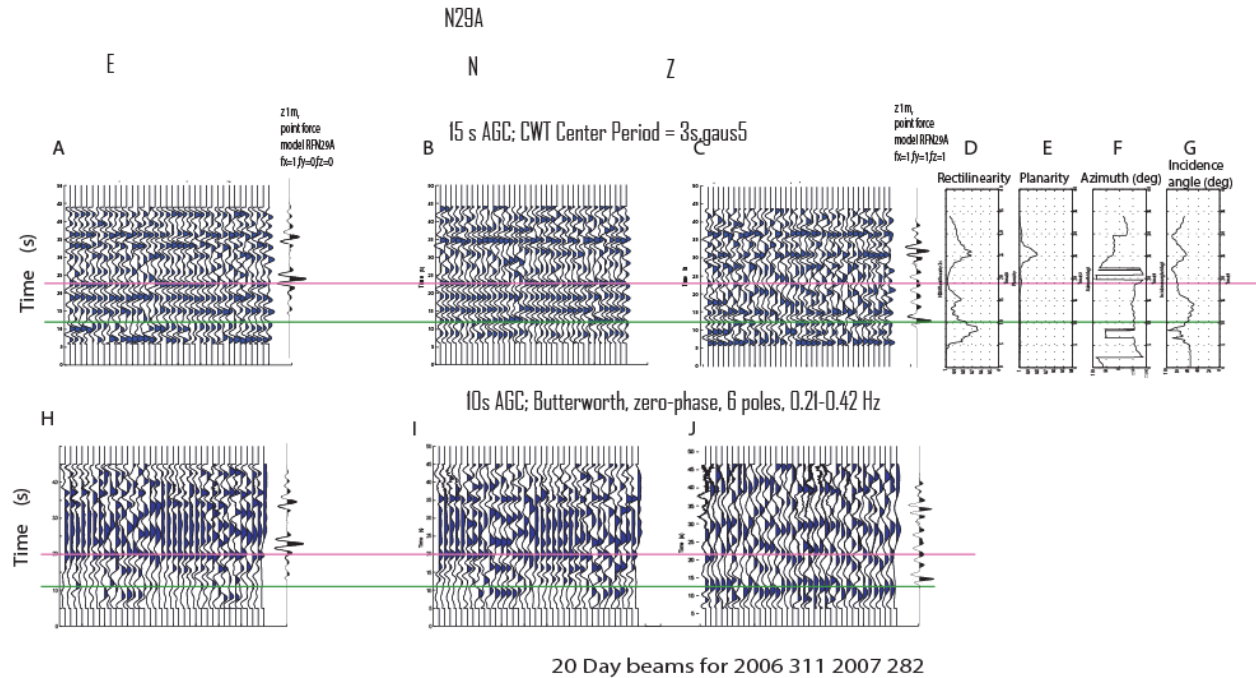


Figure 28. Similar to Figure 23, observed and synthetic waveforms at station N29A, SIMPLE AREA. The PmP (green line, at 12.5s) arrival is less clear in plot C than in plot J, and has a significant horizontal component (incidence angle $\sim 60^\circ$). Separation of PmP on the Z-component and of SmS (magenta line, at 22s, incidence angle 80°) on the horizontal components is observed here, while V_p/V_s is 1.76. Note that the model RFN29A shows too slow P and S velocities.

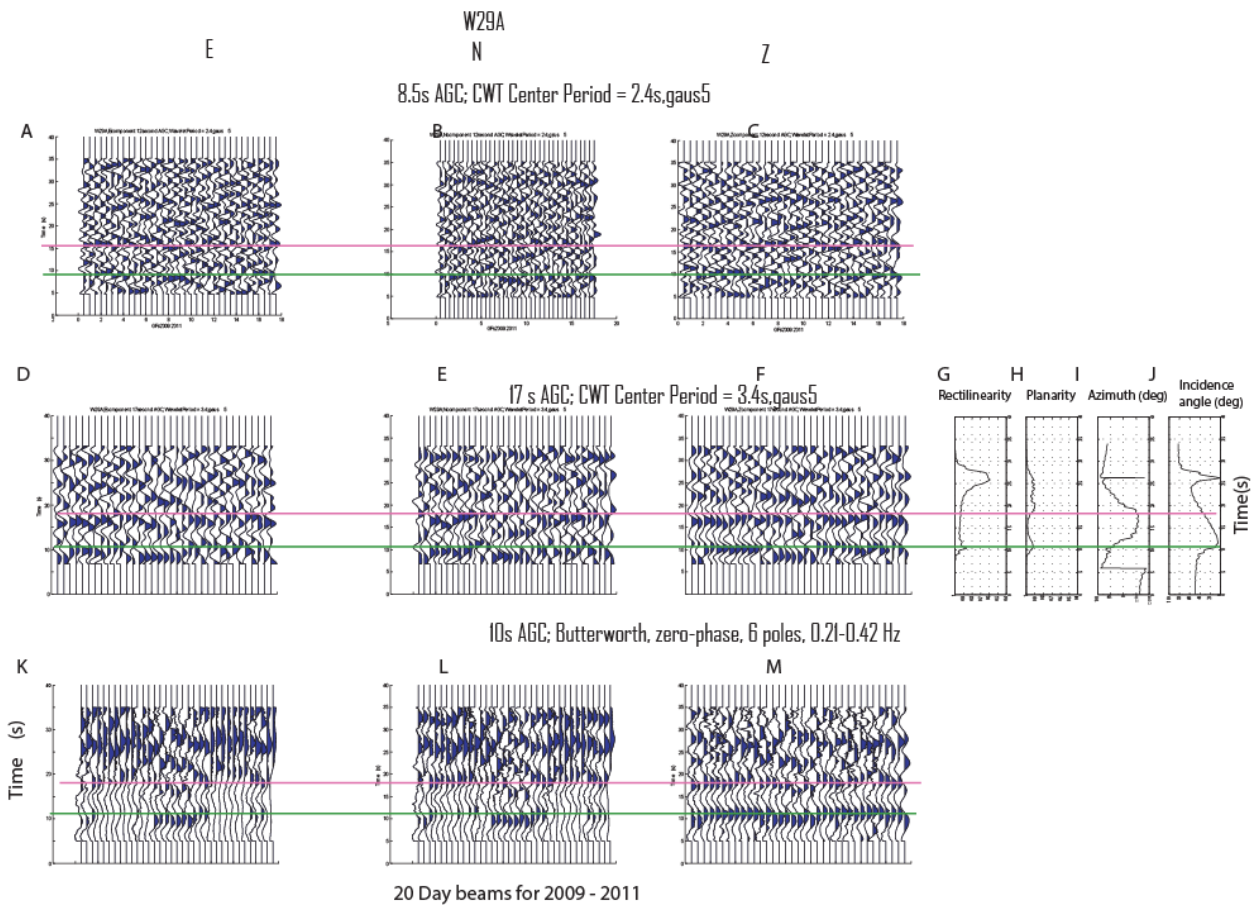


Figure 29. Similar to Figure 23, observed and synthetic waveforms at station W29A, SIMPLE AREA. A 40km crust explains the PmP (at 11s, green line, 5° incidence angle) and SmS (at 18s, magenta line and 40° incidence angle) observed at this station. Lack of clear reflections was observed at periods shorter than 3s. Note strong PmP in plot J, and F, and SmS in plots G and H (not in plot J) and in plots D and E.

2. COMPLEX AREA

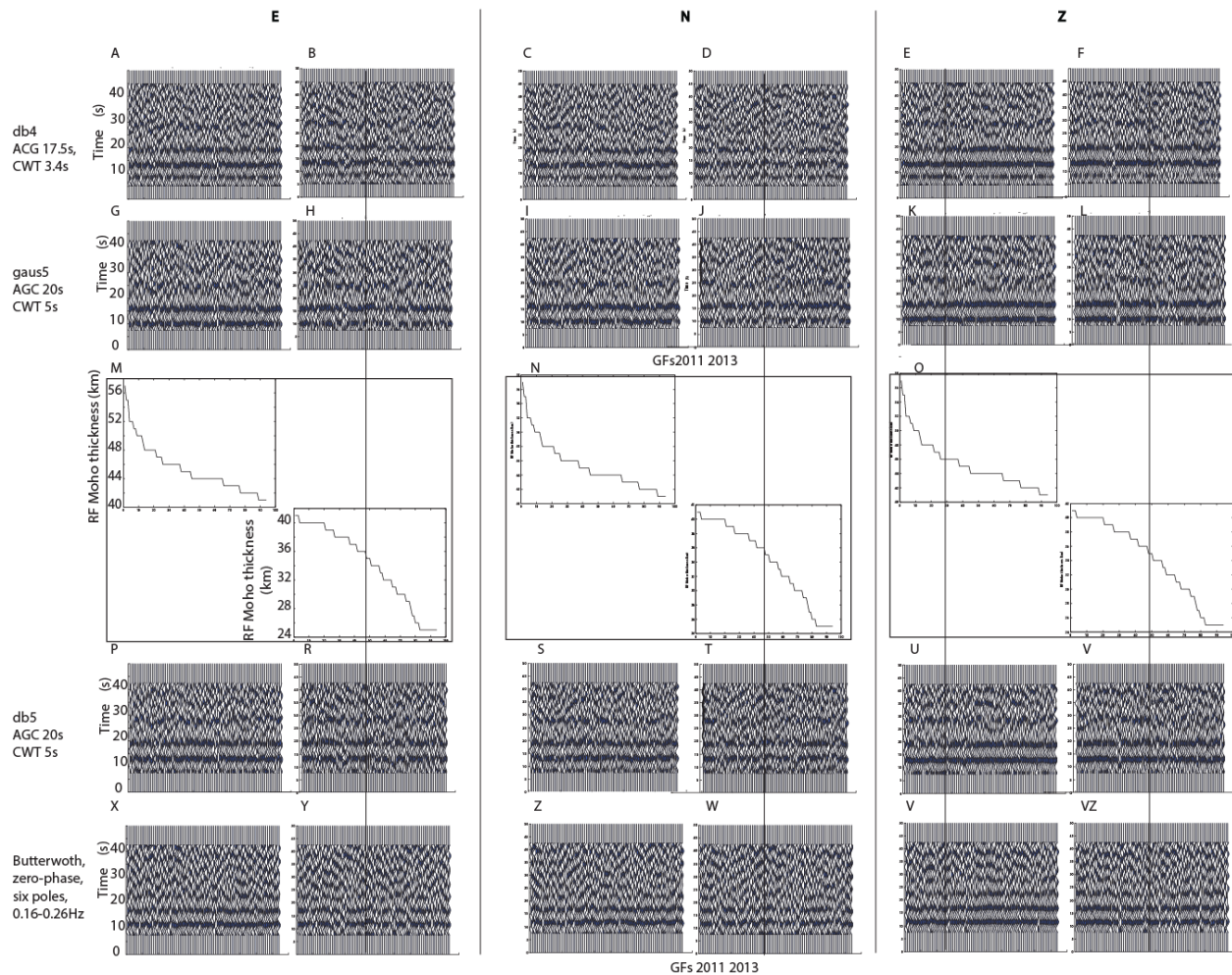


Figure 30. Same as in Figure 26, for the COMPLEX AREA. Pairs of plots, such as A and B (E component), C and D (N component) and E and F (Z component), show CWT and Butterworth filters, in comparison to the EARS-estimated depth. Unlike the case of the SIMPLE area, deeper crustal reflectors are not easily distinguishable. One explanation could be that the EARS depth estimations are less precise in this region, and that each station should be analyzed separately. The arrival at ~ 27 s is observed for deeper crust best on the Z component in plots K and L and U and V and drifts toward 25s where the EARS crustal thickness reaches 36km, after which is not visible. The horizontal components show little observable difference for deeper crust.

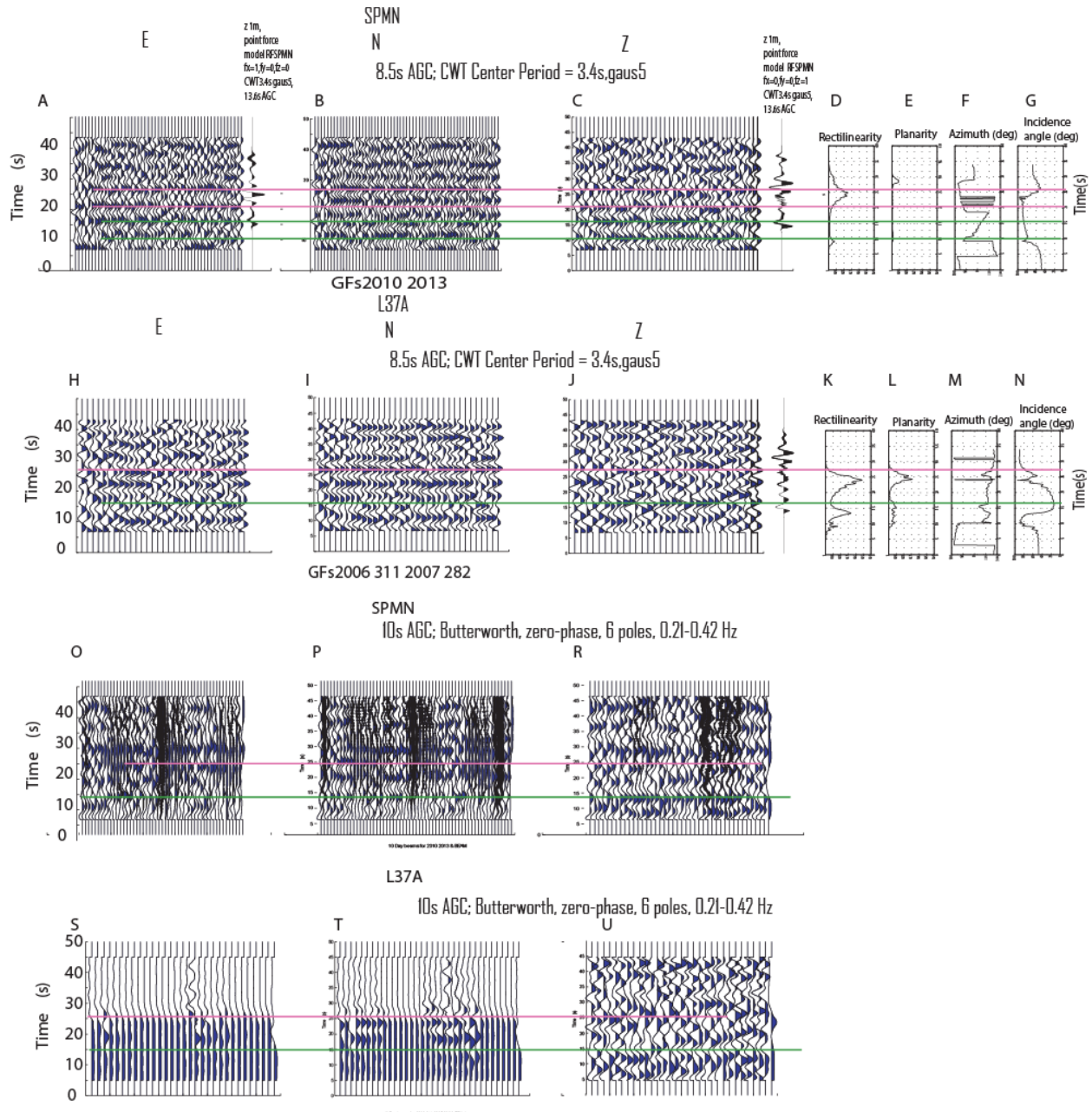


Figure 31. Similar to Figure 23, observed and synthetic waveforms at stations SPMN and L37A are shown for comparison. As estimated by Shen et al., 2013 in Appendix 1, Figure A1.1 SPMN has \sim constant gradient velocity up to 50km with a change at 35km and L37A has constant V_{sv} gradient up to \sim 25km and Moho at 50km. At SPMN an arrival at \sim 16.75s (corrected) is interpreted as PmP, however, it has a significant shear component (90° incidence angle), and arrivals at \sim 27.75s (\sim 45° incidence angle) are interpreted as SmS (V_p/V_s is 1.66). Also, an arrival is observed at \sim 10.75s, which is possibly a P-reflection from a compositional discontinuity at \sim 35 km, with a corresponding SmS at 21.75s and V_p/V_s of 1.66. At L37A (plots H-N) and plots R-T weak PmP reflections, with 15° incidence angle, are identified at 17.2s (corrected), with corresponding SmS (incidence angle 45°) at 28s (corrected), and V_p/V_s 1.6. Note that the Fourier

filtered panels show arrivals which are less clear than CWT filtered data at both stations. The RFSPMN model predicts the observed arrivals, however, the Vs of the RFL37A model is slower than observed.

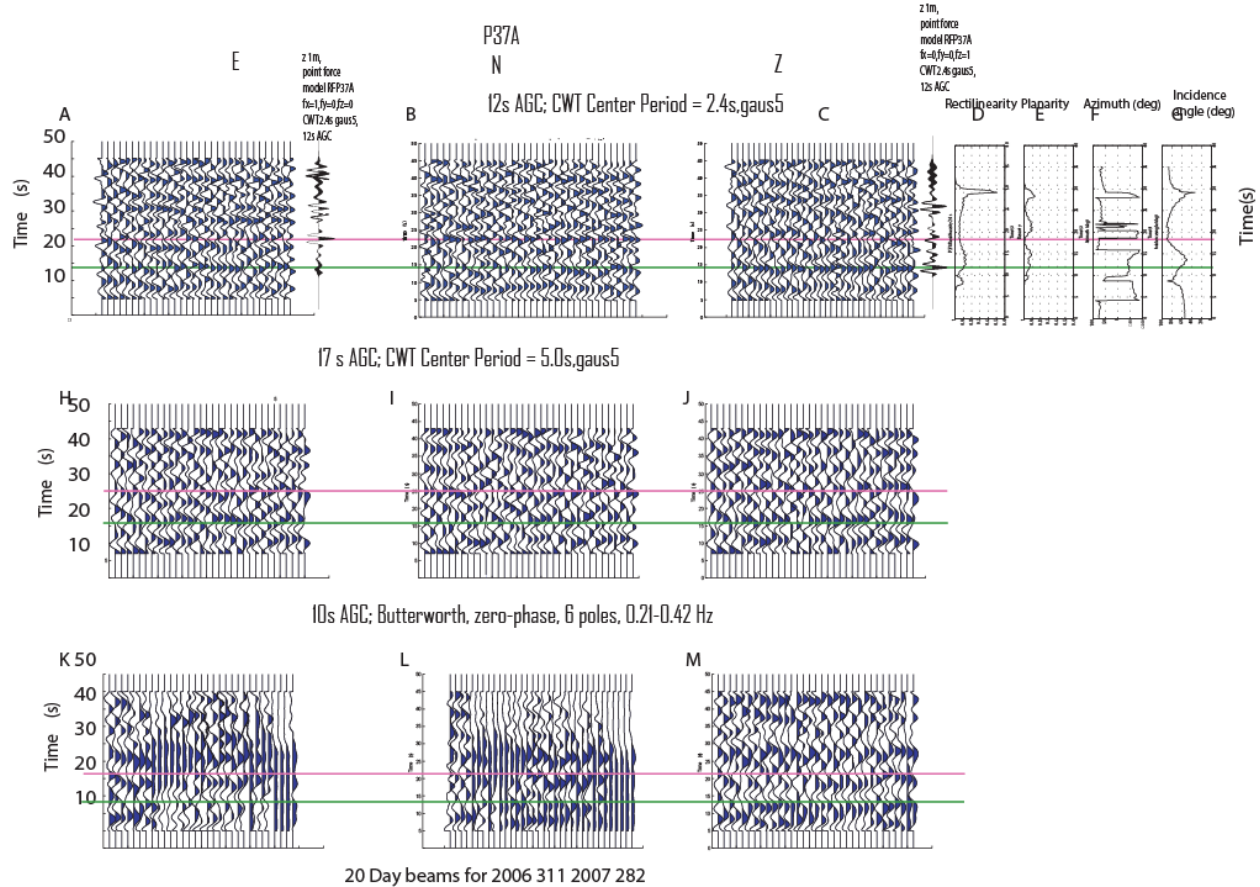


Figure 32. Similar to Figure 23, observed and synthetic waveforms at station P37A. Note clear PmP on the Z component (plot C) at ~ 14 s and SmS on the N-component at ~ 23 s. The Shen et al. 2011 model for this station has an upper crust with velocity increasing uniformly and a ~ 44 km Moho depth, which corresponds to the observed arrivals for this station. The synthetic arrivals were estimated using the Shen et al. model and match the GFs. The PmP incidence angle is $\sim 60^\circ$ (plot G) and the SmS incidence angle is 90° . Note that the Fourier analysis results in unclear GF panels.

REFERENCES

Anderson, J. G., I. Tibuleac, A. Anooshehpoor, G. Biasi, K. Smith, and D. von Seggern (2009), Exceptional Ground Motions Recorded during the 26 April 2008 Mw 5.0 Earthquake in Mogul, Nevada, *Bull. Seismol. Soc. Amer.*, **99**, pp. 3475-3486, doi: 10.1785/0120080352.

Arrowsmith, S. J., R. Whitaker, C. Katz, and C. Hayard (2009), The F-detector revisited: An improved strategy for signal detection at seismic and infrasound arrays, *Bull. Seism. Soc. Am.*, **99**, pp. 449-453, doi: 10.1785/0120080180.

Bensen, G. D., M. H. Ritzwoller, M. P. Barmin, A. L. Levshin, F. Lin, M. P. Moschetti, N. M. Shapiro, and Y. Yang (2007), Processing seismic ambient noise data to obtain reliable broad-band surface wave dispersion measurements, *Geophys. J. Int.*, **169**, pp. 1239-1260.

Blandford R.R. (1974), An automatic event detector at the Tonto forest observatory, *Geophysics*, **39**, pp. 633-643.

Claerbout J. F. (1968), Synthesis of a layered medium from its acoustic transmission response, *Geophysics*, **33**, pp. 264-269.

Douze, E. J. and S. J. Laster (1979), Seismic array noise studies at Roosevelt Hot Springs, Utah geothermal area, *Geophysics*, **44**, pp. 1570-1583.

Frassetto, A. M., George Zandt, Hersh Gilbert, Thomas J. Owens, and Craig H. Jones (2011), Structure of the Sierra Nevada from receiver functions and implications for lithospheric foundering, *Geosphere*, **7** (4), pp. 898-921, doi: 10.1130/GES00570.1.

Gorbatov, A., E. Saygin and B. L. N. Kennett (2013), Crustal properties from seismic station autocorrelograms, *Geophysical Journal International*, **192** (2), pp. 861-870.

Harben, P. E. and E. Hjortenberg (1993), Variation in microseism power and direction of approach in northeast Greenland, *Bulletin of the Seismological Society of America*, **83**, 6, pp. 1939-1958.

Hillers, G. and Y. Ben-Zion (2011), Seasonal variations of observed noise amplitudes at 2–18 Hz in southern California, *Geophysical Journal International*, **184**, 2, Blackwell Publishing Ltd 1365-246X, <http://dx.doi.org/10.1111/j.1365-246X.2010.04886.x>, doi: 10.1111/j.1365-246X.2010.04886.x.

Klemperer, S. L., T. A. Hauge, E. C. Hauser, J. E. Oliver, and C. J. Potter (1986), The Moho in the northern Basin and Range Province, Nevada, along the COCORP 40°N seismic reflection transect, *Geological Society of America Bulletin*, **97** (5), pp. 603–618.

Koper, K. D., K. Seats, and H. Benz (2010), On the Composition of Earth's Short-Period Seismic Noise Field, *Bull. Seism. Soc. of Am.*, **100**, No. 2, pp. 606-617, doi: 10.1785/0120090120.

Larkin, S. P., A. Levander, T. J. Henstock, and S. Pullammanappallil (1997), Is the Moho flat? Seismic evidence for a rough crust-mantle interface beneath the northern Basin and Range, *Geology*, **25**, 5, pp. 451-454.

Lobkis, O. I. and R. L. Weaver (2001), On the emergence of the Green's function in the correlations of a diffusive field, *J. Acoust. Soc. Am.*, **110**, pp. 3011-3017.

Larose, E., A. Derode, D. Clorennec, L. Margerin, and Michel Campillo, (2005), Passive retrieval of Rayleigh waves in disordered elastic media, *Phys. Rev. E*, **72**, doi:10.1103/PhysRevE.72.046607.

Louie, J. N., W. Thelen, S. B. Smith, J. B. Scott, M. Clark, and S. Pullammanappallil (2004), The Northern Walker Lane refraction experiment: Pn arrivals and the northern Sierra Nevada root, *Tectonophysics*, **388**, 1-4, pp. 253-269.

Petersson, N. A. and B. Sjogreen (2014), Super-grid Modeling of the Elastic Wave Equation in Semibounded Domains, *Communications in Computational Physics*, **16**, pp. 913-955.

Priestley, K. and J. Brune (1978), Surface waves and the structure of the Great Basin of Nevada and western Utah, *J. Geophys. Res.*, **83**, B5, pp. 2265-2272, doi:10.1029/JB083iB05p02265.

Sanchez-Sesma F. J. and M. Campillo (2006), Retrieval of the Green's Function from Cross Correlation: The Canonical Elastic Problem, *Bull. Seism. Soc. Am.*, **96**, pp. 1182-1191.

Schulte-Pelkum, V. and K. H. Mahan (2014), A method for mapping crustal deformation and anisotropy with receiver functions and first results from USArray, *Earth and Planetary Science Letters*, **402**, pp. 221-233.

Seats, K. J., J. F. Lawrence, and G. Prietom (2012), Improved ambient noise correlation functions using Welch's method, *Geophys. J. Int.*, **188**, pp. 513-523, doi:10.1111/j.1365-246X.2011.05263.x.

Shen, W., Michael H. Ritzwoller, and Vera Schulte-Pelkum (2013), Crustal and uppermost mantle structure in the central U.S. encompassing the Midcontinent Rift, *Journal Of Geophysical Research: Solid Earth*, **118**, pp. 4325-4344, doi:10.1002/jgrb.50321.

Sigloch, K., N. McQuarrie, and G. Nolet (2008), Two-stage subduction history under North America inferred from multiple-frequency tomography, *Nature Geoscience* **1**, pp. 458-462.

Tibuleac, I. M., D. H. von Seggern, J. N. Louie, and J. G. Anderson (2009), High Resolution Seismic Velocity Structure in the Reno Basin from Ambient Noise Recorded by a Variety of Seismic Instruments, *GRC Transactions*, **33**, pp. 143-146.

Tibuleac, I. M. and D. H. von Seggern (2012), Crust-mantle boundary reflectors in Nevada from noise auto-correlations, *Geophys. J. Int.*, **189**, Issue 1, pp. 493-500.

Tibuleac, I., D. von Seggern, J. Iovenitti, J. Sainsbury, G. Biasi, and J. G. Anderson (2013), EGS Exploration Methodology Development Using the Dixie Valley Geothermal District as a Calibration Site, The Seismic Analysis Component, Proceedings, 38th Workshop on Geothermal Reservoir Engineering Stanford University, Stanford, California, February 11-13.

Von Seggern, D. H., I. M. Tibuleac, and J. N. Louie (2009), Computing Green's Functions from Ambient Noise Recorded by Narrow-Band Seismometers, Accelerometers, and Analog Seismometers, abstract presented at the 2009 Annual Meeting Announcement Seismological Society of America, Monterey, CA, April 8-10.

Wapenaar, K. (2004), Retrieving the elastodynamic Green's function of an arbitrary inhomogeneous medium by cross-correlation, *Physical Review Letters*, **93**, 254301.

Wegler, U. and C. Sens-Schönfelder (2007), Fault Zone Monitoring with Passive Image Interferometry, *Geophys. J. Int.*, **168**, pp. 1029-1033.

Williams, C. F. and John H. Sass (1997), Thermal Signature of Subsurface Fluid Flow Near the Dixie Valley Geothermal Field, NV, p. 8, Proceedings of the Twenty-Second Workshop on Geothermal Reservoir Engineering, Twenty-Second Workshop on Geothermal Reservoir Engineering, Stanford University, Stanford, CA, August 26.

Withers, M. M., R. C. Aster, C. J. Young, and E. P. Chael (1996), High frequency analysis of seismic background noise as a function of wind speed and shallow depth, *Bull. Seism. Soc. Am.*, **86**, pp. 1507-1515.

Yang, Y. and M. H. Ritzwoller (2008), Teleseismic surface wave tomography in the western U.S. using the Transportable Array component of USArray, *Geophys. Res. Lett.*, **35**, L04308, doi:10.1029/2007GL032278.

APPENDIX

LIST OF FIGURES AND TABLES

FIGURES

Figure A-1. COMPLEX region crustal models estimated by Shel et al., 2013, extracted in Table A-3	74
--	----

TABLES

Table A-1a. Station location and receiver function information for the TEST region	62
--	----

Table A-1b. Station location and receiver function information for the SIMPLE region. The stations selected for detailed analysis in this study have bold names.....	62
--	----

Table A-1c. Station location and receiver function information for the SIMPLE region. The stations selected for detailed analysis in this study have bold names.....	64
--	----

Table A-2. Models used in synthetic waveform modeling	70
---	----

Table A-3. Custom velocity models used for synthetic waveform modeling at the TEST, SIMPLE and COMPLEX stations	70
---	----

Table A-4. Position of virtual station used for waveform modeling	73
---	----

Table A-1a. Station location and receiver function information for the TEST region.

#Net	Station	Lat	Long	Elev	Est. Thick	Std Dev	Est. Vp/ Vs	Std Dev	Assumed Vp	Vs	TWTT Vp	TWTT Vs	Poissons Ratio	Num EQ	Complexity
TA	ELFS	40.62	-120.73	1553 m	50 km	1.2	1.67	0.02	6.566 km/s	3.932 km/s	15.230 s	25.432 s	0.22	50	0.58
AZ	ELKS	33.58	-116.45	1169 m	28 km	0.5	1.75	0.03	6.264 km/s	3.579 km/s	8.940 s	15.647 s	0.26	16	0.24
TA	O05C	39.96	-120.92	1032 m	41 km	3.7	1.79	0.09	6.597 km/s	3.685 km/s	12.430 s	22.252 s	0.27	60	0.72
TA	O06A	40.165	-119.8275	1229 m	33 km	0.6	1.81	0.02	6.276 km/s	3.467 km/s	10.516 s	19.037 s	0.28	66	0.57
TA	O07A	40.1614	-118.8772	1203 m	32 km	0.2	1.67	0.02	6.276 km/s	3.758 km/s	10.198 s	17.030 s	0.22	75	0.45
TA	O08A	40.2903	-118.155	2138 m	32 km	0.3	1.65	0.02	6.276 km/s	3.804 km/s	10.198 s	16.824 s	0.21	42	0.25
TA	O09A	40.1697	-117.1899	1492 m	25 km	0.2	2.08	0.02	6.276 km/s	3.017 km/s	7.967 s	16.573 s	0.35	53	0.63
TA	O10A	40.2917	-116.4999	1470 m	30 km	0.5	1.86	0.03	6.276 km/s	3.374 km/s	9.560 s	17.783 s	0.3	48	0.54
TA	O11A	40.1313	-115.657	1948 m	33 km	0.4	1.76	0.02	6.276 km/s	3.566 km/s	10.516 s	18.508 s	0.26	72	0.49
TA	O12A	40.2679	-114.7454	1743 m	30 km	0.2	1.74	0.01	6.276 km/s	3.607 km/s	9.560 s	16.634 s	0.25	83	0.27
TA	O13A	40.13	-113.98	1573 m	44 km	6.1	2.06	0.08	6.276 km/s	3.047 km/s	14.022 s	28.881 s	0.35	32	0.8

Table A-1b. Station location and receiver function information for the SIMPLE region. The stations selected for detailed analysis in this study have bold names.

#Net	Station	Lat	Long	Elev	Est. Thick	Std Dev	Est. Vp/ Vs	Std Dev	Assumed Vp	Vs	TWTT Vp	TWTT Vs	Poissons Ratio	Num EQ	Complexity
TA	125A	32.6588	-104.6573	1212 m	45 km	0.9	1.77	0.03	6.232 km/s	3.521 km/s	14.442 s	25.561 s	0.27	49	0.64
TA	126A	32.6462	-104.0204	1032 m	43 km	0.8	1.8	0.01	6.232 km/s	3.462 km/s	13.800 s	24.841 s	0.28	45	0.53
TA	127A	32.6764	-103.3575	1160 m	26 km	10	1.6	0.16	6.129 km/s	3.831 km/s	8.484 s	13.573 s	0.18	48	0.97
TA	128A	32.6213	-102.485	966 m	30 km	1.8	1.6	0.01	6.129 km/s	3.831 km/s	9.790 s	15.662 s	0.18	42	0.8
TA	129A	32.6309	-101.8662	876 m	49 km	0.3	1.81	0.01	6.426 km/s	3.55 km/s	15.251 s	27.606 s	0.28	36	0.41
TA	225A	32.11	-104.82	1703 m	30 km	14	2.07	0.19	6.232 km/s	3.011 km/s	9.628 s	19.927 s	0.35	40	0.78
TA	226A	32.0618	-104.1014	929 m	28 km	2.5	1.61	0.06	6.232 km/s	3.871 km/s	8.986 s	14.467 s	0.19	23	0.69
TA	227A	32.012	-103.2924	879 m	38 km	4.5	1.6	0.13	6.129 km/s	3.831 km/s	12.400 s	19.838 s	0.18	26	0.91
TA	228A	32.118	-102.5918	954 m	42 km	2.2	1.86	0.03	6.129 km/s	3.295 km/s	13.705 s	25.493 s	0.3	37	0.61
TA	229A	31.97	-101.81	804 m	43 km	8.1	1.81	0.11	6.38 km/s	3.525 km/s	13.480 s	24.397 s	0.28	25	0.72
TA	N25A	40.8132	-104.0873	1607 m	39 km	3.7	2.08	0.07	6.306 km/s	3.032 km/s	12.369 s	25.726 s	0.35	24	0.6
TA	N26A	40.83	-103.22	1284 m	35 km	5.0	2.08	0.11	6.483 km/s	3.117 km/s	10.797 s	22.457 s	0.35	29	0.76
TA	N27A	40.8063	-102.5367	1228 m	51 km	6.3	1.76	0.13	6.483 km/s	3.684 km/s	15.733 s	27.687 s	0.26	31	0.79
TA	N28A	40.6873	-101.5406	1009 m	52 km	2.2	1.6	0.06	6.483 km/s	4.052 km/s	16.042 s	25.666 s	0.18	21	0.81

Table A-1b. Station location and receiver function information for the SIMPLE region. The stations selected for detailed analysis in this study have bold names (continued).

TA	N29A	40.82	-100.63	897 m	34 km	7.5 km	1.75	0.14	6.483 km/s	3.705 km/s	10.489 s	18.354 s	0.26	30	0.8
TA	O25A	40.1129	-104.1201	1444 m	34 km	5.0 km	2.1	0.1	6.306 km/s	3.003 km/s	10.783 s	22.644 s	0.35	31	0.82
TA	O26A	40.2422	-103.3128	1413 m	38 km	13 km	2.1	0.22	6.483 km/s	3.087 km/s	11.723 s	24.619 s	0.35	18	0.69
TA	O27A	40.19	-102.4794	1206 m	33 km	5.7 km	2.1	0.13	6.483 km/s	3.087 km/s	10.180 s	21.380 s	0.35	30	0.79
TA	O28A	40.1262	-101.7735	1032 m	43 km	4.6 km	1.63	0.15	6.483 km/s	3.977 km/s	13.265 s	21.624 s	0.2	30	0.83
TA	O29A	40.1253	-100.7977	826 m	45 km	4.8 km	1.89	0.07	6.483 km/s	3.43 km/s	13.882 s	26.239 s	0.31	40	0.66
TA	P25A	39.5125	-104.168	1753 m	45 km	5.3 km	1.85	0.07	6.159 km/s	3.329 km/s	14.613 s	27.035 s	0.29	27	0.59
TA	P26A	39.5602	-103.3465	1566 m	45 km	2.8 km	1.83	0.06	6.242 km/s	3.411 km/s	14.418 s	26.385 s	0.29	29	0.6
TA	P27A	39.5559	-102.5782	1286 m	45 km	0.8 km	1.75	0.05	6.242 km/s	3.567 km/s	14.418 s	25.231 s	0.26	25	0.66
TA	P28A	39.5732	-101.7548	1105 m	48 km	6.9 km	1.8	0.08	6.483 km/s	3.602 km/s	14.808 s	26.652 s	0.28	32	0.66
TA	P29A	39.6021	-100.9316	929 m	42 km	2.2 km	1.86	0.04	6.483 km/s	3.485 km/s	12.957 s	24.103 s	0.3	40	0.61
TA	Q25A	38.9145	-104.2472	2001 m	41 km	5.1 km	2.1	0.13	6.159 km/s	2.933 km/s	13.314 s	27.958 s	0.35	25	0.83
TA	Q26A	38.9234	-103.5195	1546 m	51 km	2.5 km	1.6	0.11	6.242 km/s	3.901 km/s	16.341 s	26.147 s	0.18	44	0.84
TA	Q28A	39.0623	-101.8309	1133 m	43 km	0.9 km	1.83	0.08	6.483 km/s	3.543 km/s	13.265 s	24.273 s	0.29	30	0.61
TA	Q29A	38.8905	-100.9787	895 m	46 km	2.1 km	1.78	0.04	6.483 km/s	3.642 km/s	14.191 s	25.261 s	0.27	33	0.59
TA	R25A	38.1474	-104.2834	1461 m	48 km	1.5 km	1.69	0.03	6.159 km/s	3.644 km/s	15.587 s	26.345 s	0.23	44	0.68
TA	R26A	38.3009	-103.447	1304 m	33 km	7.9 km	2.1	0.17	6.242 km/s	2.972 km/s	10.574 s	22.207 s	0.35	42	0.76
TA	R27A	38.2859	-102.798	1201 m	44 km	0.3 km	1.73	0.01	6.242 km/s	3.608 km/s	14.098 s	24.390 s	0.25	40	0.48
TA	R28A	38.3423	-101.8106	1108 m	28 km	7.5 km	1.7	0.1	6.483 km/s	3.814 km/s	8.638 s	14.683 s	0.24	35	0.87
TA	R29A	38.4243	-101.1383	957 m	45 km	9.0 km	1.88	0.1	6.483 km/s	3.448 km/s	13.882 s	26.102 s	0.3	32	0.63
TA	T25A	37.1388	-104.4108	2017 m	42 km	1.0 km	1.78	0.03	6.316 km/s	3.548 km/s	13.300 s	23.675 s	0.27	189	0.66
TA	T26A	37.1747	-103.5933	1830 m	42 km	1.5 km	1.75	0.02	6.306 km/s	3.603 km/s	13.321 s	23.314 s	0.26	37	0.59
TA	T27A	37.0614	-102.7214	1366 m	45 km	0.9 km	1.81	0.02	6.306 km/s	3.484 km/s	14.272 s	25.832 s	0.28	37	0.55
TA	T28A	37.1204	-102.1136	1148 m	45 km	0.5 km	1.76	0.01	6.306 km/s	3.583 km/s	14.272 s	25.119 s	0.26	33	0.53
TA	T29A	37.1565	-101.2942	936 m	45 km	0.3 km	1.82	0.01	6.483 km/s	3.562 km/s	13.882 s	25.267 s	0.28	36	0.38
TA	U25A	36.3998	-104.4081	1845 m	44 km	0.2 km	1.75	0.01	6.316 km/s	3.609 km/s	13.933 s	24.383 s	0.26	58	0.42
TA	U26A	36.3945	-103.7439	1861 m	44 km	0.3 km	1.79	0.01	6.306 km/s	3.523 km/s	13.955 s	24.979 s	0.27	49	0.46
TA	U27A	36.4213	-102.8246	1342 m	46 km	7.2 km	1.8	0.12	6.306 km/s	3.503 km/s	14.589 s	26.263 s	0.28	21	0.73
TA	U28A	36.3793	-102.2243	1165 m	49 km	1.8 km	1.74	0.04	6.306 km/s	3.624 km/s	15.541 s	27.042 s	0.25	26	0.53
TA	U29A	36.4519	-101.2702	928 m	38 km	4.3 km	1.97	0.08	6.483 km/s	3.291 km/s	11.723 s	23.093 s	0.33	37	0.68
TA	V25A	35.8383	-104.6164	1861 m	51 km	1.2 km	1.7	0.02	6.419 km/s	3.776 km/s	15.890 s	27.013 s	0.24	57	0.55
TA	V26A	35.7964	-103.786	1362 m	47 km	1.8 km	1.69	0.04	6.242 km/s	3.693 km/s	15.059 s	25.454 s	0.23	51	0.68
TA	V27A	35.7569	-102.8361	1228 m	52 km	8.9 km	1.73	0.11	6.242 km/s	3.608 km/s	16.661 s	28.825 s	0.25	24	0.77
TA	V28A	35.7505	-102.2243	1163 m	44 km	1.4 km	1.88	0.03	6.242 km/s	3.32 km/s	14.098 s	26.506 s	0.3	35	0.42
TA	V29A	35.8734	-101.5209	953 m	32 km	6.9 km	2.09	0.15	6.426 km/s	3.075 km/s	9.960 s	20.813 s	0.35	31	0.83
TA	W25A	35.2177	-104.4606	1446 m	41 km	0.6 km	1.83	0.02	6.419 km/s	3.508 km/s	12.775 s	23.375 s	0.29	47	0.5

Approved for public release; distribution is unlimited.

Table A-1b. Station location and receiver function information for the SIMPLE region. The stations selected for detailed analysis in this study have bold names (continued).

TA	W26A	35.0891	-103.7656	1314 m	36 km	4.7 km	1.9	0.11	6.242 km/s	3.285 km/s	11.535 s	21.918 s	0.31	47	0.7
TA	W27A	35.0637	-103.0627	1233 m	43 km	1.5 km	1.81	0.1	6.242 km/s	3.449 km/s	13.778 s	24.935 s	0.28	42	0.59
TA	W28A	35.2574	-102.2063	1156 m	47 km	0.5 km	1.8	0.02	6.242 km/s	3.468 km/s	15.059 s	27.105 s	0.28	35	0.42
TA	W29A	35.1212	-101.6476	1072 m	40 km	6.0 km	1.95	0.11	6.426 km/s	3.295 km/s	12.449 s	24.279 s	0.32	26	0.78
TA	X25A	34.5271	-104.6621	1494 m	43 km	3.4 km	1.77	0.06	6.419 km/s	3.627 km/s	13.398 s	23.711 s	0.27	49	0.72
TA	X26A	34.5508	-103.8103	1393 m	38 km	3.1 km	1.92	0.07	6.242 km/s	3.251 km/s	12.176 s	23.377 s	0.31	48	0.66
TA	X27A	34.6469	-103.0974	1304 m	38 km	1.6 km	1.95	0.04	6.242 km/s	3.201 km/s	12.176 s	23.743 s	0.32	47	0.54
TA	X28A	34.5185	-102.1973	1160 m	34 km	4.7 km	1.95	0.12	6.242 km/s	3.201 km/s	10.894 s	21.243 s	0.32	29	0.7
TA	X29A	34.4452	-101.7008	1039 m	44 km	1.7 km	1.91	0.06	6.426 km/s	3.364 km/s	13.694 s	26.159 s	0.31	24	0.74
TA	Y25A	33.9229	-104.6928	1364 m	48 km	5.2 km	1.87	0.1	6.232 km/s	3.333 km/s	15.404 s	28.803 s	0.3	49	0.7
TA	Y26A	33.9232	-103.8246	1371 m	35 km	7.3 km	1.9	0.13	6.129 km/s	3.226 km/s	11.421 s	21.699 s	0.31	47	0.7
TA	Y28A	33.9086	-102.2479	1068 m	43 km	1.8 km	1.83	0.01	6.129 km/s	3.349 km/s	14.032 s	25.679 s	0.29	27	0.49
TA	Y29A	33.8602	-101.6712	991 m	47 km	7.1 km	1.72	0.1	6.426 km/s	3.736 km/s	14.628 s	25.161 s	0.24	27	0.81
TA	Z25A	33.2797	-104.7171	1233 m	55 km	4.8 km	1.84	0.06	6.232 km/s	3.387 km/s	17.651 s	32.477 s	0.29	56	0.71
TA	Z26A	33.2716	-103.9798	1163 m	41 km	5.1 km	1.85	0.11	6.129 km/s	3.313 km/s	13.379 s	24.751 s	0.29	45	0.7
TA	Z27A	33.315	-103.2145	1197 m	49 km	6.7 km	1.75	0.18	6.129 km/s	3.502 km/s	15.990 s	27.984 s	0.26	41	0.78
TA	Z28A	33.2884	-102.3866	1045 m	49 km	3.1 km	1.72	0.05	6.129 km/s	3.563 km/s	15.990 s	27.505 s	0.24	19	0.71
TA	Z29A	33.2595	-101.7062	938 m	29 km	5.9 km	1.92	0.03	6.426 km/s	3.347 km/s	9.026 s	17.329 s	0.31	32	0.62

Table A-1c. Station location and receiver function information for the SIMPLE region. The stations selected for detailed analysis in this study have bold names.

Station	Lat	Long	Elev	Est. Thick	Std Dev	Est. Vp/Vs	Std Dev	Assumed Vp	Vs	TWTT Vp	TWTT Vs	Poissons Ratio	Num EQ	Complexity
A30A	48.94	-98.3	484 m	25 km	2.8 km	1.68	0.09	6.53 km/s	3.887 km/s	7.657 s	12.863 s	0.23	40	0.8
A31A	48.932	-97.189	244 m	44 km	4.4 km	1.78	0.1	6.498 km/s	3.651 km/s	13.543 s	24.103 s	0.27	17	0.7
A32A	48.9172	-96.494	322 m	48 km	3.4 km	1.67	0.1	6.498 km/s	3.891 km/s	14.774 s	24.672 s	0.22	27	0.7
A33A	48.9371	-95.39	329 m	40 km	2.9 km	1.77	0.08	6.419 km/s	3.627 km/s	12.463 s	22.057 s	0.27	53	0.6
B30A	48.4505	-98.329	480 m	30 km	5.8 km	1.65	0.07	6.53 km/s	3.958 km/s	9.188 s	15.159 s	0.21	46	0.8
B31A	48.4236	-97.65	279 m	44 km	0.6 km	1.77	0.01	6.498 km/s	3.671 km/s	13.543 s	23.972 s	0.27	42	0.5
B32A	48.3951	-96.536	335 m	50 km	5.6 km	1.71	0.12	6.498 km/s	3.8 km/s	15.389 s	26.316 s	0.24	37	0.7
B33A	48.2722	-95.588	362 m	46 km	5.7 km	1.73	0.12	6.419 km/s	3.71 km/s	14.332 s	24.798 s	0.25	33	0.7
B34A	48.486	-94.65	354 m	34 km	5.7 km	2.05	0.12	6.419 km/s	3.131 km/s	10.594 s	21.718 s	0.34	38	0.7
B35A	48.3603	-93.726	358 m	48 km	4.4 km	1.66	0.07	6.419 km/s	3.867 km/s	14.956 s	24.825 s	0.22	32	0.8
BGNE	41.4083	-98.15	573 m	52 km	7.5 km	1.73	0.13	6.53 km/s	3.775 km/s	15.926 s	27.550 s	0.25	174	0.9

Approved for public release; distribution is unlimited.

Table A-1c. Station location and receiver function information for the SIMPLE region. The stations selected for detailed analysis in this study have bold names (continued).

BRSD	44.443	-98.956	519 m	30 km	4.0 km	1.61	0.03	6.53 km/s	4.056 km/s	9.188 s	14.793 s	0.19	45	0.8
C30A	47.7026	-98.478	480 m	32 km	0.9 km	1.7	0.02	6.53 km/s	3.841 km/s	9.801 s	16.662 s	0.24	39	0.5
C31A	47.7927	-97.734	384 m	25 km	7.2 km	1.6	0.08	6.498 km/s	4.061 km/s	7.695 s	12.312 s	0.18	51	1
C32A	47.8255	-96.528	286 m	46 km	2.5 km	1.65	0.06	6.498 km/s	3.938 km/s	14.158 s	23.362 s	0.21	15	0.7
C33A	47.7586	-95.773	388 m	40 km	0.3 km	1.73	0.01	6.419 km/s	3.71 km/s	12.463 s	21.563 s	0.25	35	0.5
C34A	47.6501	-94.911	441 m	37 km	3.5 km	1.88	0.13	6.419 km/s	3.414 km/s	11.528 s	21.675 s	0.3	11	0.7
C35A	47.7007	-93.976	426 m	41 km	1.7 km	1.7	0.04	6.571 km/s	3.865 km/s	12.479 s	21.216 s	0.24	40	0.6
C36A	47.758	-92.838	410 m	46 km	5.3 km	1.72	0.13	6.571 km/s	3.82 km/s	14.001 s	24.084 s	0.24	42	0.7
C37A	47.7283	-92.185	447 m	43 km	0.6 km	1.72	0.01	6.571 km/s	3.82 km/s	13.088 s	22.513 s	0.24	40	0.5
C38A	47.7171	-91.273	498 m	31 km	3.2 km	1.85	0.11	6.467 km/s	3.496 km/s	9.587 s	17.735 s	0.29	47	0.7
C39A	47.8171	-90.129	341 m	29 km	2.9 km	1.8	0.09	6.467 km/s	3.593 km/s	8.969 s	16.142 s	0.28	27	0.7
D30A	47.1082	-98.758	465 m	38 km	1.1 km	1.7	0.03	6.53 km/s	3.841 km/s	11.639 s	19.787 s	0.24	29	0.7
D31A	47.0481	-97.723	359 m	36 km	0.1 km	1.77	0.01	6.498 km/s	3.671 km/s	11.080 s	19.613 s	0.27	56	0.4
D32A	47.1354	-97.016	280 m	37 km	0.6 km	1.77	0.02	6.498 km/s	3.671 km/s	11.388 s	20.158 s	0.27	21	0.3
D33A	47.1404	-95.845	466 m	32 km	5.8 km	2.01	0.15	6.419 km/s	3.194 km/s	9.970 s	20.038 s	0.34	31	0.7
D34A	47.0851	-95.195	476 m	41 km	1.0 km	1.6	0.02	6.419 km/s	4.012 km/s	12.775 s	20.439 s	0.18	45	0.7
D35A	47.081	-94.053	427 m	42 km	1.0 km	1.76	0.02	6.419 km/s	3.647 km/s	13.086 s	23.033 s	0.26	36	0.5
D36A	47.1765	-93.165	434 m	46 km	3.8 km	1.75	0.08	6.571 km/s	3.755 km/s	14.001 s	24.501 s	0.26	37	0.7
D37A	47.1581	-92.426	413 m	35 km	6.1 km	2.01	0.14	6.571 km/s	3.269 km/s	10.653 s	21.413 s	0.34	41	0.7
E30A	46.5021	-98.91	544 m	38 km	0.3 km	1.8	0.01	6.53 km/s	3.628 km/s	11.639 s	20.948 s	0.28	29	0.7
E31A	46.5583	-97.888	427 m	34 km	3.3 km	1.83	0.1	6.498 km/s	3.551 km/s	10.465 s	19.150 s	0.29	63	0.7
E32A	46.5927	-97.07	297 m	36 km	0.2 km	1.73	0.01	6.498 km/s	3.756 km/s	11.080 s	19.169 s	0.25	28	0.3
E33A	46.5035	-96.005	428 m	36 km	0.6 km	1.79	0.02	6.498 km/s	3.63 km/s	11.080 s	19.835 s	0.27	39	0.5
E34A	46.5136	-95.169	430 m	29 km	4.9 km	2.1	0.14	6.419 km/s	3.057 km/s	9.036 s	18.973 s	0.35	37	0.9
E35A	46.5572	-94.404	409 m	33 km	7.4 km	2.1	0.15	6.419 km/s	3.057 km/s	10.282 s	21.590 s	0.35	41	0.7
E36A	46.5177	-93.256	393 m	44 km	3.8 km	1.74	0.07	6.571 km/s	3.776 km/s	13.392 s	23.305 s	0.25	43	0.7
E37A	46.5658	-92.4	304 m	42 km	6.6 km	1.61	0.11	6.571 km/s	4.081 km/s	12.783 s	20.583 s	0.19	16	0.8
E38A	46.6058	-91.554	341 m	32 km	4.1 km	1.99	0.21	6.467 km/s	3.25 km/s	9.896 s	19.692 s	0.33	34	0.8
E39A	46.3777	-90.556	426 m	34 km	5.0 km	1.96	0.08	6.467 km/s	3.299 km/s	10.515 s	20.612 s	0.32	38	0.8
F31A	45.8598	-98.253	412 m	30 km	0.2 km	2.01	0.01	6.53 km/s	3.249 km/s	9.188 s	18.467 s	0.34	47	0.5
F32A	45.8705	-97.126	371 m	25 km	6.8 km	1.61	0.07	6.552 km/s	4.07 km/s	7.631 s	12.285 s	0.19	42	1
F33A	45.8398	-96.293	313 m	39 km	1.1 km	1.71	0.02	6.552 km/s	3.832 km/s	11.905 s	20.355 s	0.24	38	0.6
F34A	45.7954	-95.258	419 m	43 km	0.6 km	1.77	0.01	6.571 km/s	3.712 km/s	13.088 s	23.168 s	0.27	35	0.5
F35A	45.858	-94.573	376 m	47 km	0.2 km	1.76	0.01	6.571 km/s	3.734 km/s	14.305 s	25.174 s	0.26	38	0.4
F36A	45.8618	-93.524	345 m	46 km	0.2 km	1.7	0	6.571 km/s	3.865 km/s	14.001 s	23.803 s	0.24	37	0.5
F37A	45.7243	-92.626	296 m	40 km	5.8 km	1.89	0.08	6.571 km/s	3.477 km/s	12.175 s	23.008 s	0.31	36	0.8

Approved for public release; distribution is unlimited.

Table A-1c. Station location and receiver function information for the SIMPLE region. The stations selected for detailed analysis in this study have bold names (continued).

F39A	45.9153	-90.919	440 m	40 km	1.5 km	1.82	0.03	6.571 km/s	3.61 km/s	12.175 s	22.161 s	0.28	34	0.6
F40A	45.919	-90.122	486 m	43 km	0.3 km	1.69	0.01	6.571 km/s	3.888 km/s	13.088 s	22.119 s	0.23	38	0.4
G31A	45.2254	-98.208	393 m	30 km	6.8 km	1.6	0.08	6.53 km/s	4.081 km/s	9.188 s	14.702 s	0.18	57	0.9
G32A	45.2555	-97.499	566 m	25 km	4.5 km	2.04	0.12	6.552 km/s	3.212 km/s	7.631 s	15.567 s	0.34	40	0.7
G33A	45.1946	-96.438	338 m	42 km	0.3 km	1.73	0.01	6.552 km/s	3.787 km/s	12.821 s	22.181 s	0.25	33	0.5
G34A	45.2419	-95.638	316 m	44 km	3.4 km	1.75	0.07	6.571 km/s	3.755 km/s	13.392 s	23.435 s	0.26	32	0.6
G35A	45.2199	-94.486	361 m	44 km	0.3 km	1.79	0.01	6.571 km/s	3.671 km/s	13.392 s	23.972 s	0.27	39	0.4
G36A	45.2344	-93.751	293 m	44 km	5.9 km	1.84	0.13	6.571 km/s	3.571 km/s	13.392 s	24.643 s	0.29	26	0.7
G38A	45.1693	-91.855	370 m	25 km	9.7 km	1.62	0.05	6.571 km/s	4.056 km/s	7.609 s	12.327 s	0.19	35	1
G39A	45.2867	-91.17	350 m	46 km	1.2 km	1.71	0.03	6.571 km/s	3.843 km/s	14.001 s	23.940 s	0.24	52	0.6
G40A	45.2684	-90.201	472 m	33 km	8.4 km	1.97	0.1	6.571 km/s	3.336 km/s	10.044 s	19.784 s	0.33	57	0.8
H31A	44.4795	-98.477	415 m	25 km	7.4 km	2.1	0.16	6.53 km/s	3.11 km/s	7.657 s	16.077 s	0.35	50	0.8
H32A	44.5041	-97.436	573 m	55 km	11 km	1.8	0.11	6.552 km/s	3.64 km/s	16.789 s	30.220 s	0.28	48	0.8
H33A	44.6812	-96.743	584 m	48 km	8.2 km	1.8	0.03	6.552 km/s	3.64 km/s	14.652 s	26.374 s	0.28	46	0.8
H34A	44.6673	-95.777	329 m	35 km	0.7 km	2.09	0.03	6.571 km/s	3.144 km/s	10.653 s	22.265 s	0.35	36	0.6
H35A	44.6985	-94.831	345 m	46 km	1.8 km	1.77	0.05	6.571 km/s	3.712 km/s	14.001 s	24.784 s	0.27	44	0.6
H36A	44.5775	-93.928	311 m	32 km	10 km	1.99	0.14	6.571 km/s	3.302 km/s	9.740 s	19.382 s	0.33	27	0.8
H37A	44.5812	-92.918	321 m	25 km	13 km	1.95	0.1	6.571 km/s	3.37 km/s	7.609 s	14.837 s	0.32	26	0.9
H38A	44.6753	-92.282	333 m	48 km	0.9 km	1.71	0.01	6.571 km/s	3.843 km/s	14.610 s	24.980 s	0.24	35	0.5
H39A	44.6797	-91.283	345 m	52 km	0.4 km	1.76	0.01	6.571 km/s	3.734 km/s	15.827 s	27.852 s	0.26	28	0.4
H40A	44.622	-90.391	372 m	46 km	1.7 km	1.78	0.03	6.571 km/s	3.692 km/s	14.001 s	24.919 s	0.27	40	0.6
I31A	44.0297	-98.535	469 m	27 km	6.3 km	2.1	0.15	6.53 km/s	3.11 km/s	8.270 s	17.363 s	0.35	37	0.8
I32A	44.0271	-97.464	493 m	27 km	4.1 km	1.6	0.05	6.552 km/s	4.095 km/s	8.242 s	13.187 s	0.18	34	0.9
I33A	44.0475	-96.799	509 m	40 km	4.6 km	1.66	0.11	6.552 km/s	3.947 km/s	12.210 s	20.269 s	0.22	58	0.8
I34A	44.0392	-95.86	509 m	38 km	8.9 km	1.97	0.16	6.571 km/s	3.336 km/s	11.566 s	22.782 s	0.33	26	0.7
I35A	43.8565	-94.983	428 m	29 km	7.4 km	2.07	0.2	6.53 km/s	3.155 km/s	8.882 s	18.384 s	0.35	35	0.8
I36A	44.0191	-94.014	307 m	41 km	0.2 km	1.8	0.01	6.571 km/s	3.651 km/s	12.479 s	22.460 s	0.28	32	0.5
I37A	44.0148	-93.4	371 m	50 km	8.1 km	1.91	0.11	6.571 km/s	3.44 km/s	15.218 s	29.070 s	0.31	31	0.6
I38A	44.0405	-92.331	390 m	38 km	1.9 km	1.83	0.04	6.571 km/s	3.591 km/s	11.566 s	21.164 s	0.29	39	0.6
I39A	43.8543	-91.523	393 m	42 km	1.0 km	1.71	0.01	6.53 km/s	3.819 km/s	12.864 s	21.995 s	0.24	33	0.4
I40A	43.8916	-90.618	419 m	46 km	0.2 km	1.76	0.01	6.53 km/s	3.71 km/s	14.089 s	24.798 s	0.26	37	0.4
J31A	43.2915	-98.74	491 m	25 km	4.3 km	1.6	0.08	6.53 km/s	4.081 km/s	7.657 s	12.252 s	0.18	43	1
J32A	43.3719	-97.848	399 m	26 km	12 km	1.71	0.1	6.498 km/s	3.8 km/s	8.002 s	13.684 s	0.24	35	0.9
J33A	43.3185	-96.967	400 m	49 km	2.6 km	1.62	0.01	6.498 km/s	4.011 km/s	15.082 s	24.433 s	0.19	34	0.6
J34A	43.2844	-95.958	432 m	34 km	4.9 km	2.09	0.18	6.53 km/s	3.124 km/s	10.413 s	21.767 s	0.35	14	0.8
J35A	43.3655	-95.208	457 m	36 km	4.8 km	1.8	0.12	6.53 km/s	3.628 km/s	11.026 s	19.846 s	0.28	35	0.8

Approved for public release; distribution is unlimited.

Table A-1c. Station location and receiver function information for the SIMPLE region. The stations selected for detailed analysis in this study have bold names (continued).

J36A	43.3292	-94.34	370 m	37 km	3.3 km	1.98	0.07	6.53 km/s	3.298 km/s	11.332 s	22.438 s	0.33	42	0.6
J37A	43.3103	-93.553	385 m	39 km	6.1 km	1.99	0.11	6.53 km/s	3.281 km/s	11.945 s	23.773 s	0.33	30	0.7
J38A	43.319	-92.476	371 m	30 km	2.3 km	1.93	0.05	6.53 km/s	3.383 km/s	9.188 s	17.736 s	0.32	32	0.7
J39A	43.3354	-91.706	350 m	38 km	0.2 km	1.77	0.01	6.53 km/s	3.689 km/s	11.639 s	20.602 s	0.27	32	0.3
J40A	43.3965	-90.741	353 m	44 km	0.4 km	1.75	0.02	6.53 km/s	3.731 km/s	13.476 s	23.586 s	0.26	36	0.5
K31A	42.6229	-98.755	580 m	26 km	1.4 km	1.73	0.03	6.53 km/s	3.775 km/s	7.963 s	13.775 s	0.25	49	0.6
K32A	42.6597	-97.972	512 m	36 km	2.8 km	1.7	0.03	6.498 km/s	3.822 km/s	11.080 s	18.838 s	0.24	47	0.6
K33A	42.6052	-97.001	507 m	26 km	3.2 km	1.9	0.09	6.498 km/s	3.42 km/s	8.002 s	15.205 s	0.31	42	0.6
K34A	42.6865	-96.096	436 m	25 km	12 km	1.79	0.12	6.498 km/s	3.63 km/s	7.695 s	13.774 s	0.27	32	0.9
K35A	42.7218	-95.233	439 m	44 km	2.4 km	1.85	0.07	6.53 km/s	3.53 km/s	13.476 s	24.929 s	0.29	35	0.6
K36A	42.6381	-94.451	364 m	45 km	2.2 km	1.75	0.05	6.53 km/s	3.731 km/s	13.783 s	24.122 s	0.26	22	0.6
K37A	42.7669	-93.639	365 m	50 km	7.3 km	1.7	0.13	6.53 km/s	3.841 km/s	15.314 s	26.035 s	0.24	46	0.8
K38A	42.6472	-92.771	306 m	34 km	2.1 km	1.95	0.03	6.53 km/s	3.349 km/s	10.413 s	20.305 s	0.32	25	0.7
K39A	42.705	-91.888	332 m	36 km	2.7 km	1.92	0.16	6.53 km/s	3.401 km/s	11.026 s	21.170 s	0.31	42	0.6
K40A	42.6999	-91.138	274 m	43 km	0.3 km	1.79	0.01	6.53 km/s	3.648 km/s	13.170 s	23.575 s	0.27	39	0.3
K41A	42.6071	-90.305	298 m	44 km	0.2 km	1.77	0.01	6.53 km/s	3.689 km/s	13.476 s	23.855 s	0.27	44	0.4
L31A	42.176	-98.839	670 m	25 km	13 km	1.93	0.1	6.53 km/s	3.383 km/s	7.657 s	14.780 s	0.32	48	0.9
L32A	42.0045	-98.008	586 m	34 km	6.6 km	1.62	0.08	6.53 km/s	4.031 km/s	10.413 s	16.869 s	0.19	27	0.8
L33A	42.1659	-97.272	556 m	38 km	6.5 km	1.79	0.16	6.498 km/s	3.63 km/s	11.696 s	20.937 s	0.27	20	0.7
L34A	41.9666	-96.376	424 m	40 km	2.0 km	1.82	0.05	6.498 km/s	3.57 km/s	12.311 s	22.409 s	0.28	27	0.6
L34B	41.9666	-96.376	414 m	39 km	1.7 km	1.84	0.03	6.498 km/s	3.532 km/s	12.004 s	22.084 s	0.29	26	0.6
L35A	42.1123	-95.545	410 m	42 km	4.1 km	1.86	0.06	6.53 km/s	3.511 km/s	12.864 s	23.925 s	0.3	28	0.6
L36A	42.1009	-94.668	353 m	50 km	0.3 km	1.8	0.01	6.53 km/s	3.628 km/s	15.314 s	27.563 s	0.28	46	0.5
L37A	42.1246	-93.755	312 m	46 km	3.7 km	1.75	0.07	6.53 km/s	3.731 km/s	14.089 s	24.658 s	0.26	33	0.7
L38A	42.141	-92.96	300 m	45 km	1.3 km	1.84	0.03	6.53 km/s	3.549 km/s	13.783 s	25.359 s	0.29	26	0.5
L39A	42.1234	-92.001	261 m	44 km	0.4 km	1.77	0.02	6.53 km/s	3.689 km/s	13.476 s	23.855 s	0.27	38	0.5
L40A	42.0628	-91.222	242 m	40 km	0.2 km	1.75	0.01	6.53 km/s	3.731 km/s	12.251 s	21.442 s	0.26	58	0.4
L41A	42.0751	-90.498	238 m	40 km	0.3 km	1.76	0.01	6.53 km/s	3.71 km/s	12.251 s	21.563 s	0.26	36	0.5
M31A	41.344	-98.977	699 m	28 km	4.6 km	2	0.1	6.53 km/s	3.265 km/s	8.576 s	17.152 s	0.33	29	0.6
M33A	41.5726	-97.195	503 m	40 km	3.5 km	1.93	0.08	6.498 km/s	3.367 km/s	12.311 s	23.760 s	0.32	34	0.6
M34A	41.5025	-96.583	415 m	40 km	0.8 km	1.88	0.04	6.498 km/s	3.456 km/s	12.311 s	23.148 s	0.3	27	0.5
M35A	41.4665	-95.695	363 m	40 km	2.4 km	1.6	0.17	6.498 km/s	4.061 km/s	12.311 s	19.700 s	0.18	32	0.9
M36A	41.4537	-94.802	430 m	32 km	9.1 km	1.61	0.14	6.498 km/s	4.036 km/s	9.849 s	15.857 s	0.19	52	0.9
M37A	41.4028	-94.058	325 m	48 km	0.2 km	1.75	0.01	6.498 km/s	3.713 km/s	14.774 s	25.855 s	0.26	35	0.4
M38A	41.4175	-93.197	258 m	45 km	2.1 km	1.72	0.03	6.498 km/s	3.778 km/s	13.850 s	23.822 s	0.24	31	0.6
M39A	41.4786	-92.173	264 m	43 km	0.3 km	1.75	0.01	6.498 km/s	3.713 km/s	13.235 s	23.162 s	0.26	32	0.3

Approved for public release; distribution is unlimited.

Table A-1c. Station location and receiver function information for the SIMPLE region. The stations selected for detailed analysis in this study have bold names (continued).

M40A	41.406	-91.512	223 m	38 km	0.4 km	1.8	0.02	6.498 km/s	3.61 km/s	11.696 s	21.053 s	0.28	24	0.4
M41A	41.375	-90.542	226 m	40 km	0.5 km	1.82	0.02	6.498 km/s	3.57 km/s	12.311 s	22.409 s	0.28	41	0.5
N31A	40.8235	-98.954	687 m	42 km	7.6 km	1.6	0.15	6.53 km/s	4.081 km/s	12.864 s	20.583 s	0.18	36	0.9
N32A	40.7639	-98.296	587 m	39 km	0.8 km	1.95	0.02	6.53 km/s	3.349 km/s	11.945 s	23.291 s	0.32	30	0.5
N33A	40.7384	-97.451	475 m	44 km	4.5 km	1.81	0.07	6.498 km/s	3.59 km/s	13.543 s	24.513 s	0.28	40	0.6
N35A	40.8612	-95.643	353 m	40 km	6.2 km	1.97	0.11	6.498 km/s	3.298 km/s	12.311 s	24.257 s	0.33	35	0.7
N36A	40.8156	-94.96	349 m	44 km	1.0 km	1.79	0.02	6.498 km/s	3.63 km/s	13.543 s	24.242 s	0.27	48	0.5
N37A	40.7582	-94.21	351 m	41 km	2.4 km	1.91	0.05	6.498 km/s	3.402 km/s	12.619 s	24.103 s	0.31	44	0.5
N38A	40.7931	-93.235	317 m	57 km	9.1 km	1.64	0.16	6.498 km/s	3.962 km/s	17.544 s	28.773 s	0.2	35	0.9
N39A	40.8776	-92.502	260 m	44 km	5.4 km	1.77	0.13	6.498 km/s	3.671 km/s	13.543 s	23.972 s	0.27	32	0.7
N40A	40.8841	-91.584	208 m	38 km	2.3 km	1.89	0.05	6.498 km/s	3.438 km/s	11.696 s	22.106 s	0.31	42	0.6
N41A	40.7077	-90.855	226 m	35 km	3.5 km	1.93	0.08	6.498 km/s	3.367 km/s	10.773 s	20.790 s	0.32	53	0.6
N42A	40.829	-90.035	205 m	47 km	6.1 km	1.73	0.11	6.498 km/s	3.756 km/s	14.466 s	25.027 s	0.25	19	0.7
O32A	40.261	-98.276	579 m	31 km	2.4 km	2.09	0.1	6.53 km/s	3.124 km/s	9.495 s	19.846 s	0.35	27	0.7
O33A	40.0755	-97.585	480 m	39 km	0.8 km	1.78	0.02	6.498 km/s	3.651 km/s	12.004 s	21.364 s	0.27	40	0.6
O34A	40.1831	-96.694	409 m	46 km	4.5 km	1.79	0.06	6.498 km/s	3.63 km/s	14.158 s	25.344 s	0.27	36	0.5
O35A	40.2665	-95.91	342 m	40 km	7.0 km	1.79	0.12	6.498 km/s	3.63 km/s	12.311 s	22.039 s	0.27	25	0.8
O36A	40.1315	-94.965	306 m	41 km	0.2 km	1.77	0.01	6.498 km/s	3.671 km/s	12.619 s	22.337 s	0.27	41	0.3
O37A	40.1664	-94.146	284 m	44 km	4.9 km	1.78	0.11	6.498 km/s	3.651 km/s	13.543 s	24.103 s	0.27	36	0.6
O38A	40.1215	-93.473	266 m	44 km	3.8 km	1.73	0.09	6.498 km/s	3.756 km/s	13.543 s	23.429 s	0.25	34	0.7
O39A	40.2544	-92.544	282 m	40 km	5.7 km	2.04	0.12	6.498 km/s	3.185 km/s	12.311 s	25.118 s	0.34	34	0.8
O40A	40.1212	-91.874	206 m	43 km	1.6 km	1.94	0.05	6.498 km/s	3.349 km/s	13.235 s	25.679 s	0.32	37	0.6
O41A	40.1156	-90.882	203 m	41 km	0.4 km	1.8	0.02	6.498 km/s	3.61 km/s	12.619 s	22.715 s	0.28	35	0.4
O42A	40.1956	-90.081	155 m	43 km	0.3 km	1.8	0.01	6.498 km/s	3.61 km/s	13.235 s	23.823 s	0.28	31	0.4
P32A	39.6223	-98.601	524 m	36 km	2.9 km	1.89	0.05	6.483 km/s	3.43 km/s	11.106 s	20.991 s	0.31	39	0.5
P33A	39.4363	-97.695	488 m	37 km	2.2 km	1.94	0.05	6.483 km/s	3.342 km/s	11.414 s	22.142 s	0.32	27	0.5
P34A	39.5471	-96.827	429 m	31 km	5.8 km	1.89	0.13	6.483 km/s	3.43 km/s	9.563 s	18.076 s	0.31	38	0.6
P35A	39.5286	-96.019	418 m	44 km	1.3 km	1.76	0.03	6.483 km/s	3.684 km/s	13.574 s	23.887 s	0.26	36	0.5
P36A	39.6204	-95.206	313 m	41 km	1.2 km	1.8	0.03	6.498 km/s	3.61 km/s	12.619 s	22.715 s	0.28	39	0.5
P37A	39.5882	-94.349	300 m	43 km	0.2 km	1.75	0.02	6.498 km/s	3.713 km/s	13.235 s	23.162 s	0.26	39	0.5
P38A	39.6248	-93.532	248 m	44 km	0.5 km	1.77	0.03	6.498 km/s	3.671 km/s	13.543 s	23.972 s	0.27	45	0.5
P39A	39.4877	-92.755	232 m	46 km	2.8 km	1.66	0.06	6.498 km/s	3.914 km/s	14.158 s	23.505 s	0.22	7	0.6
P39B	39.4876	-92.754	226 m	45 km	0.2 km	1.75	0.01	6.498 km/s	3.713 km/s	13.850 s	24.239 s	0.26	27	0.4
P40A	39.5299	-92.048	225 m	47 km	2.0 km	1.73	0.04	6.498 km/s	3.756 km/s	14.466 s	25.027 s	0.25	37	0.6
P41A	39.675	-91.062	215 m	51 km	5.3 km	1.79	0.09	6.498 km/s	3.63 km/s	15.697 s	28.099 s	0.27	35	0.7
P42A	39.5853	-90.344	197 m	25 km	13 km	1.64	0.14	6.498 km/s	3.962 km/s	7.695 s	12.620 s	0.2	33	1

Approved for public release; distribution is unlimited.

Table A-1c. Station location and receiver function information for the SIMPLE region. The stations selected for detailed analysis in this study have bold names (continued).

Q32A	38.9908	-98.56	526 m	38 km	1.9 km	1.86	0.08	6.483 km/s	3.485 km/s	11.723 s	21.808 s	0.3	32	0.6
Q33A	38.9982	-97.833	422 m	41 km	5.6 km	1.81	0.08	6.483 km/s	3.582 km/s	12.648 s	22.892 s	0.28	26	0.7
Q34A	38.9214	-96.941	378 m	48 km	2.8 km	1.84	0.06	6.483 km/s	3.523 km/s	14.808 s	27.250 s	0.29	36	0.6
Q35A	38.8586	-96.037	402 m	40 km	0.2 km	1.79	0.01	6.483 km/s	3.622 km/s	12.340 s	22.087 s	0.27	41	0.4
Q36A	38.9612	-95.461	306 m	41 km	6.5 km	1.76	0.13	6.498 km/s	3.692 km/s	12.619 s	22.210 s	0.26	38	0.7
Q37A	38.8763	-94.452	297 m	42 km	1.3 km	1.84	0.03	6.498 km/s	3.532 km/s	12.927 s	23.783 s	0.29	38	0.5
Q38A	38.9609	-93.618	228 m	37 km	11 km	2.05	0.19	6.498 km/s	3.17 km/s	11.388 s	23.344 s	0.34	36	0.8
Q39A	39.0455	-92.976	225 m	44 km	0.2 km	1.77	0.01	6.498 km/s	3.671 km/s	13.543 s	23.972 s	0.27	37	0.2
Q40A	38.9946	-92.075	275 m	44 km	3.9 km	1.77	0.07	6.498 km/s	3.671 km/s	13.543 s	23.972 s	0.27	25	0.6
Q41A	38.9539	-91.232	191 m	39 km	5.5 km	1.98	0.1	6.498 km/s	3.282 km/s	12.004 s	23.766 s	0.33	29	0.7
Q42A	38.912	-90.533	175 m	25 km	5.9 km	1.6	0.06	6.498 km/s	4.061 km/s	7.695 s	12.312 s	0.18	36	1
R32A	38.4225	-98.711	573 m	42 km	0.2 km	1.78	0.01	6.483 km/s	3.642 km/s	12.957 s	23.064 s	0.27	30	0.3
R33A	38.3081	-97.984	497 m	39 km	0.9 km	1.79	0.02	6.483 km/s	3.622 km/s	12.031 s	21.535 s	0.27	24	0.5
R34A	38.3008	-97.247	437 m	43 km	2.2 km	1.82	0.05	6.483 km/s	3.562 km/s	13.265 s	24.144 s	0.28	40	0.6
R35A	38.3231	-96.199	365 m	43 km	6.4 km	1.8	0.15	6.483 km/s	3.602 km/s	13.265 s	23.876 s	0.28	43	0.6
R36A	38.3237	-95.504	354 m	42 km	2.1 km	1.76	0.04	6.498 km/s	3.692 km/s	12.927 s	22.752 s	0.26	48	0.6
R37A	38.3133	-94.829	298 m	42 km	2.8 km	1.69	0.04	6.498 km/s	3.845 km/s	12.927 s	21.847 s	0.23	25	0.6
R38A	38.1868	-93.906	237 m	42 km	2.7 km	1.77	0.06	6.498 km/s	3.671 km/s	12.927 s	22.882 s	0.27	35	0.6
R39A	38.3138	-93.038	290 m	48 km	1.4 km	1.75	0.03	6.498 km/s	3.713 km/s	14.774 s	25.855 s	0.26	32	0.5
R40A	38.2909	-92.268	213 m	43 km	3.1 km	1.77	0.07	6.498 km/s	3.671 km/s	13.235 s	23.427 s	0.27	36	0.6
R41A	38.2976	-91.38	257 m	40 km	3.8 km	1.85	0.07	6.498 km/s	3.512 km/s	12.311 s	22.779 s	0.29	31	0.6
R42A	38.2804	-90.794	218 m	38 km	1.6 km	2.1	0.04	6.498 km/s	3.094 km/s	11.696 s	24.564 s	0.35	34	0.6
S32A	37.7001	-98.936	558 m	32 km	12 km	2.09	0.22	6.426 km/s	3.075 km/s	9.960 s	20.813 s	0.35	31	0.8
S33A	37.5936	-98.002	471 m	46 km	2.5 km	1.76	0.05	6.426 km/s	3.651 km/s	14.317 s	25.199 s	0.26	32	0.5
S34A	37.7009	-97.111	373 m	45 km	2.1 km	1.75	0.01	6.483 km/s	3.705 km/s	13.882 s	24.291 s	0.26	26	0.5
S35A	37.6821	-96.319	334 m	51 km	5.7 km	1.64	0.08	6.483 km/s	3.953 km/s	15.733 s	25.803 s	0.2	47	0.8
S36A	37.724	-95.592	299 m	42 km	0.9 km	1.8	0.02	6.53 km/s	3.628 km/s	12.864 s	23.153 s	0.28	33	0.5
S37A	37.7597	-94.828	260 m	44 km	0.2 km	1.76	0.01	6.53 km/s	3.71 km/s	13.476 s	23.720 s	0.26	34	0.4
S38A	37.6304	-93.908	294 m	44 km	0.3 km	1.76	0.01	6.53 km/s	3.71 km/s	13.476 s	23.720 s	0.26	29	0.4
S39A	37.691	-93.323	331 m	47 km	3.5 km	1.82	0.08	6.53 km/s	3.588 km/s	14.395 s	26.198 s	0.28	36	0.6
S40A	37.5988	-92.501	336 m	52 km	5.3 km	1.72	0.1	6.53 km/s	3.797 km/s	15.926 s	27.390 s	0.24	31	0.8
S41A	37.5877	-91.746	376 m	48 km	2.1 km	1.72	0.05	6.53 km/s	3.797 km/s	14.701 s	25.283 s	0.24	38	0.6
S42A	37.77	-90.794	315 m	45 km	1.2 km	1.79	0.03	6.53 km/s	3.648 km/s	13.783 s	24.671 s	0.27	30	0.5
S43A	37.5716	-90.075	263 m	45 km	4.5 km	1.75	0.11	6.53 km/s	3.731 km/s	13.783 s	24.122 s	0.26	35	0.7
SPMN	45.2246	-92.804	311 m	55 km	0.3 km	1.67	0.01	6.571 km/s	3.935 km/s	16.740 s	27.954 s	0.22	129	0.7
SUSD	44.4429	-98.956	520 m	30 km	2.8 km	1.63	0.1	6.53 km/s	4.006 km/s	9.188 s	14.978 s	0.2	165	0.8

Approved for public release; distribution is unlimited.

Table A-2. Models used in synthetic waveform modeling

Depth from the surface (m)	Vp (m/s)	Vs (m/s)	Density (g.m ³)	Model name
10000	5400	3100	2500	M1
20000	6100	3500	2900	
30000	7200	4100	3300	
Half space	8200	4500	3500	
25000	6000	3400	2800	M2
35000	6600	3850	3000	
Half space	8000	4500	3700	
30000	6700	3463	2800	M3
31000	7200	4161	2900	
32000	7700	4450	3400	
Half space	8000	4500	3700	M4
21000	6276	3566	2900	
30000	7300	4000	3110	
Half space	7993	4474	3287	

Table A-3. Custom velocity models used for synthetic waveform modeling at the TEST, SIMPLE and COMPLEX stations

Station	Depth (km)	Vp (m/s)	Vs (m/s)	Density (g/cm ³)	Model
TEST AREA					UNRELFS
ELFS	3000	6608	3684	2751	
	4000	6645	3703	2756	
	5000	6681	3722	2760	
	6000	6717	3742	2765	
	7000	6753	3761	2770	
	11000	6898	3831	2796	
	14000	7005	3875	2820	
	17000	7110	3916	2844	
	20000	7232	3976	2908	
	26000	7535	4194	3157	
	30000	7721	4341	3280	
	34000	7833	4404	3280	
	38000	7928	4446	3281	
ELFS	0-3	6448	3731	2744	RFELFS
	3-5	6556	3781	2760	
	5-6	6591	3798	2766	

Table A-3 Custom velocity models used for synthetic waveform modeling at the TEST, SIMPLE and COMPLEX stations (continued).

	6-7	6662	3831	2776	
	7-12	6803	3872	2808	
	12-15	7005	3919	2862	
	15-18	7186	4044	2978	
	18-24	7534	4325	3209	
	24-26	7579	4370	3230	
	26-30	7651	4404	3280	
	30-34	7728	4431	3230	
	34-36	7746	4451	3231	
	36-42	7812	4464	3243	
	42-60	7885	4415	3235	
	Half Step	7989	4439	3238	
005C	0-3	6608	3684	2751	UNRO05C
	3-4	6645	3703	2756	
	4-5	6681	3722	2760	
	5-6	6717	3742	2765	
	6-7	6753	3761	2770	
	7-11	6898	3831	2796	
	11-14	7005	3875	2820	
	14-17	7110	3916	2844	
	17-20	7232	3976	2908	
	20-26	7535	4194	3157	
	26-30	7721	4341	3280	
	30-34	7833	4404	3280	
	34-38	7928	4446	3281	
	38-42	7973	4452	3282	
	42-44	7969	4449	3282	
	Half Space	7993	4474	3287	
005C	0-41	6597	3685	2900	RFO05C

Table A-3 Custom velocity models used for synthetic waveform modeling at the TEST, SIMPLE and COMPLEX stations (continued).

	Half Space	7993	4474	3287	
O08A	0-32	6276	3804	2900	RFO07A
	Half Space	7993	4474	3287	
O11A	0-10	5400	3100	2000	UNRO11A
	10-20	6100	3500	2870	
	20-30	7200	4100	3010	
	Half Space	8200	4550	3360	
O11A	0-30	6276	3566	2900	RFO11A
	Half Space	7993	4474	3287	
O13A	0-25	6276	3566	2900	RFO13A
	Half Space	7993	4474	3287	
SIMPLE AREA					
N27A	0-10	6228	3000	3000	RFN27A
	10-15	6401	3600	3200	
	15-51	6534	3750	3450	
	Half Space	8131	4700	4200	
N29A	0-10	6228	3000	3000	RFN29A
	10-15	6401	3600	3200	
	15-40	6500	3752	3450	
	Half Space	8131	4700	4200	
COMPLEX AREA					
L37A	0-15	6574	3800	3300	RFL37A
	15-40	6747	3900	3400	
	40-45	7093	4100	3600	
	Half Step	8131	4700	4200	
P37A	0-1	6055	3500	3000	RFP37A

Table A-3 Custom velocity models used for synthetic waveform modeling at the TEST, SIMPLE and COMPLEX stations (continued).

	1-10	6228	3600	3100	
	10-25	6747	3900	3400	
	25-40	7093	4100	3600	
	Half Step	8131	4700	4200	
SPMN	0-1	5882	3400	2900	RFSPMN
	1-5	6055	3500	3000	
	5-10	6228	3600	3100	
	10-15	6401	3700	3200	
	15-20	6488	3750	3250	
	20-25	6574	3800	3300	
	25-30	6747	3900	3400	
	30-35	6834	3950	3650	
	35-40	7093	4100	3600	
	40-45	7439	4300	3800	
	45-50	7785	4500	4000	
	50-55	7958	4600	4100	
	Half Step	8131	4700	4200	

Table A-4. Position of virtual station used for waveform modeling

Station (1-X and 2-Y)	X (m)	Y (M)	Z (M)
11	15000	50000	0
12	30000	50000	0
13	45000	50000	0
14	60000	50000	0
15	75000	50000	0
16	90000	50000	0
21	50000	15000	0
22	50000	30000	0
23	50000	45000	0
24	50000	60000	0
25	50000	75000	0
26	50000	90000	0
BB	50000	15000	0

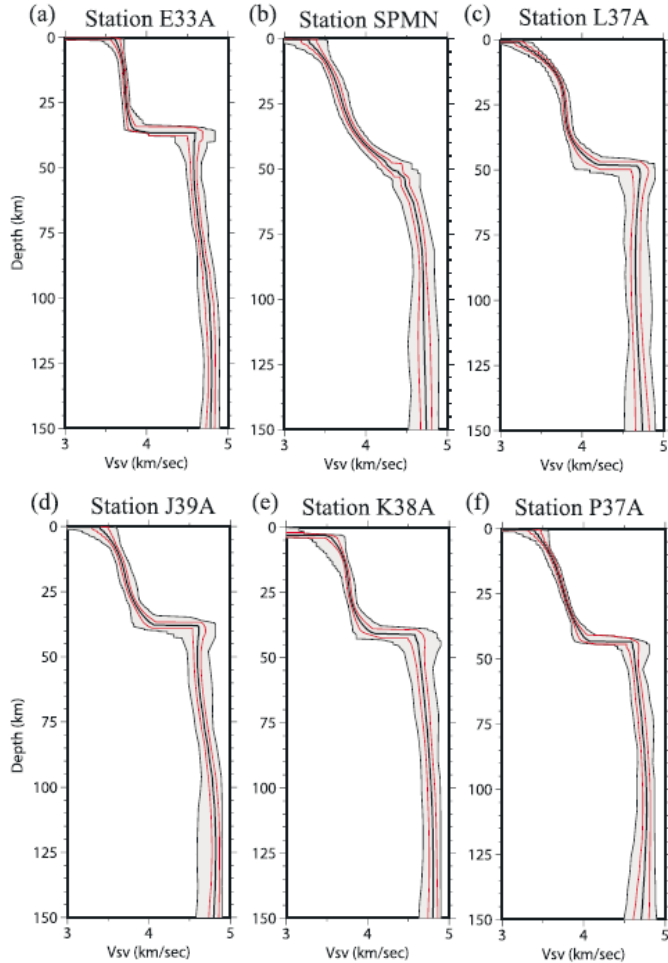


Figure 5. Resulting model ensembles that fit both Rayleigh wave and receiver function data for the six example stations of Figures 3 and 4. (a) The resulting model ensemble for station E33A. The average of the posterior distribution is shown as the black line near the middle of the grey corridor, which defines the full width of the posterior distribution at each depth. The red lines represent the 1σ width of the distribution. (b–f) Same as Figure 5a but for stations SPMN, L37A, J39A, K38A, and P37A, respectively.

Figure A-1. COMPLEX region crustal models estimated by Shel et al., 2013, extracted in Table A-3

LIST OF SYMBOLS, ABBREVIATIONS, AND ACRONYMS

AFRL Air Force Research Laboratory

AFSPC Air Force Space Command

AFWA Air Force Weather Agency

DISTRIBUTION LIST

DTIC/OCP
8725 John J. Kingman Rd, Suite 0944
Ft Belvoir, VA 22060-6218 1 cy

AFRL/RVIL
Kirtland AFB, NM 87117-5776 2 cys

Official Record Copy
AFRL/RVBYE/Robert Raistrick 1 cy